TECHNISCHE UNIVERSITÄT WIEN

Dissertation

Photonics with Loss and Disorder

Ausgeführt zum Zwecke der Erlangung des akademischen Grades eines
Doktors der technischen Wissenschaften

unter der Leitung von
Univ.-Prof. Dipl.-Ing. Dr. techn. Stefan Rotter
Institut für Theoretische Physik, E136

eingereicht an der
Technischen Universität Wien
Fakultät für Physik

von
Dipl.-Ing. Andre Brandstötter
Matr.-Nr. e1025838

Ort, Datum	Unterschrift

Erklärung zur Verfassung der Arbeit

Dipl.-Ing. Andre Brandstötter
Alfred-Stix-Platz 1/20/10, 1100 Wien

Hiermit erkläre ich, dass ich diese Arbeit selbständig verfasst habe, dass ich die verwendeten Quellen und Hilfsmittel vollständig angegeben habe und, dass ich die Stellen der Arbeit – einschließlich Tabellen, Karten und Abbildungen –, die anderen Werken oder dem Internet im Wortlaut oder dem Sinn nach entnommen sind, auf jeden Fall unter Angabe der Quelle als Entlehnung kenntlich gemacht habe.

_____   _____
Ort, Datum   Unterschrift Dipl.-Ing. Andre Brandstötter

Deutsche Kurzfassung

Fortschritte in der Photonik sind typischerweise mit technologischen Neuerungen bei der Herstellung immer komplexerer optischer Geräte verbunden. Bei diesen Bestrebungen, neuartige dielektrische Strukturen zu erzeugen, gibt es zwei Komponenten, die weitgehend ungenutzt geblieben sind: Absorption und Unordnung. Dies ist auf die vorherrschende Ansicht zurückzuführen, dass der Verlust von Licht durch Absorption und die komplexe Streuung, die durch ein ungeordnetes Material hervorgerufen wird, nachteilig und daher von keinem praktischen Interesse sind. Aktuelle theoretische Erkenntnisse und die sich abzeichnenden experimentellen Möglichkeiten, sehr komplizierte Lichtfelder zu modulieren und zu detektieren, verändern derzeit jedoch diese traditionelle Denkweise.

In dieser Arbeit versuchen wir diesen Paradigmenwechsel zu beschleunigen indem wir vielversprechende theoretische Konzepte untersuchen, um die Einflüsse von Absorption und Unordnung zu kontrollieren und sie sogar zum Vorteil zu nutzen. Basierend auf unseren neuesten Arbeiten, in denen wir gezeigt haben, wie eine systemspezifische Verteilung von Absorption und Verstärkung in bestimmten photonischen Strukturen die Streuung der einfallenden Lichtwelle komplett unterdrückt, präsentieren wir in dieser Arbeit einige neue Erkenntnisse aus diesem Forschungsfeld. Wir zeigen, wie eine (ungeordnete) Struktur unidirektional unsichtbar gemacht werden kann, indem auf eine bestimmte Art und Weise Absorption und Verstärkung dem System hinzugefügt wird. Licht, das sich durch solch eine Struktur ausbreitet, kann nicht von Licht unterschieden werden, das sich durch eine homogene Struktur ausbreitet, sodass die Struktur als unsichtbar betrachtet werden kann, obwohl das Medium an sich ungeordnet ist. Darüber hinaus präsentieren wir die erste experimentelle Umsetzung unseres Konzepts in einem ungeordneten akustischen Wellenleiter, in dem wir zeigen, dass wir durch gezielte Absorption und Verstärkung der Schallwelle den Wellenleiter für die Schallwelle transparent machen können. In Abwesenheit von Absorption und Verstärkung würde die Welle reflektiert werden ohne tief in den Wellenleiter eindringen zu können. Durch gezielte Hinzugabe von Absorption und Verstärkung können wir nicht nur die Streuung in der gesamten Struktur unterdrücken, sondern auch die Welle zwingen, einer vorgegebenen Intensitätsverteilung zu folgen. Dadurch kann selbst in ungeordneten Medien an einer bestimmten Stelle ein starker Intensitätsfokus erzeugt werden, der in vielen Bereichen der Physik von großem Interesse ist.

Ein konzeptionell anderer Ansatz zur Bewältigung von Unordnung ohne Absorption und Verstärkung baut auf den jüngsten experimentellen Fortschritten auf, ein komplexes Medium durch Messung seiner Streumatrix zu charakterisieren. Mit diesen neu verfügbaren Möglichkeiten zeigen wir wie sogenannte "teilchenähnliche Streuzustände" – also strahlartige Wellenzustände die sich auf klassischen, geraden Bahnen bewegen – erzeugt werden können. Aufbauend auf dieser Erkenntnis unter-

4

suchen wir die Ausbreitung von Licht in ungeordneten aber räumlich korrelierten Strukturen, die zu einer Aufspaltung der Welle in einzelne Äste führen. Wir entwickeln eine Strategie, die es uns ermöglicht, einzelne Bahnen dieser Verästelung mithilfe von teilchenähnlichen Zuständen zu selektieren. Anders formuliert, können wir die Lichtwelle so beeinflussen, dass sie sich nicht mehr entlang eines verzweigten Geflechts an Pfaden in ganz unterschiedliche Richtungen ausbreitet, sondern auf einer einzelnen vorher ausgewählten Bahn bleibt.

Unter Verwendung eines ähnlichen Konzepts wie bei der Suche nach teilchenähnlichen Wellenzuständen entwickeln wir Strategien zur Manipulation von Teilchen in ungeordneten Materialien. Insbesondere untersuchen wir wie eine Welle von außen auf ein Medium geschickt werden muss, um ein in einer ungeordneten Umgebung verborgenes Teilchen zu manipulieren. Speziell möchten wir auf das Teilchen einen genau definierten Impuls, Druck oder Drehimpuls übertragen beziehungsweise auf das Teilchen fokussieren. Um dies zu erreichen, stellen wir ein neues Konzept vor, das es uns erlaubt die vorher genannten Ziele optimal umzusetzen und vergleichen die daraus resultierenden theoretischen Vorhersagen mit einer experimentellen Implementierung in einem Mikrowellen-Wellenleiter.

Abschließend zeigen wir, dass eine Lichtwelle von einem kleinen, absorptiven Element eingebettet in einem ungeordneten Medium komplett absorbiert werden kann, wenn die Frequenz und die Form der Welle sowie die Absorptionsstärke des absorbierenden Elements richtig eingestellt wird. Wäre die Form der Welle nicht korrekt adjustiert, würde sie von dem Medium zu einem großen Teil reflektiert anstatt absorbiert werden. Dieser Effekt der "kohärenten perfekten Absorption" wird zum ersten Mal experimentell in einem ungeordneten Medium mithilfe von Mikrowellen demonstriert.

Wir hoffen mit dieser Arbeit zur Entstehung weiterer Experimente beitragen zu können, die das enorme Potenzial von Absorption und Unordnung für neue Innovationen in der Photonik aufzeigen.

Abstract

Progress in photonics has traditionally been linked to technological advances in fabricating ever more complex optical devices. In this effort to create arbitrary dielectric structures, two components that have remained largely unexploited are loss and disorder. This is because of the prevailing view that the absorption of light by the loss and the seemingly random scattering induced by a disordered material are disadvantageous and thus of no practical interest. Recent theoretical insights and the emerging experimental possibilities to shape and detect very complicated light fields are currently, however, changing this traditional way of thinking.

In this thesis we try to accelerate this paradigm shift by exploring promising theoretical concepts for controlling the influences of loss and disorder and for turning them to an advantage. Based on our recent work, where we showed how adding a judiciously designed pattern of loss and gain on a given photonic structure leads to light fields that are immune to scattering in a disordered medium, we show here several novel phenomena with interesting features. We demonstrate how to make a (disordered) structure unidirectionally invisible by adding a tailored loss and gain distribution to it. Light propagating through such a structure cannot be distinguished from light that travels through a uniform structure, such that it can be considered as invisible although inhomogeneities are still present, but compensated by gain and loss. Moreover, we present the first experimental implementation of our concept in a disordered acoustic waveguide where we demonstrate that by absorbing and amplifying sound waves in a well-defined way, we can make the waveguide one-way transparent for an incoming sound wave that would otherwise get perfectly reflected in the absence of gain and loss. By adding the right loss and gain distribution to a given structure, we can not only suppress scattering in the entire structure, but also force the wave to have a predetermined intensity distribution. This concept can be used to create a strong intensity focus at a certain position even inside disordered media, which is of great interest in many fields of physics.

A conceptually different approach to cope with the presence of disorder without introducing loss and gain into the structure builds on the recent experimental breakthrough to characterize a highly complex medium by measuring its scattering matrix. Using these newly available data sets, we first show in a simple system how so-called "particle-like scattering states" – states that have a beam-like wave function – can be generated. Building up on this knowledge, we study the propagation of light waves in a smoothly correlated disorder which gives rise to the formation of a network of branches. We develop a strategy that allows us to address individual branches using particle-like states such that we can steer light through a disordered system on only a single branch rather than on multiple of them.

Using a similar concept to the one used to find particle-like states, we devise strategies for micromanipulating targets inside disordered materials in an optimal

manner. Specifically, we study how wavefronts directed from the outside onto the medium have to be shaped to manipulate a target buried inside a disorder by applying a well-defined momentum, pressure or torque as well as to achieve a focus inside the target. In addition to the introduction of our novel theoretical approach we also show a corresponding implementation in a microwave setup that demonstrates our predictions in a convincing way.

Ultimately, we show that perfect absorption of a wave's intensity can be achieved by a small absorptive element embedded inside a disordered structure by carefully shaping the incident wavefront, the wave's frequency as well as the amount of absorption. This effect of "coherent perfect absorption" is, for the first time, demonstrated experimentally in a disordered medium in a microwave setup.

With this work we hope to trigger further experiments that demonstrate the enormous potential of loss and disorder for innovation in photonics.

Contents

Introduction

Building new photonic devices is usually connected to the effort of reducing two naturally occurring ingredients spoiling the long-distance propagation of light: loss and disorder. Loss leads to an absorption of light whereas disorder causes a highly complex intensity pattern due to scattering and multi-path interference. While loss occurs in materials such as metals or black paint, disorder is induced by inhomogeneities of the system such as impurities or other imperfections. The prevailing view of staying away from these two ingredients in the fabrication process of optical devices is thus very reasonable, however, new theoretical insights and newly available experimental possibilities have recently questioned this belief.

Instead of eliminating loss, it was recently shown in several experiments that loss can induce interesting new effects in optics such as loss-induced transparency [1, 2], coherent enhancement or perfect absorption [3–7], loss-triggered lasing [8–10], loss-enhanced amplifiers [11], and loss-induced quantum phase-transitions [12]. One particular case that has been studied extensively is that of materials where loss is combined with gain in a balanced way [13, 14]. Especially structures where gain and loss follow a so-called parity-time ($\mathcal{PT}$)-symmetry [15] have recently drawn a lot of attention [15]. This new design principle for engineering structures features a plethora of remarkable characteristics [16–18] like power oscillations [2, 19], non-reciprocal transport [20–22], unidirectional invisibility [23–26], and constant-intensity waves in inhomogeneous refractive index landscapes [27–30], which play a significant role in this thesis.

While wave scattering induced by disordered media was also considered as detrimental not very long ago [31, 32], disorder has recently been proven to be a useful resource in photonic structures [33–35]. In several proof-of-principle experiments, disorder was shown to be beneficial for applications like sub-wavelength focusing [36], for enhancing transport [37, 38], for the construction of ultra-small spectrometers [39], for controlled random lasing [40–43] or for very intense laser sources without speckle [44]. A promising new approach to cope with the presence of disorder is to characterize [45, 46] as well as to control [47, 48] light fields even in strongly disordered media with so-called spatial light modulators (SLMs). It has been shown that with SLMs the wavefront can be shaped in such a way that light could be focused behind a disordered medium in space [47, 48] and time [49, 50].

This emerging new field of "wavefront shaping" has become a broad and fruitful field in modern wave physics during the last few years. The experimental accessibility of the scattering matrix of a disordered medium [45, 46, 51] that relates

all incoming with all outgoing field states, is one of the principal reasons for this progress. The information stored in this scattering matrix can nowadays be exploited for several purposes, such as to turn an arbitrary disordered medium into any desired optical instrument [52], use wavefront shaping to see through or around disorder [52–55], to enhance the information transfer rate of multi-mode fibers [56–58], or to do medical imaging with visible light [59, 60]. Since spatial light modulators become faster and allow to control even more degrees of freedom of the light field, we expect that the possibilities in wavefront shaping will continue to grow.

These recent developments make us optimistic that loss and disorder in optical systems can be controlled or can be even turned to our advantage. In the following thesis, we focus on new theoretical concepts involving loss and disorder (separately and jointly) that are both promising in terms of new functionalities as well as implementable with state-of-the-art technology in photonics.

In the upcoming chapter we give a short introduction to the scattering formalism used throughout this thesis. Specifically, we introduce the concept of the scattering matrix and show different scattering geometries that we use in the thesis.

The second chapter of this thesis is dedicated to so-called constant-intensity waves [27–30]. In general, when waves propagate through disordered structures, back-scattering occurs at inhomogeneities of the medium such that complex interference patterns in the intensity of the wave arise. These intensity variations can be completely removed by adding a tailored gain and loss distribution to the disorder. We show that by using the concept of constant-intensity waves we can make a medium invisible from one side [30] and, furthermore, present a first experimental realization of this concept in an acoustic waveguide [61] which has been carried out in collaboration with Romain Fleury's group from EPFL in Lausanne. Moreover, we present a generalization of the constant-intensity idea that allows us to create wave states with any predetermined intensity profile, such as a focus, instead of a constant intensity only [62, 63]. At the end of the second chapter we demonstrate the existence of constant-intensity waves not only in one-, but also in two-dimensional systems [64].

Even in the ballistic regime, wave scattering can be very complex leading potentially to a spatially extended wave function. In order to overcome a spreading of the wave due to multiple scattering, we introduce in the chapter thereafter the concept of the time-delay operator and so-called "particle-like states" [65, 66]. These special wave states feature a beam-like (or particle-like) wave function instead of being spread in the entire scattering region. We present the first *in situ* realization of particle-like states in a microwave cavity [67] resulting from a collaboration with Ulrich Kuhl's group from the Université Côte d'Azur. Such particle-like states can not only be investigated in the ballistic regime but also in systems with a weak and smoothly correlated disorder featuring the phenomenon of "branched flow". In such systems, an injected wave does not spread out isotropically in all directions but rather forms a distinct branching pattern along which the wave flows preferentially.

We show that these branches in the spreading pattern can be separated from each other by exploiting the time-delay operator, allowing us to steer light through a disorder along one single branch [68].

In the fourth chapter we generalize the concept of the time-delay operator to a much broader class of new operators, of which the time-delay operator is only one specific implementation. These new operators allow us to apply to a target, which can be embedded inside an arbitrarily disordered environment, a well-defined momentum, pressure or torque as well as to achieve a focus inside the target. Beside studying these new operators analytically as well as numerically, we also present experimental data from a collaboration with Ulrich Kuhl's group [69, 70].

In the last chapter we combine loss and disorder and study the phenomenon of "coherent perfect absorption" – an effect commonly referred to as "anti-lasing" because it corresponds to the time-reversed process of coherent emission of radiation [3]. Here, we investigate coherent perfect absorption in a disordered medium, which would then be the time-reversed process of a random laser at threshold [71]. We directly implement such a random anti-laser for the first time in a microwave setup – again in collaboration with Ulrich Kuhl's group – and conduct stability tests on it [7].

This thesis concludes with a summary and an outlook.

Chapter 1

Scattering formalism

A generic scattering system can be divided into two domains: the asymptotic region where the waves can be decomposed into well-defined scattering channels and the actual scattering region where the scattering process takes place. A sketch of such a scattering system is shown in Fig. 1.1(a). The scattering region (grainy area in gray) can be arbitrarily shaped, it can be filled with a disordered medium or it can include loss and/or gain. All these properties of the scattering region can be translated into an (inhomogeneous) refractive index landscape $n(\vec{r})$ with $\vec{r}$ being the position vector. In contrast to the scattering region, the refractive index of the asymptotic region [Fig. 1.1(a) surrounding white area] is uniform, i.e., $n(\vec{r}) = \text{const}$. What all scattering experiments have in common is that waves coming from the asymptotic region impinge onto the scattering region and leave the region after the scattering process. The incoming wave as well as the outgoing wave can be written as a coefficient vector with respect to a certain basis that is defined in the asymptotic region where we use the vector $\vec{u}$ to describe the incoming wave and the vector $\vec{v}$ to describe the outgoing wave. The notion behind the projects presented in this thesis is to control the behavior of the wave inside the scattering region either by shaping the incoming wave $\vec{u}$, which can be experimentally realized by using so-called spatial light modulators (SLMs) [47, 48], or by modifying the scattering region itself (e.g., by adding absorption to it).

In the following we study exclusively one- and two-dimensional, time-harmonic systems such that the out-of-plane component of the wave's electric field $\psi(\vec{r})$ can be described by the scalar Helmholtz equation (for a derivation see appendix A.1),

$$[\Delta + n^2(\vec{r})k_0^2]\psi(\vec{r}) = 0, \tag{1.1}$$

where $k_0 = 2\pi/\lambda_0$ is the wave number in the asymptotic region (with λ_0 being the wavelength) and Δ the Laplacian. For two-dimensional systems, the Laplacian Δ and the position vector $\vec{r}$ take the form $\Delta = \partial^2/\partial x^2 + \partial^2/\partial y^2$ and $\vec{r} = (x, y)^T$, respectively, whereas in one dimension they turn into $\Delta = \partial^2/\partial x^2$ and $\vec{r} = x$.

In this thesis we study, among others, two-dimensional systems where the scattering region is surrounded by hard walls forcing the wave's intensity to be zero at the boundaries. One example of such a setup with a square scattering region is
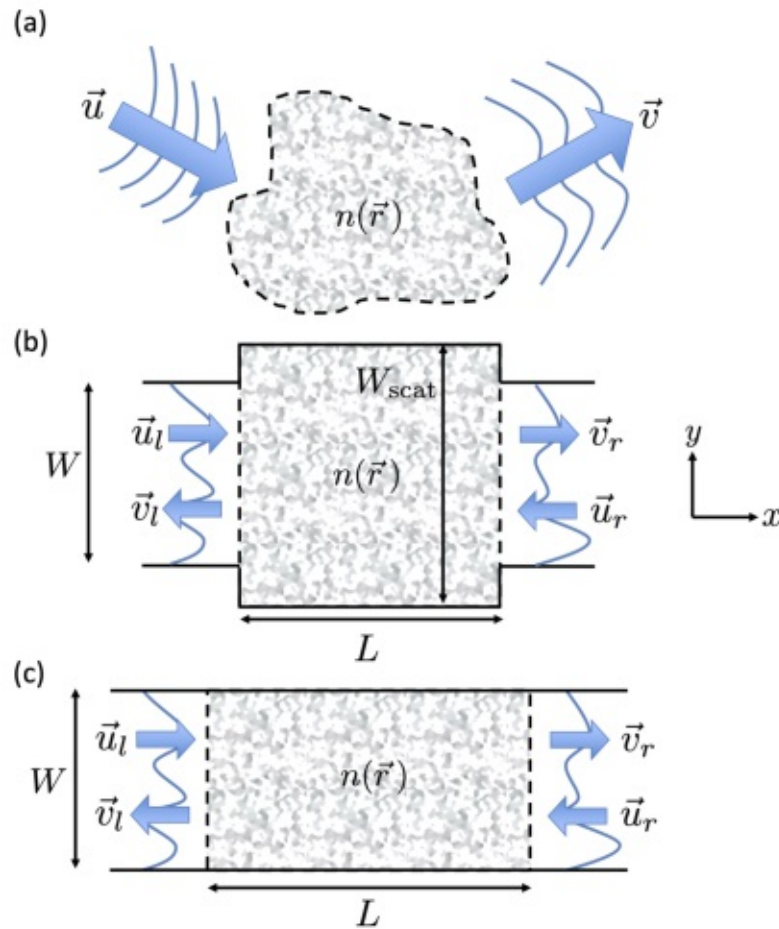
Fig 1.1: (a) Generic scattering system with a scattering region featuring a non-uniform refractive index $n(\vec{r})$ (grainy area in gray) and a uniform asymptotic region with $n(\vec{r}) = \text{const.}$ (surrounding white region). The incoming wave (described by the vector $\vec{u}$) coming from infinity propagates toward the scattering region where the wave gets scattered. The outgoing wave (described by the vector $\vec{v}$) leaves the structure into infinity. (b) One example of a scattering system is a square-shaped cavity of length L and width $W_{\text{scat}} = L$ with leads of width W attached to it on both sides. Hard-wall boundary conditions are applied on both sides of the structure (see solid black lines). The asymptotic regions are called leads through which waves can enter the scattering region ($\vec{u}_l$ and $\vec{u}_r$) and can leave it after the scattering process ($\vec{v}_l$ and $\vec{v}_r$). (c) A special case of such a two-port system is a waveguide structure where the scattering region has the same width as the leads, i.e., $W_{\text{scat}} = W$.

sketched in Fig. 1.1(b), where the hard walls are indicated by black solid lines. It consists of a square scattering region of length L and width $W_{\text{scat}} = L$ (grainy area in gray) with two semi-infinite leads of width W attached to it representing the

asymptotic regions (white areas). These leads allow waves to enter and leave the scattering region. In such two-port systems we choose the x-axis as the longitudinal propagation direction of the wave and the y-axis as the transverse direction. A special case of a two-port system is a waveguide which is studied, e.g., in Chapter 4, where the scattering region has the same width as the leads, i.e., $W_{scat} = W$ [see Fig. 1.1(c)]. Such waveguide structures are in general much longer than they are wide, i.e., $L > W$. The leads of these two-port systems are both uniform where we assume (without loss of generality) a constant refractive index of $n(x,y) = 1$ bringing the advantage that the number of basis states in which the wave can be decomposed into is finite and determined by the wavelength of the incident wave λ_0. These basis states are solutions of the Helmholtz Eq. (1.1) with a uniform refractive index $n(x,y) = 1$,

$$\psi_n(x,y) = \frac{1}{\sqrt{k_{x,n}}} \chi_n(y) e^{ik_{x,n}x}, \tag{1.2}$$

where

$$\chi_n(y) = \sqrt{\frac{2}{W}} \sin(k_{y,n}y) \tag{1.3}$$

is the transverse profile of the wave function and the prefactor $1/\sqrt{k_{x,n}}$ normalizes these states to unit flux. These solutions are called transverse modes and are characterized by an integer n, the transverse wave number $k_{y,n} = n\pi/W$ and the wave number in longitudinal direction $k_{x,n} = \sqrt{k_0^2 - k_{y,n}^2}$. The solutions in Eq. (1.2) are right-propagating waves, however, left-propagating waves are simply described by $\psi_n^*(x,y)$, where the asterisk $*$ represents the operation of complex conjugation. For $k_{y,n} \leq k_0$, the longitudinal wave number $k_{x,n}$ is real and the mode can propagate in x-direction. In the case of $k_{y,n} > k_0$, $k_{x,n}$ is purely imaginary and the mode decays exponentially (evanescent mode). Modes with a real longitudinal wave number $k_{x,n}$ are referred to as open modes and in contrast to evanescent modes they carry a finite flux. The total wave number k_0 determines the number N of open modes in a lead through $N = \lfloor Wk_0/\pi \rfloor$ with $\lfloor \ldots \rfloor$ being the floor function. As an example we show in Fig. 1.2(a) the intensity of a wave obtained when the 13-th mode, i.e., ψ_{13} as described in Eq. (1.2), is injected from the left-hand lead into a cavity as sketched in Fig. 1.1(b).

The wave states in Eq. (1.2) can be used as a basis to decompose an arbitrary wave into it since they form a complete and orthogonal set of states. Consequently, any incoming or outgoing wave can be written as a coefficient vector $\vec{u} = (\vec{u}_l, \vec{u}_r)^T$ and $\vec{v} = (\vec{v}_l, \vec{v}_r)^T$, respectively, where the indices l and r indicate the lead on the right or on the left side of the scattering region. The parts $\vec{u}_l$ and $\vec{v}_r$ are right-propagating waves, whereas $\vec{u}_r$ and $\vec{v}_l$ are left-propagating waves as is schematically shown in Fig. 1.1(b) and (c).

The most widely-used tool to describe wave scattering processes is the scattering matrix S of a system that relates incoming to outgoing wave amplitudes through $\vec{v} = S\vec{u}$. In this thesis we present concepts that exploit the information stored in this scattering matrix S to shape the incoming wave $\vec{u}$ in such a way that the resulting wave inside the scattering region shows a desired behavior. In the absence of absorption and amplification, the scattering matrix is unitary (i.e., $S^\dagger S = \mathbb{1}$), meaning that the norm of the wave is conserved. If the input wave is normalized to one ($\vec{u}^\dagger \vec{u} = 1$), the norm of the outgoing wave $\vec{v}^\dagger \vec{v} = \vec{u}^\dagger S^\dagger S \vec{u} = \vec{u}^\dagger \vec{u} = 1$ is one as well, i.e., the total flux carried by the wave is conserved. For non-Hermitian systems, i.e., systems including loss and/or gain, the scattering matrix is in general non-unitary (i.e., $S^\dagger S \neq \mathbb{1}$) and thus the norm of the wave is not conserved, i.e., $\vec{v}^\dagger \vec{v} \neq 1$.

In two-port systems as shown in Fig. 1.1(b) and (c), the scattering matrix takes the block structure

$$S = \begin{pmatrix} r & t' \\ t & r' \end{pmatrix}, \tag{1.4}$$

where r, t are the reflection and transmission matrices containing the scattering amplitudes for injection from the left side and r', t' consist of the corresponding amplitudes for injection from the right side. The matrix element t_{nm}, for example, describes the transmission from the m-th incoming mode into the n-th outgoing mode. Since reciprocity is not broken in all systems that we study in this thesis, the following symmetry relations are valid: $r = r^T$, $r' = (r')^T$, $t = (t')^T$. Breaking the reciprocity typically requires either a time-dependent dielectric function, non-linearities or an external magnetic field, which are all not considered in this thesis [35].

Until now, the scattering amplitudes were given with respect to the lead modes in Eq. (1.2), however, this choice is arbitrary and, in fact, any complete and orthogonal set of functions can be taken as a basis. An experimentally very useful basis, especially in optics, is a spatial basis, where one spatial basis element would correspond to one pixel in a spatial light modulator. One element of the transmission matrix t_{ba} measured in this pixel basis would then describe the transmission from pixel a at the input to pixel b at the output. A transformation between the transmission matrix in the modal basis [now called $t^{\{m\}}$] and the transmission matrix in the spatial basis [now called $t^{\{s\}}$] can be derived as follows: (i) we calculate the elements of the transverse position operator y in the modal basis

$$y_{nm}^{\{m\}} = \int_0^W dy\, \chi_n(y) \cdot y \cdot \chi_m(y), \tag{1.5}$$

with $\chi_n(y)$ denoting the transverse mode profiles in Eq. (1.3). (ii) We calculate the eigenbasis of the $y^{\{m\}}$-operator in Eq. (1.5). These eigenstates $\vec{y}^{(i)}$ (the index i represents the i-th eigenvector) are states with a well-pronounced intensity maximum at a transverse position specified by the corresponding eigenvalue,
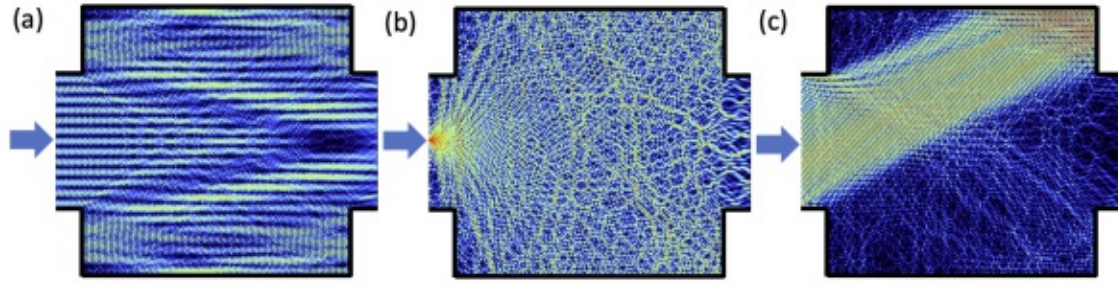
Fig 1.2: (a) Field profile of the 13-th transverse mode, i.e., ψ_{13}, as defined in Eq. (1.2) injected from the left-hand lead into the system sketched in Fig. 1.1(b). (b) Spatial eigenstate $\vec{y}^{(25)}$ showing a well-pronounced intensity maximum at the input lead. (c) Angular eigenstate $\vec{k}_y^{(14)}$ radiating into a specific direction. Both vectors, $\vec{y}^{(25)}$ and $\vec{k}_y^{(14)}$, are given with respect to the mode basis spanned by the functions in Eq. (1.2). The incident wave number is chosen in such a way that 50 transverse modes can propagate in the leads. In order to solve the Helmholtz equation numerically we use the modular recursive Green's function technique (see appendix A.5 for more details).

where one such eigenstate is shown in Fig. 1.2(b). (iii) Using these eigenstates, we obtain the transmission matrix in coordinate space by $t^{\{s\}} = Y^\dagger t^{\{m\}} Y$, where $Y = [\vec{y}^{(1)}, \vec{y}^{(2)}, \ldots, \vec{y}^{(N)}]$ contains the eigenvectors of the y-operator column-wise. In this basis, one row of $t^{\{s\}}$ describes the transmission from the entire incoming lead to only one peak on the right-hand side of the scattering geometry. The other blocks of the scattering matrix can be transformed analogously.

Another widely used basis is the angular basis, i.e., where the basis states feature a well-defined angle of injection. In order to obtain these states numerically, we calculate the elements of the operator $k_y = -i\partial/\partial y$ in the modal basis measuring the transverse y-component of the wave vector, since a well-defined transverse wave vector component corresponds to a well-defined angle of incidence. In analogy to the spatial basis, we calculate the eigenvectors $\vec{k}_y^{(i)}$ of this operator. One such eigenstate is shown in Fig. 1.2(c), where we can clearly see that the incident wave radiates into only one specific direction. In this thesis we use the eigenstates $\vec{k}_y^{(i)}$ as a basis to analyze the different angular components of an incident wave.

Having introduced the scattering formalism in this chapter, we study in the next chapter very special scattering states, namely constant-intensity waves. To make life more simple, we start introducing these waves in one-dimensional structures and generalize these waves to two dimensions later on.

Chapter 2

Non-Hermitian wave control

Any inhomogeneous index of refraction generally leads to a highly complex interference pattern in the intensity of light waves that pass through such a medium. To completely remove these intensity variations as well as any back-reflections from the inhomogeneities in the medium, a protocol was introduced that is based on system-specific gain and loss components that are added to the system in a very delicate way [27–30, 61]. The resulting constant-intensity waves (CI-waves) were first introduced for paraxial wave beams in a suitable optical potential showing variations transverse to the propagation direction of the beam [27]. In a next step we could show that this approach can be extended in a non-trivial way such that CI-waves can also be created in structures that show variations of the refractive index in propagation direction of the light [28]. Building up on this knowledge, we explore in this chapter many different aspects of shaping a wave by introducing gain and loss to a system. We show not only how to completely eliminate a wave's intensity variation to get a CI-wave but also how to create a wave with an arbitrary predetermined intensity profile [62, 63]. By carefully tuning a wave's phase information we show how to create structures that are unidirectionally invisible [30]. We also report on the first experimental realization of the CI-concept using an acoustic waveguide [61] and show that our concepts can also be transferred to two-dimensional structures [64]. In what follows, we give a short introduction into the mathematical description of CI-waves in one-dimensional systems.

2.1 Constant-intensity waves in one-dimensional structures[1]

Scalar wave scattering in one-dimensional structures is governed by the Helmholtz equation (see derivation in appendix A.1),

$$\left[\frac{\partial^2}{\partial x^2} + n^2(x) k_0^2 \right] \psi(x) = 0, \tag{2.1}$$

---

[1] The theory of CI-waves in one-dimensional scattering systems was developed together with Konstantinos Makris from the University of Crete [29].

with $n(x)$ being the refractive index, k_0 the wave number, and $\psi(x)$ the scalar, complex-valued field amplitude. We assume that the refractive index shows variations in a finite region $x \in [-L, L]$ and that it can be complex, i.e., $n(x) = n_R(x) + in_I(x)$ where $n_R(x)$ is the real part and $n_I(x)$ is the imaginary part. A negative value for $n_I(x)$ corresponds to gain (amplification) and a positive value for $n_I(x)$ to loss (absorption). A plane wave incoming from the asymptotic region $|x| > L$ with a uniform refractive index of n_0 typically scatters at the refractive index variations $n(x)$, leading, in general, to a finite back-reflection and a complicated interference pattern in the intensity. What we show now is that we can get a fringe-free intensity pattern for incident plane waves with a specific wave number k_0 provided that $n_R(x)$ and $n_I(x)$ fulfill a certain relation. In other words, adding to a structure a well-defined gain-loss distribution can eliminate all intensity variations of the wave.

The Helmholtz Eq. (2.1) is usually solved for a given refractive index (which is determined by the medium) yielding a corresponding scattering wave function $\psi(x)$. Now, we follow the reverse strategy: we fix a specific form of the wave function $\psi(x)$ and determine the corresponding refractive index $n(x)$ that supports this wave state. To be more precise, we want the wave to have the form

$$\psi(x) = A \exp\left[ik_0 \int_{-L}^{x} W(x')dx'\right], \tag{2.2}$$

with an arbitrary real-valued function $W(x)$ and a constant amplitude A. Inserting the ansatz in Eq. (2.2) into the Helmholtz Eq. (2.1) and resolving for the refractive index yields

$$n^2(x) = W^2(x) - \frac{i}{k_0}\frac{\partial W(x)}{\partial x}. \tag{2.3}$$

In other words, injecting a plane wave with wave number k_0 into a structure with a refractive index described by Eq. (2.3), we get a wave that follows the solution in Eq. (2.2) having a constant intensity $I = |\psi(x)|^2 = |A|^2$ anywhere inside the structure. Solving Eq. (2.3) for $n_R(x)$ and $n_I(x)$, we get

$$n_R(x) = \frac{W(x)}{\sqrt{2}}\left\{1 + \left[1 + \frac{W'^2(x)}{W^4(x)k_0^2}\right]^{\frac{1}{2}}\right\}^{\frac{1}{2}}, \tag{2.4}$$

$$n_I(x) = -\frac{1}{2k_0}\frac{W'(x)}{n_R(x)}, \tag{2.5}$$

with $W'(x) = \partial W(x)/\partial x$. From these equations we can see that for $W(x) = \text{const.} = W_0$ the imaginary part of the index goes to zero, i.e., $n_I(x) = 0$, and the real part becomes $n_R(x) = W_0$, which is the trivial case of a plane wave traveling through a uniform material with $n_R(x) = W_0$. Thus, non-trivial CI-waves can only exist in systems featuring gain and loss, i.e., $n_I(x) \neq 0$. In the following work we

only consider structures with $n_R(x) \geq 1$, such that the function $W(x)$ has to be larger than 1 [see Eq. (2.4)].

The solution in the entire space, i.e., including the asymptotic regions (with index of refraction n_0) in front of and behind the cavity reads as follows,

$$\psi(x) = \begin{cases} A \, \exp[ik_0 n_0 \, (x + L)], & x < -L \,, \\ A \, \exp[ik_0 \int_{-L}^{x} W(x')dx'], & -L \leq x \leq L \,, \\ A \, \exp[ik_0 n_0 \, (x - L)], & x > L, \end{cases} \tag{2.6}$$

where one can easily see that the wave has a constant intensity, $I(x) = |\psi(x)|^2 = |A|^2$, in the asymptotic regions [where $n(x) = n_0$] as well as inside the cavity where the refractive index varies.

In a last step we have to find the appropriate boundary conditions for the function $W(x)$. Since a CI-wave is a wave traveling from the left-hand asymptotic region into positive x-direction without back-reflections, the corresponding boundary conditions at $x = \pm L$ are perfect transmission boundary conditions,

$$\frac{\partial \psi}{\partial x}(\pm L) = ik_0 n_0 \psi(\pm L), \tag{2.7}$$

resulting in the following condition for $W(x)$: $W(L) = n_0 = W(-L)$.

We emphasize here that a CI-wave is associated with a specific incidence direction. Here, incidence is assumed from the left (in positive x-direction), such that injecting a plane wave with the same wave number k_0 from the other incidence direction, i.e., from the right (in negative x-direction), one gets finite reflections and non-trivial intensity variations inside the structure. Due to Lorentz-reciprocity, however, one would still get unit transmission.

In order to elucidate the above ideas we consider in the following one specific CI-refractive index. To construct such a refractive index distribution $n(x)$, we choose an arbitrary function $W(x)$ that fulfills the boundary condition in Eq. (2.7). Consider first the refractive index calculated from Eq. (2.3) obtained from a generating function $W(x) = n_0 + f(x)$ where n_0 is the asymptotic refractive index and $f(x)$ is a superposition of 12 randomly placed Gaussian functions. The corresponding complex refractive index is shown in Fig. 2.1(a) and (b), where the real part is shown in gray and the imaginary part in green (loss) and red (gain). In Fig. 2.1(c) we display the intensity of the scattering state at the design wave number k_0 for the two cases with the gain-loss distribution added (magenta line) and without it (blue line). We can clearly see that the wave's intensity shows strong variations in the Hermitian case, whereas the intensity is constant for the system including gain and loss. In other words, the interplay of gain and loss makes the wave lose all its interference fringes resulting in a wave with a constant intensity.

Our example shows that for a plane wave at an incident wave number k_0, we can add a corresponding gain-loss landscape, such that the wave gets perfectly transmitted and has no spatial variations in its intensity pattern. A natural question one
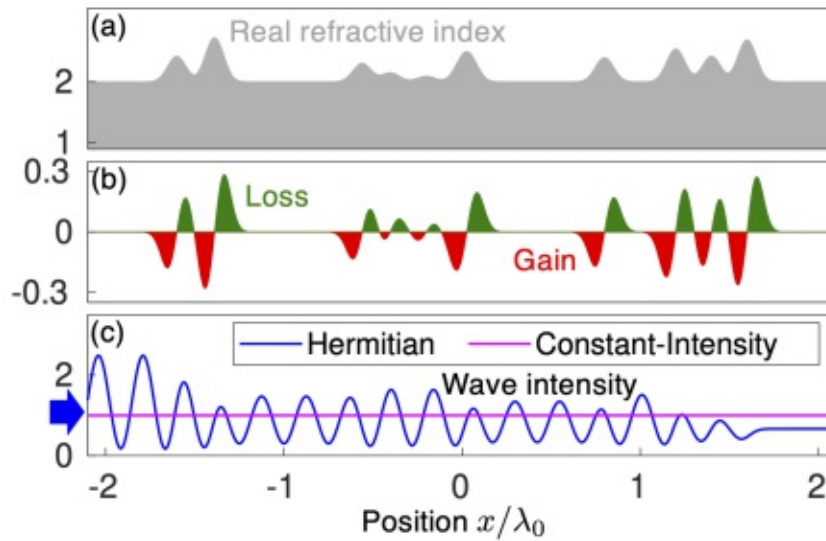
Fig 2.1: (a), (b) Real (gray) and imaginary (red: gain, green:loss) parts of the refractive index for a CI-system calculated from Eq. (2.3) with a generating function $W(x) = n_0 + f(x)$, where $f(x)$ is the superposition of 12 randomly placed Gaussian functions with different amplitudes (amplitudes uniformly distributed between 0 and 1) and the same standard deviation $\sigma = 0.5\lambda_0$. The asymptotic refractive index is $n_0 = 2$ and the wave number is $k_0 = 2\pi/0.2$. (c) Intensity of the scattering state for a plane wave with wave number k_0 and amplitude $A = 1$ injected from the left into the system for the structure including gain and loss (magenta line) and without gain and loss (blue line). As we can see, the non-Hermitian components make the wave perfectly transmitting without any intensity variations. The calculations were performed using the transfer-matrix method (see appendix A.2 for more details).

may ask at this point is what happens to incident plane waves with detuned wave numbers $k = k_0 \pm \Delta k$ assuming active materials that are characterized by approximately flat dispersion curves near the values of the wavelength of operation. One may expect that the emergence of CI-waves is a sharp resonance phenomenon, such that waves with a slightly detuned wave number k would show a completely different behavior just like for a resonance in a Fabry-Pérot interferometer [72]. This turns out to be a misleading picture. Since the CI-wave function at position x, $A \exp[\mathrm{i} k_0 \int_{-L}^{x} W(x') dx']$, only depends on the generating function $W(x')$ at $x' < x$, one can easily truncate the structure at any point x and still get a CI-wave. We have to make sure however, that one continues the system for all $x > x'$ with a constant generating function having the same value as at the point of truncation (provided that the transition to the asymptotic value is continuous). This observation indicates that CI-refractive indices are not only reflectionless in total but also unidirectional at any point inside the structure. Perfect transmission in such

systems is thus not a resonance phenomenon (as resulting from a back and forth propagation of waves), suggesting that CI-waves are stable against changes of the incident wavelength.

In order to test this broadband stability we take the structure from Fig. 2.1 that is designed to support a CI-wave for incident plane waves with wave number k_0 and inject plane waves with detuned wave numbers $k \neq k_0$. To be more precise, Fig. 2.2(a) shows the transmission spectrum, i.e., the transmittance $T = |t|^2$ as a function of the wave number detuning $\delta = k - k_0$, for the Hermitian system (blue line) and for the CI-system (magenta line) shown in Fig. 2.1. We see, first of all, that the CI-system is close to perfectly transmitting not only at $k = k_0$ (i.e., $\delta = 0$) but also in a broad frequency range around k_0 (between $\delta = -2$ and $\delta = 2$), whereas the Hermitian system strongly deviates from unit transmittance. Figure 2.2(b) shows the difference between the transmission phase ϕ_t of a wave propagating through the Hermitian or through the CI-system and the transmission phase of a wave propagating through a uniform material with index n_0, $\phi_0 = 2Lkn_0$. In Fig. 2.2(c) we can see the difference between the corresponding transmission time-delay $\tau_t = \partial\phi_t/\partial k$ [73] compared to the time-delay a wave suffers from propagating through a uniform material $\tau_0 = \partial\phi_0/\partial k$. We see that not only the transmittance but also the time-delay is very stable compared to the Hermitian system. Figure 2.2 thus clearly demonstrates the broadband frequency stability of CI-waves.

Given the function $W(x)$, the corresponding refractive index distribution $n(x)$ can be directly determined via Eq. (2.3) and vice versa. The same is, however, not true if, as a starting point, the real part of the refractive index $n_R(x)$ is known instead (typical situation in many realistic cases). One would have to solve the differential equations (2.4) and (2.5), which turns out to be a very challenging task. We tackled this problem, instead, with a deep-learning based approach and show that we can indeed find the corresponding gain-loss profile $n_I(x)$ with a very high precision when the refractive index distribution $n_R(x)$ is given (see Ref. [74] for details).

Due to the fact that the phase of CI-waves is given as the integral over the generating function $W(x)$, one can create a scattering state with a predetermined phase profile by fixing $W(x)$. This fact can be used to hide the information about the scattering region by delicately choosing $W(x)$ and thus making it unidirectionally invisible, as presented in the next section.
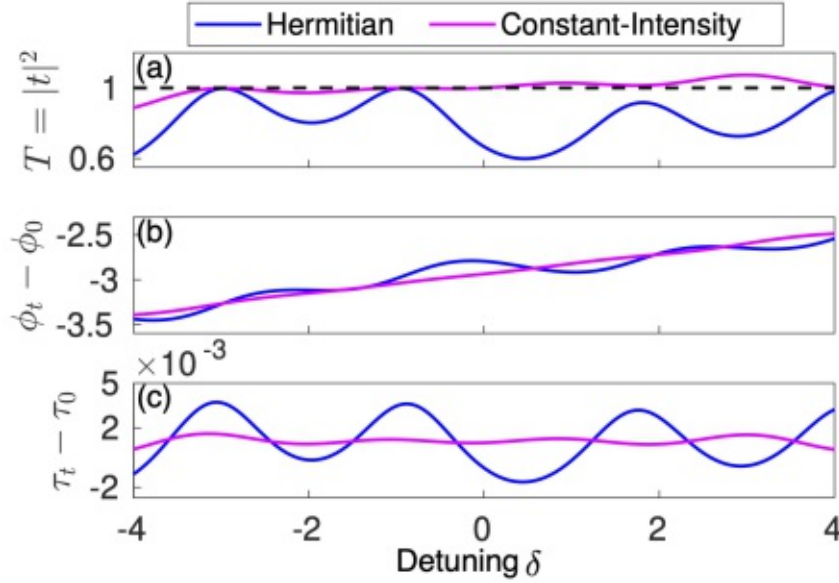
Fig 2.2: (a) Transmission spectrum of the Hermitian (blue line) and CI (magenta line) system shown in Fig. 2.1 as a function of the wave number detuning $\delta = k - k_0$. (b) Transmission phase ϕ_t minus the phase that the wave would accumulate in a uniform material $\phi_0 = 2Lkn_0$ for the Hermitian and CI-system. (c) Difference between the corresponding time-delays $\tau_t - \tau_0 = \partial\phi_t/\partial k - \partial\phi_0/\partial k$. For the CI-system the transmittance in (a) is close to unity, and the time-delay is considerably stable in a broad interval. The reference values of perfect transmittance is indicated by the horizontal dashed line in (a). The relative width of the stability window between $\delta = -2$ and $\delta = 2$ is $\Delta\delta/k_0 \approx 4/31.42 \approx 0.13$, i.e., a wave number detuning of around 6% from k_0 in both directions still allows for perfect transmission.

2.2 Unidirectionally invisible constant-intensity waves[2]

From quantum mechanics textbooks we know that the Hamiltonian of a system has to be Hermitian to ensure that its eigenvalues are real. Recently it was shown, however, that there exists a whole class of non-Hermitian Hamiltonians that possess real spectra as long as they fulfill a so-called parity-time ($\mathcal{PT}$)-symmetry [15]. A Hamiltonian H is called $\mathcal{PT}$-symmetric if it commutes with the $\mathcal{PT}$-operator, i.e., $[\mathcal{PT}, H] = 0$. The $\mathcal{PT}$-operator is a combination of the parity-operator $\mathcal{P}$, flipping the spatial coordinate $x \to -x$, and the time-reversal operator $\mathcal{T}$ that performs a

---

[2] The text in this section partially goes back to our published work in Ref. [30], from which also the figures were taken. All numerical simulations were performed by myself whereas the theoretical analysis and data evaluation was carried out in collaboration with Konstantinos Makris from the University of Crete.

complex conjugation i $\to$ $-$i, i.e., it turns gain into loss (and vice versa) and changes the propagation direction of the waves. In optics, a system is $\mathcal{PT}$-symmetric if its refractive index $n(x)$ is invariant under the application of the $\mathcal{PT}$-operator, i.e., $\mathcal{PT}n(x) = n_R(-x) - in_I(-x) = n(x)$. In order so satisfy this relation, the real part of the refractive index has to be an even function, $n_R(x) = n_R(-x)$, and the imaginary part an odd function, $n_I(x) = -n_I(-x)$, of the spatial coordinate x.

One of the most successful concepts in the field of $\mathcal{PT}$-symmetric optics is the idea to make periodic gratings unidirectionally invisible by adding loss and gain to them in a well-controlled way [24]. Such systems feature zero reflection for waves incident from one side of the structure while the reflection for the other side is increased. Moreover, waves feature unit transmission (for injection from both sides) and accumulate a phase along the two propagation directions that is the same as in the absence of the structure. The first theoretical proposal for such unidirectionally invisible structures [24] drew considerable attention and was already successfully implemented in several experiments [23, 25, 26]. It was soon shown that the invisibility of such structures breaks down for long systems, which, however, can be fixed by a modification of the refractive index [75, 76]. The idea of invisible non-Hermitian structures was later extended to non-$\mathcal{PT}$-symmetric structures, which, however, are restricted to layered and periodic systems [77, 78] or to structures where the corresponding dielectric function has to be analytic in one half of the complex position plane (in terms of spatial Kramers-Kronig relations) [79–81]. In spite of the intense research activities related to this novel topic, the question of whether this concept can also be generalized to aperiodic, non-$\mathcal{PT}$-symmetric, and non-analytic refractive indices remains to be answered.

Here, we propose such a general design principle for unidirectionally invisible structures that are unrestricted in their spatial shape. This design principle is based on the concept of CI-waves which is presented in the previous section where we show that a plane wave with wave number k_0 incident from the left asymptotic region $x < -L$ will feature a constant intensity inside the non-uniform scattering region $-L < x < L$. While it will also be perfectly transmitted to the right asymptotic region $x > L$, the structure still imprints information on its shape onto the transmission phase ϕ_t of the outgoing plane wave. Here, we present a way to eliminate the possibility of detecting such structures even through phase measurements. To achieve this goal, we choose the generating function [which is used to calculate a CI-refractive index via Eq. (2.3)] to be of the form

$$W(x) = n_0 + f(x), \tag{2.8}$$

where n_0 is again the refractive index of the asymptotic regions and $f(x)$ an arbitrary real-valued function that should satisfy

$$\int_{-L}^{L} f(x)dx = 0. \tag{2.9}$$

This function $f(x)$ describes the phase the CI-wave accumulates in addition to the propagation through a uniform medium with constant refractive index n_0. In other words, enforcing Eq. (2.9) is equivalent to demanding that this additionally accumulated phase vanishes. Specifically, the transmission phase of a CI-wave is given by $\phi_t = k_0 \int_{-L}^{L} W(x)dx$ which turns into the simple expression $\phi_t = 2k_0 L n_0$ for a wave traveling through a CI-system derived from the generating function Eq. (2.8) with the condition in Eq. (2.9). This transmission phase is equal to the phase a wave would accumulate by propagating through a uniform scattering region with index n_0 of length $2L$. In such systems, neither the transmitted intensity nor the transmission phase then reveals whether the refractive index is uniform with n_0 or an inhomogeneous refractive index. Due to the frequency stability of CI-waves (see Fig. 2.2), also the time-delay $\tau = \partial\phi_t/\partial k$ is the same as obtained in the uniform system, not only at the design wave number k_0, but rather in a broad frequency window.

In order to test our predictions, we start by considering first the refractive index distribution as provided in Eq. (2.8), where $f(x)$ consists of 12 randomly placed Gaussians with the same height and the same width but with six of them having a positive amplitude and six of them having a negative amplitude, thus enforcing the condition shown in Eq. (2.9). The corresponding complex refractive index calculated with Eq. (2.3) is shown in Fig. 2.3(a) and (b), in analogy to Fig. 2.1. The intensity of a plane wave at the design wave number k_0 for the two cases with the gain-loss distribution added (magenta line) and without it (blue line) is shown in Fig. 2.3(c). For the Hermitian case (blue line) we can clearly see the strong variations of the wave's intensity, whereas the intensity is constant for the system including gain and loss. In order to check if the system at hand is unidirectionally invisible, we study now several quantities.

Figure 2.4(a) shows the transmission spectrum, i.e., the transmittance $T = |t|^2$ as a function of the wave number detuning $\delta = k - k_0$, for the Hermitian system (blue line) and for the CI-system (magenta line) shown in Fig. 2.3. We can see that the CI-system is close to unit transmission not only at the design wave number $k = k_0$ (i.e., $\delta = 0$) but also in a broad frequency range around k_0 (between $\delta = -2$ and $\delta = 2$). Quite in contrast, the Hermitian system shows strong deviations from unit transmission. Figure 2.4(b) shows the difference between the transmission phase ϕ_t of a wave propagating through the Hermitian or through the CI-system compared to the transmission phase of a wave propagating through a uniform material with index n_0, $\phi_0 = 2Lkn_0$. We see that for the CI-system the difference is close to zero in a broad frequency interval. In Fig. 2.4(c) we can see the difference between the corresponding time-delay τ_t compared to the time-delay a wave suffers from propagating through a uniform material $\tau_0 = \partial\phi_0/\partial k$. Also here, the CI-system features the same values as the corresponding uniform system. Figure 2.4 thus clearly shows that the CI-system in Fig. 2.3 cannot be distinguished from a uniform system such that it is indeed invisible from the left around the target wave number k_0.
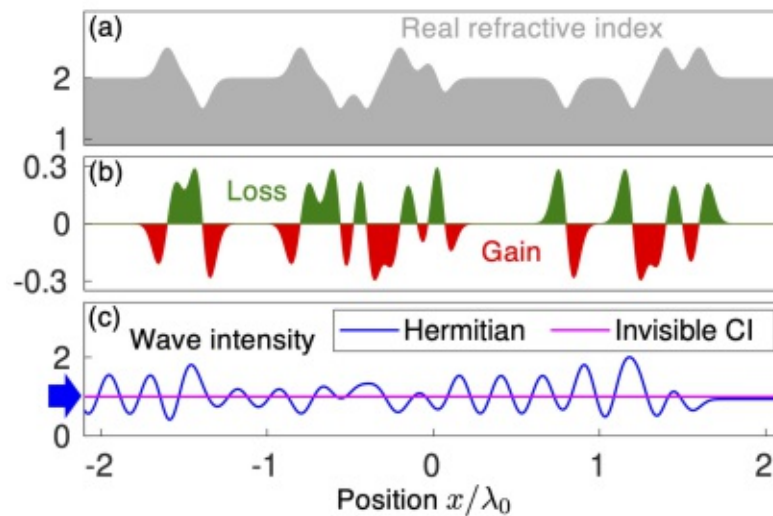
Fig 2.3: (a) and (b) Real (gray) and imaginary (red: gain, green:loss) parts of the refractive index for a CI-system. The system follows a generating function $W(x) = n_0 + f(x)$, where $f(x)$ is the superposition of 12 randomly placed Gaussian functions, with six of them having a positive amplitude and six of them having a negative amplitude, as is dictated by Eq. (2.9). The asymptotic refractive index is $n_0 = 2$, and the wave number $k_0 = 2\pi/0.2$. (c) Intensity of the scattering state for a plane wave with wave number k_0 and amplitude $A = 1$ injected from the left into the system for the structure including gain and loss (magenta line) and without gain and loss (blue line). As we can see, the non-Hermitian components make the wave perfectly transmitting without any intensity variations

After showing that the invisibility concept works for the simple system shown in Fig. 2.3, we now demonstrate its general applicability. To be more precise, we show that we can even make a strongly disordered structure, whose strong variations in the refractive index lead to Anderson localization, unidirectionally invisible. Our starting point to generate such a disorder is a generating function in Eq. (2.8), with $f(x)$ being a superposition of $N = 3000$ Gaussians with random widths, heights, and positions satisfying the invisibility condition in Eq. (2.9). The choice of using partially overlapping Gaussians for generating the disorder is just for convenience here: any other arbitrary, but smooth, function $f(x)$ satisfying Eq. (2.9) can also be used. In analogy to Fig. 2.3, we show the real and imaginary parts of the refractive index in Fig. 2.5(a) and (b), respectively.

Before studying the invisibility property of this refractive index, we first show that the disordered structure in Fig. 2.5(a) gives rise to Anderson localization in the absence of gain and loss. To prove this explicitly, we determine its localization length ξ, which quantifies the strength of the exponential decrease of the transmittance $T = |t|^2$ as a function of the system's total length $L_{\text{tot}} = 2L$. This localization
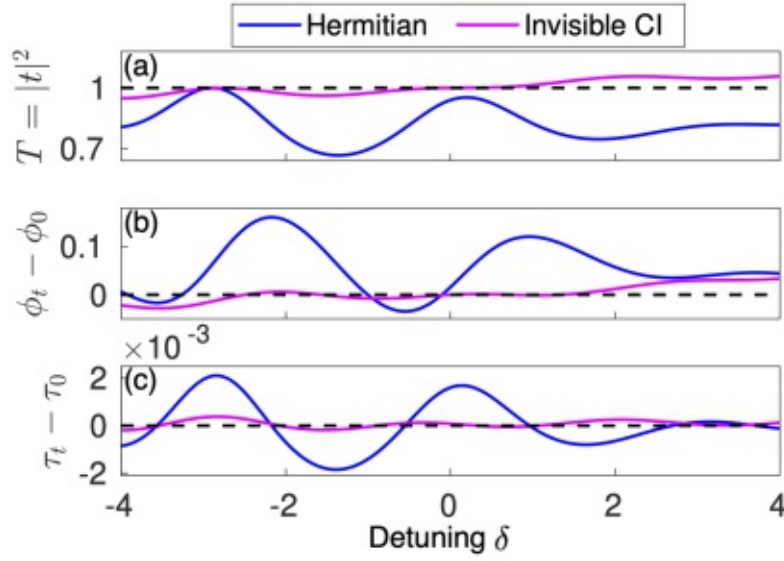
Fig 2.4: (a) Transmission spectrum of the Hermitian (blue line) and invisible CI (magenta line) system shown in Fig. 2.3 as a function of the wave number detuning $\delta = k - k_0$. (b) Transmission phase ϕ_t minus the phase that the wave would accumulate in a uniform material $\phi_0 = 2Lkn_0$ for the Hermitian and invisible CI-system. (c) Difference between the corresponding time-delays $\tau_t - \tau_0 = \partial\phi_t/\partial k - \partial\phi_0/\partial k$. For the invisible CI-system the transmittance in (a) is close to unity, and the other two quantities in (b) and (c) are close to zero in a broad interval. The reference values of perfect transmittance, zero phase difference, and zero time-delay, which are necessary for a system to be perfectly invisible, are indicated by the horizontal dashed lines. The relative width of the invisibility window between $\delta = -2$ and $\delta = 2$ is $\Delta\delta/k_0 \approx 4/31.42 \approx 0.13$, i.e., a wave number detuning of around 6% from k_0 in both directions still allows for unit transmission and zero accumulated phase. In order to quantify the deviations from perfect invisibility, we calculate the mean square deviation (MSD) within the invisibility window of the transmittance from unit transmission ($T = 1$), the MSD of the phase difference from zero extra phase ($\phi_t - \phi_0 = 0$) and the MSD of the time-delay difference from zero extra time-delay ($\tau_t - \tau_0 = 0$). To get a reference value, we evaluate all deviations for the corresponding Hermitian system as well. We get the following results: $\mathrm{MSD}(T)_{\mathrm{Herm}} \approx 5.01 \cdot 10^{-2}$, $\mathrm{MSD}(T)_{\mathrm{CI}} \approx 6.9 \cdot 10^{-4}$, $\mathrm{MSD}(\phi_t - \phi_0)_{\mathrm{Herm}} \approx 6.72 \cdot 10^{-3}$, $\mathrm{MSD}(\phi_t - \phi_0)_{\mathrm{CI}} \approx 1.98 \cdot 10^{-5}$, $\mathrm{MSD}(\tau_t - \tau_0)_{\mathrm{Herm}} \approx 1.34 \cdot 10^{-6}$, $\mathrm{MSD}(\tau_t - \tau_0)_{\mathrm{CI}} \approx 1.37 \cdot 10^{-8}$. The small deviations from perfect invisibility (see horizontal dashed lines) turn out to be around two orders of magnitude smaller for the CI-system than for the Hermitian system.

length ξ can be estimated by $\xi = -2L_{\mathrm{tot}}\langle\ln[T(L_{\mathrm{tot}})]\rangle^{-1}$, where the brackets $\langle\ldots\rangle$ denote the average value over 1000 random configurations at a given system length L_{tot}. In Fig. 2.5(d) we plot $\langle\ln[T(L_{\mathrm{tot}})]\rangle$ over L_{tot}, from which we can estimate the
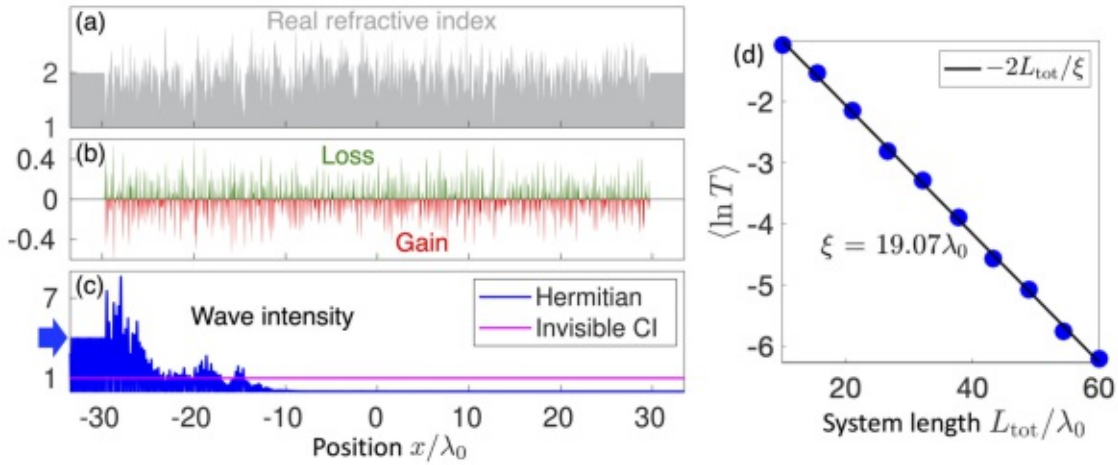
Fig 2.5: (a) and (b) Real (gray) and imaginary (red: gain, green:loss) parts of the refractive index for a strongly disordered CI-system. We use a generating function of the form Eq. (2.8), where $f(x)$ is a superposition of $N = 3000$ Gaussian functions with different widths (σ is uniformly distributed between $0.04\lambda_0$ and $0.05\lambda_0$), heights (uniformly distributed between 0 and 0.22), and positions, satisfying the invisibility condition in Eq. (2.9). The asymptotic refractive index is $n_0 = 2$, and the wave number $k_0 = 2\pi/0.2$. (c) Intensity of the scattering state for a plane wave with wave number k_0 and amplitude $A = 1$ injected from the left into the system for the structure including gain and loss (magenta line) and without gain and loss (blue line). As can be seen, the non-Hermitian components make the wave perfectly transmitting and free of any intensity variations. (d) Logarithmic transmittance averaged over 1000 random configurations of the system shown in (a) as a function of the system's total length $L_{\text{tot}} = 2L$. We fit the data to the black line $2L_{\text{tot}}/\xi$, whose slope we can use to estimate the localization length $\xi \approx 19\lambda_0$.

localization length ξ through a fit with $-2L_{\text{tot}}/\xi$ (black line). We find that the localization length is $\xi \approx 19\lambda_0$, such that the disordered structure in Fig. 2.5 is around three times longer than the localization length ξ and therefore deep in the localized regime. As a consequence, the wave gets hardly transmitted [see Fig. 2.5(c) blue line] in the Hermitian system, whereas in the non-Hermitian case (magenta line) it gets perfectly transmitted featuring a constant intensity.

In Fig. 2.6 we show that even such a strongly disordered system is unidirectionally invisible. It can be seen that the CI-system yields not only the same transmittance [see Fig. 2.6(a)] but also the same transmission phase [see Fig. 2.6(b)] and the same time-delay [see Fig. 2.6(c)] as the corresponding uniform system. We thus conclude that the disordered structure in Fig. 2.5, which in the absence of gain and loss is in the regime of Anderson localization, can be turned completely invisible by adding the correct gain-loss refractive index distribution to it.
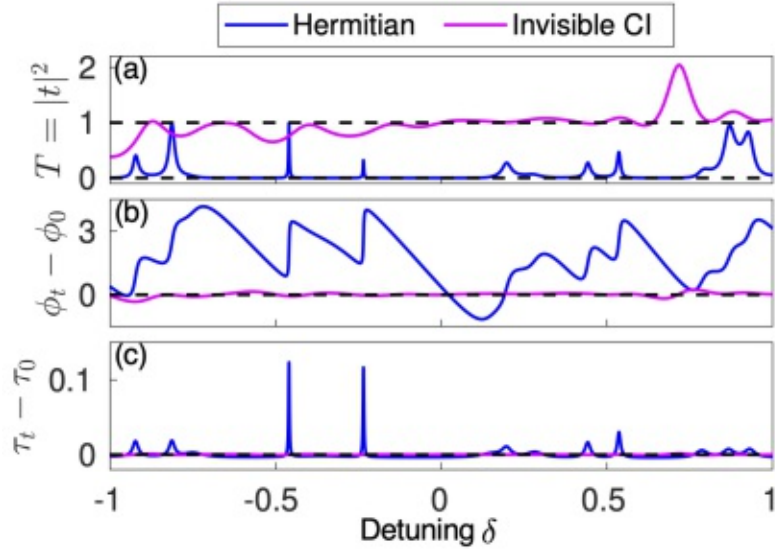
Fig 2.6: (a) Transmittance, (b) difference between the transmission phase, and (c) difference between the time-delay of the Hermitian (blue line) and invisible CI (magenta line) system shown in Fig. 2.5 as a function of the detuning $\delta = k - k_0$. All quantities indicate that even such a disordered system is invisible for left-incident waves in a broad frequency rang between $\delta = -0.5$ and $\delta = 0.5$. The relative width of the invisibility window is $\Delta\delta/k_0 \approx 1/31.42 \approx 0.03$; i.e., a wave number detuning of around 1.5% from k_0 in both directions still allows for unit transmission and zero accumulated phase, which is significantly broader than a resonance in the Hermitian system. The deviations from perfect invisibility (see horizontal dashed lines) are calculated as described in the caption of Fig. 2.4. We get the following values: $\mathrm{MSD}(T)_{\mathrm{Herm}} \approx 9.43 \cdot 10^{-1}$, $\mathrm{MSD}(T)_{\mathrm{CI}} \approx 1.29 \cdot 10^{-2}$, $\mathrm{MSD}(\phi_t - \phi_0)_{\mathrm{Herm}} \approx 3.94$, $\mathrm{MSD}(\phi_t - \phi_0)_{\mathrm{CI}} \approx 1.9 \cdot 10^{-3}$, $\mathrm{MSD}(\tau_t - \tau_0)_{\mathrm{Herm}} \approx 8.32 \cdot 10^{-5}$, $\mathrm{MSD}(\tau_t - \tau_0)_{\mathrm{CI}} \approx 2.94 \cdot 10^{-8}$, i.e., the deviations for the invisible CI-system are around two orders of magnitude smaller than for the Hermitian system.

As shown in the previous as well as in the current section, CI-waves are very robust to changes of the incident frequency. We now make use of this broadband stability to test whether we can even launch pulses through our unidirectionally invisible structures. As shown above, such structures should feature the same time-delay as a pulse propagating through the corresponding uniform structure. We first show in Fig. 2.7(a) the propagation of a pulse through the same disordered Hermitian system as in Fig. 2.5 at three different time steps ($t_1 < t_2 < t_3$). As expected, for the Hermitian system in the strong scattering regime the pulse diffracts already considerably at the beginning of the structure. In strong contrast, we can see that the pulse in the corresponding invisible CI-system [see Fig. 2.7(b)] propagates through the system while maintaining its initial shape throughout the entire

scattering region. We compare now this situation to a pulse propagating through a uniform system with the asymptotic index value $n_0 = 2$ [see Fig. 2.7(c)], and see, that both pulses arrive at the end of the structure in the same shape and at the same time (as indicated by the vertical dashed line). Thus, adding the appropriate gain-loss distribution to a disordered structure allows us to make the system not only perfectly transmitting for pulses but even completely invisible for them.
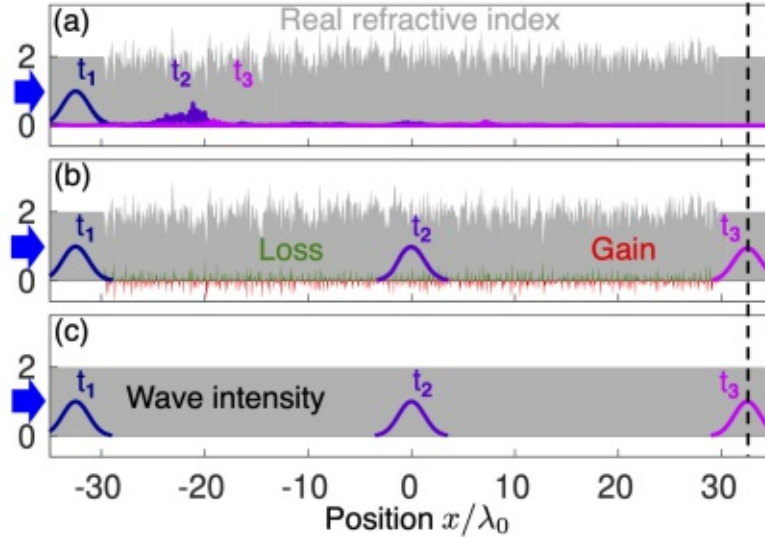

Fig 2.7: Pulse propagating through (a) the disordered Hermitian system of Fig. 2.5, (b) the corresponding invisible CI-system, and (c) a uniform system at three different time steps, $t_1 < t_2 < t_3$. Whereas the pulse diffracts rather fast in the Hermitian structure [see (a)], it gets perfectly transmitted through the CI-system [see (b)] while maintaining its initial shape. Moreover, the pulse takes the same time to propagate through the structure as through a uniform system [see (c)]. The Fourier spectrum of the pulse is Gaussian-shaped with a standard deviation of $\sigma \approx 0.045 k_0$.

In the last part of this section we show that the unidirectionally invisible Bragg grating proposed in Ref. [24] coincides with one example of our family of invisible structures at specific parameter configurations. When moving away from these parameter values, the $\mathcal{PT}$-symmetric Bragg grating loses its invisibility property, whereas our system stays invisible. We start by introducing the Bragg grating from Ref. [24] which follows a $\mathcal{PT}$-symmetric and periodic refractive index modulation:

$$n(x) = n_0 + n_1 \cos(2\beta x) + i n_2 \sin(2\beta x), \tag{2.10}$$

with β being the spatial periodicity of the grating. At the Bragg point ($\beta = k_0$) and with $n_1 = n_2 = 10^{-3}$ and $n_0 = 1$, the structure becomes unidirectionally invisible for left-incident waves and strongly reflecting for waves incident from the right. The CI-system that this Bragg grating coincides with can be derived with Eq. (2.3)

from a generating function $W(x) = n_0 + f(x)$ featuring $f(x) = n' \cos(2\beta' x)$, which satisfies the invisibility condition in Eq. (2.9):

$$
\begin{aligned}
n(x) &= \sqrt{W^2(x) - \frac{\mathrm{i}}{k_0} \frac{\partial W(x)}{\partial x}} \\
&= n_0 \sqrt{1 + \frac{n'^2}{n_0^2} \cos^2(2\beta' x) + \frac{2n'}{n_0} \cos(2\beta' x) + \mathrm{i} \frac{2\beta' n'}{k_0 n_0^2} \sin(2\beta' x)}. \quad (2.11)
\end{aligned}
$$

Assuming that $n' = 10^{-3}$ (in analogy to Ref. [24]), we can neglect in Eq. (2.11) the term which is proportional to n'^2 and consider the other two terms, which are proportional to n', as small, allowing us to approximate the square root $\sqrt{1 + x} \approx 1 + x/2$ for small x [with $x = \frac{2n'}{n_0} \cos(2\beta' x) + \mathrm{i} \frac{2\beta' n'}{k_0 n_0^2} \sin(2\beta' x)$]. We end up with $n(x) \approx n_0 + n' \cos(2\beta' x) + \mathrm{i} \frac{\beta' n'}{k_0 n_0} \sin(2\beta' x)$, which turns out to match exactly the expression in Eq. (2.10) if $n' = n_1 = n_2 = 10^{-3}$, $n_0 = 1$ and $\beta' = \beta = k_0$. This strongly indicates that the unidirectionally invisible Bragg grating in Ref. [24] is in fact a refractive index that supports CI-waves which also satisfies the invisibility condition in Eq. (2.9).

The CI-structure in Eq. (2.11) has the big advantage that it is invisible for all values of β', n_0 and n'. In other words, the structure is neither restricted to the Bragg point $\beta' = k_0$ nor to small index variations n' as the structure in Eq. (2.10). To prove our statement numerically, we perform the same calculations as in Fig. 2.4 and Fig. 2.6 but now for two different systems: the first one (see Fig. 2.8 blue lines) is the Bragg grating defined in Eq. (2.10) away from the Bragg point, $\beta = 0.7k_0$, and for larger index variations $n_1 = n_2 = 0.5$, whereas the second one (see Fig. 2.8 magenta lines) is our invisible CI-refractive index in Eq. (2.11) with the same parameters ($\beta' = \beta$, $n' = n_1 = n_2$). From Fig. 2.8(a) we can see that the Bragg grating can be detected already by measuring the transmittance at different frequencies, whereas the CI-system has unit transmittance in a broad frequency window. Also the transmission phase [see Fig. 2.8(b)] and the time-delay [see Fig. 2.8(c)] indicate that the CI-system is invisible – quite in contrast to the Bragg grating. Figure 2.8 thus demonstrates that the CI-system in Eq. (2.11) is invisible per construction for arbitrary parameters n_0, n' and β', whereas the Bragg grating in Eq. (2.10) is only invisible for the parameters used in Ref. [24].

To conclude this section, we show that the interplay of gain and loss allows for a class of unidirectionally invisible systems that are very robust with respect to frequency variations and do not satisfy any spatial symmetries. Our approach constitutes a broadly applicable generalization of earlier concepts restricted to periodic, layered, or to refractive indices that are analytic in one half of the complex position plane. We show that even disordered systems, which, in the absence of gain and loss, give rise to Anderson localization, can be made unidirectionally invisible using our approach. The frequency stability of CI-waves even allows us to
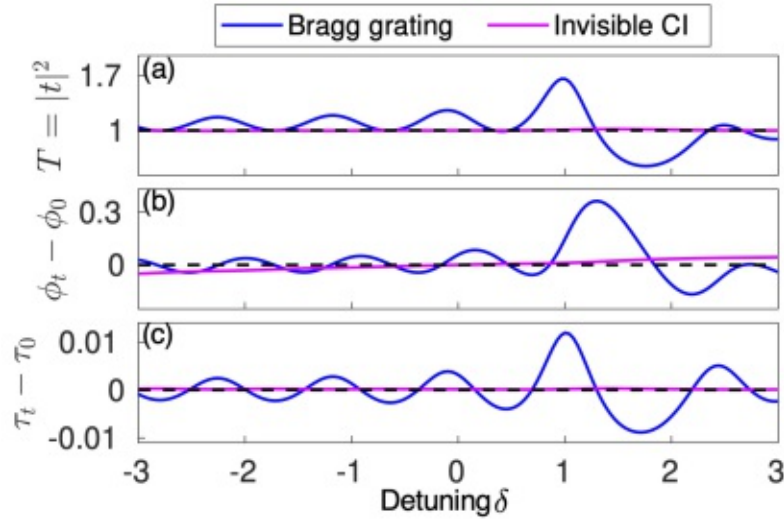
Fig 2.8: (a) Transmittance, (b) difference in the transmission phase and (c) difference in the time-delay for the Bragg structure in [Eq. (2.10)] (blue line) with different parameters for n_0, n_1, n_2, β as in Ref. [24] and for the CI-system [Eq. (2.11)] (magenta line) as a function of the detuning $\delta = k - k_0$, with the following parameters: $n_0 = 2$, $n' = n_1 = n_2 = 0.5$, $\beta' = \beta = 0.7k_0$ and $k_0 = 2\pi/0.2$. The system's length is $\approx 7\lambda_0$. All quantities indicate that the CI-system is unidirectionally invisible in a broad frequency window, whereas the Bragg grating from Eq. (2.10) can already be detected by measuring the (frequency dependent) transmittance. The relative width of the invisibility window between $\delta = -2$ and $\delta = 2$ is $\Delta\delta/k_0 \approx 4/31.42 \approx 0.13$, i.e., a wave number detuning of around 6% from k_0 in both directions still allows for unit transmission and zero accumulated phase.

send pulses through disorder as through a uniform system. We are confident that these exciting predictions can be implemented in a number of experiments where the spatial engineering of gain and loss has recently been achieved successfully [13, 23, 25, 26, 43, 61, 82–84].

A major obstacle to the practical implementation of the concept of CI-waves is the challenge of building continuous gain–loss distributions. Therefore, it is of interest to extend the notion of CI-waves to systems involving discrete distributions of gain and loss as theoretically shown in Ref. [28]. A corresponding experimental realization of this concept in an acoustic waveguide is presented in the next section.

2.3 Constant-pressure waves in acoustic waveguides[3]

In Ref. [28] we show analytically that the concept of CI-waves can also be applied to discrete systems. Here, we transfer this concept of discrete CI-waves to the acoustic regime where non-Hermitian acoustic wave physics has recently become a sizable research field on its own [82, 83, 85]. Switching from optics to acoustics, the corresponding quantities to the light intensity and the refractive index are the sound pressure and the acoustic impedance, respectively.

The experimental setup that we consider for the creation of constant-pressure sound waves is a one-dimensional air-filled tube loaded with a set of discrete acoustic inclusions modeled by acoustic impedances Z_j as can be seen Fig. 2.9. At low frequencies, where only a single mode can be excited, the system can be described by a transmission line model (see appendix A.3 and Ref. [86] for more details). In this model, the complex acoustic pressures p_j and volume flows q_j in front of each inclusion with $j = 1, ..., n$ (with n being the total number of inclusions) are connected through

$$\begin{pmatrix} p_j \\ q_j \end{pmatrix} = \begin{pmatrix} 1 & Z_j \\ 0 & 1 \end{pmatrix} \begin{pmatrix} A_j & B_j \\ C_j & D_j \end{pmatrix} \begin{pmatrix} p_{j+1} \\ q_{j+1} \end{pmatrix}, \qquad (2.12)$$

where $M_j = [A_j, B_j; C_j, D_j]$ represents the transfer matrices connecting the impedances Z_j and Z_{j+1} (for details see appendix A.3). In contrast to optics, the non-Hermiticity of the impedances Z_j is represented by a non-vanishing real part (positive for loss and negative for gain), whereas the imaginary part of Z_j corresponds to the Hermitian component. We assume that the finite system is connected to two semi-infinite half-spaces described by characteristic impedances Z_L (left) and Z_R (right).

In analogy to our CI-waves, we make the following (discretized) ansatz for our acoustic constant-pressure wave,

$$p_{j+1} = \exp\left(ik_0 \sum_{l=1}^{j} \phi_l \right) p_1, \qquad (2.13)$$

with ϕ_l being real-valued numbers representing the phase evolution of the sound wave (just as the generating function W). This wave ansatz forces the volume flow

---
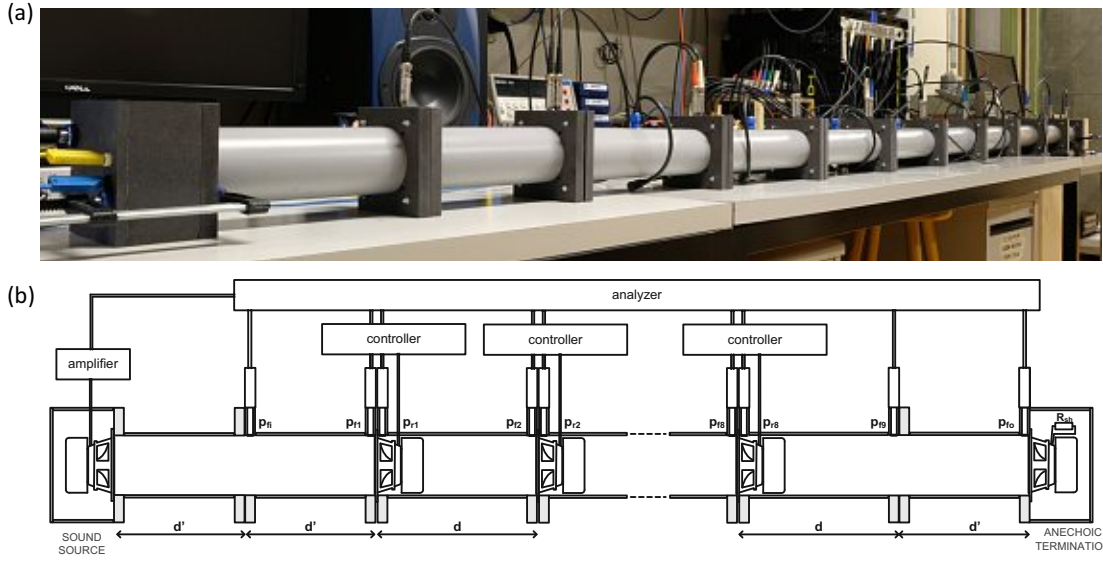
Fig 2.9: (a) Photo of the one-dimensional acoustic waveguide with a total length of $3.5\,\mathrm{m}$ loaded with eight non-Hermitian acoustic inclusions. These inclusions are loud-speakers, whose acoustic impedances can be designed through a harmonic impedance control method (for details see Methods section in Ref. [61]). (b) Schematic of the experimental setup with the sound source being at the left-hand side and the termination at the right-hand side.

q_j to take the values

$$q_j = \frac{1}{\prod_{l=1}^{j-1} D_l} q_1 - \sum_{l=1}^{j-1} \frac{C_l}{\prod_{m=l}^{j-1} D_m} p_{l+1}. \tag{2.14}$$

The required acoustic impedances Z_j supporting such a constant-pressure wave are found to be

$$Z_j = \frac{p_j - A_j p_{j+1} - B_j q_{j+1}}{C_j p_{j+1} + D_j q_{j+1}}. \tag{2.15}$$

If we set all the phases ϕ_j, then both the acoustic impedances Z_j and the reflection coefficient of the whole system R are fixed (see appendix A.3). Since we are interested in a perfectly transmitted wave featuring zero reflection, we want the reflection coefficient R to be zero. Therefore we have to relax two degrees of freedom in the choice of the phases ϕ_j which will be optimized to obtain zero reflection. Here, we use the first two phases ϕ_1 and ϕ_2 to tune the reflection coefficient R to zero without modifying the rest of the design. At this point we want to mention that also for the case of $R \neq 0$ we get a constant-pressure wave at each inclusion.

In order to illustrate the idea of discrete constant-pressure waves we first show a simulation of an acoustic system consisting of $n = 8$ inclusions terminated by

$Z_L = Z_R = Z_0$, where Z_0 is the characteristic acoustic impedance in the tube. We start by randomly choosing the phases ϕ_j, followed by an optimization of the first two phases to minimize R (as described above). These values ϕ_j are then used to calculate the corresponding acoustic impedances Z_j through Eq. (2.15). In a next step we study the behavior of the wave in the Hermitian system, i.e., when the acoustic impedances are purely imaginary [see Fig. 2.10(a)]. The pressures p_j for this Hermitian system can be determined through Eq. (2.12) and show large variations as shown in Fig. 2.10(c). Adding, however, the corresponding gain and loss components to the system [see Fig. 2.10(b)] force the wave to have a constant pressure at each site as shown in Fig. 2.10(d).
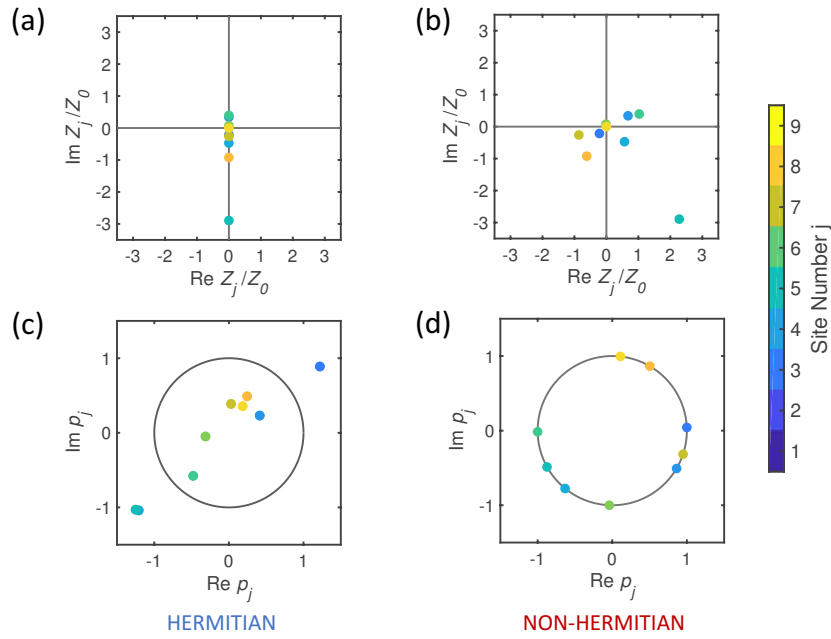
Fig 2.10: (a) Acoustic impedances Z_j calculated from Eq. (2.15) in the complex plane where the real part of all impedances are removed to obtain a Hermitian system. (c) Acoustic pressures p_j obtained for the case in (a) leading to non-uniform amplitudes. (b) By adding loss and gain, we obtain a non-Hermitian system whose non-Hermitian impedances have the same imaginary parts as those in the case of the Hermitian system in (b), but their real parts are now different from zero. (d) The non-Hermitian additions result in an acoustic scattering state with constant pressure at each site p_j.

In order to get a better understanding of our constant-pressure waves, we study now the full wave field inside the waveguide by simulating a three-dimensional air-filled cylindrical pipe loaded with the same acoustic impedances as in Fig. 2.10. This gives us access to the pressures not only at the inclusions p_j but everywhere in the system. In Fig. 2.11(a) we can see the real part of the acoustic pressure (at a given time) in black when there is no gain and loss inside the system for injection

from the left-hand side into the pipe. The gray area represents the values spanned by the pressure over a full period of the harmonic field. Due to the disorder inside the system, large parts of the wave are reflected and the absolute value of the pressure decreases along the system. If we now, in turn, add the corresponding non-Hermitian parts to the impedances as dictated by Eq. (2.15), we can see in Fig. 2.11(b) that the wave gets perfectly transmitted through the system. Additionally, we can see that the gray envelope meets the dashed red line at unity right in front of every inclusion corresponding to the location of every pressure site p_j. In contrast to continuous constant-pressure waves, the discrete design here forces the pressure to be unitary in front of each inclusion, but not in between. That is, however, not a limitation of the concept, since the distance between neighboring sites p_j can be chosen to be arbitrarily small and, when being shorter than the wavelength, prevents large-amplitude fluctuations in between the sites. Additionally, perfect transmission is guaranteed by design such that we can conclude that the present discretization of the constant-pressure property does not introduce any fundamental limitation compared to the continuous case, although it brings a significant simplification on the required gain-loss distribution.
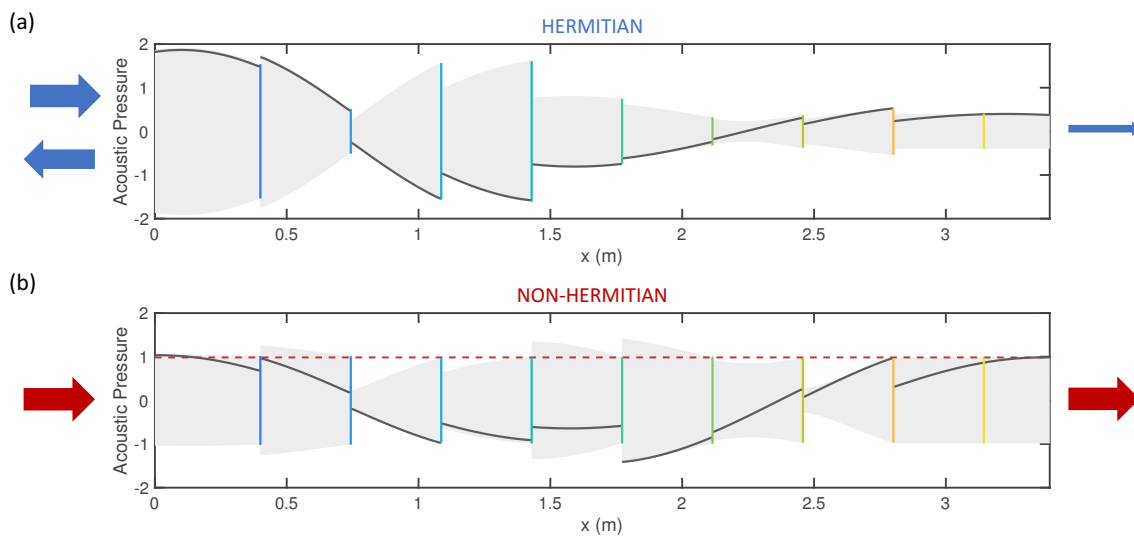
Fig 2.11: (a) Full wave three-dimensional finite-element simulations of the pressure field in the Hermitian case of Fig. 2.10(a),(c). The system transmits poorly and the pressure inside fluctuates strongly. (b) Simulation of the corresponding non-Hermitian case of Fig. 2.10(b),(d). The amplitude of the pressure reaches unity at each check point p_j, located directly in front of each inclusion [consistent with Fig. 2.10(d)] making the disorder transparent. The black line is a snapshot in time of the acoustic pressure field, whereas the gray area shows the range of its oscillations as time evolves. The vertical colored lines represent the locations of the impedances Z_j.

Based on our theory and simulations, we show now the results of the experiment, where a schematic of this experiment can be seen in Fig. 2.12(a). We first consider again the Hermitian system having only imaginary acoustic impedances [see Fig. 2.12(b)]. Statistical considerations show that such a system operates in the regime of Anderson localization where the waveguide is about three times the localization length (see Methods section in Ref. [61] for details). The acoustic pressures inside the Hermitian system measured directly in front of the inclusions with the help of microphones are displayed in 2.12(c). We can clearly see that the wave state has a spatially varying pressure and a strongly reduced transmission to the right-hand side. Adding the correct gain and loss to the inclusions [see Fig. 2.12(d)], the measured pressure amplitudes become identical at each site as shown in Fig. 2.12(e). Our measurements clearly demonstrate that a specific distribution of gain and loss can even make a disordered and Anderson localized Hermitian system transparent for waves coming from the left-hand side featuring a constant pressure at discrete check points.
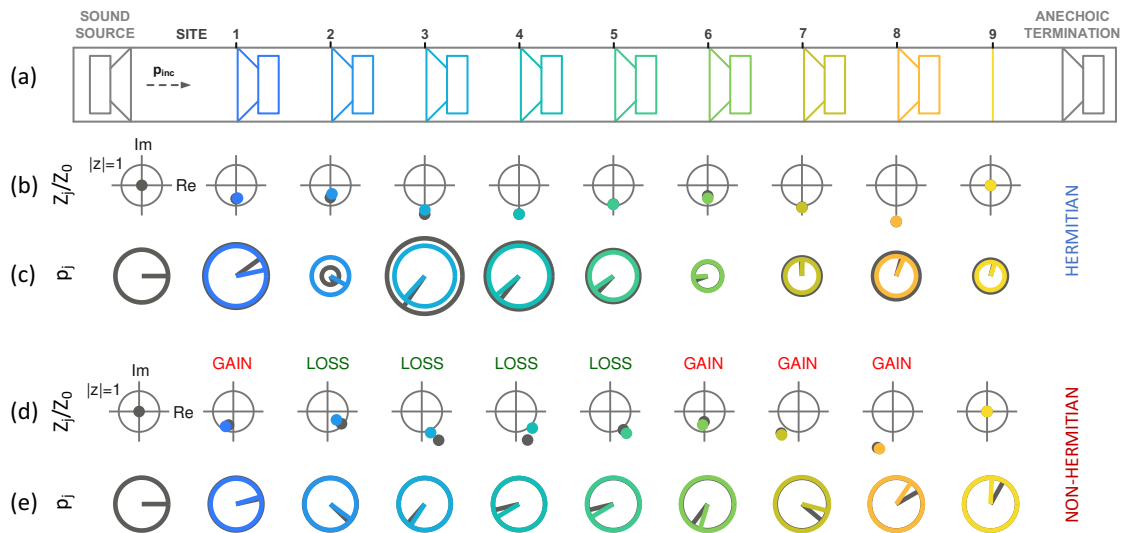
Fig 2.12: (a) Schematic of the setup shown in Fig. 2.9. (b) Imaginary part (Hermitian case) of the constant-pressure impedances represented in the complex plane forming a disorder. (c) Pressures measured at each site for the Hermitian case in (b) showing high variations due to the disorder. The pressures are represented as phasors, with the radius of the circle being proportional to their amplitude, and the line segment showing their phase with respect to that of the incident pressure. (d) Impedances obtained by adding the correct gain or loss value to each inclusion. (e) Pressures measured at each site in the non-Hermitian case (d) demonstrating the discrete constant-pressure property in excellent agreement with theoretical predictions. Measured data is represented by colors and simulated data in black.

Summarizing the previous sections, we show that we can completely counteract the detrimental influence of disorder by adding to it a well-defined gain and loss distribution to finally obtain a wave with no intensity (or pressure) variations that gets perfectly transmitted through the system. This concept was demonstrated in the acoustic experiment shown in this section. One essential point to create such constant-intensity (constant-pressure) waves is the choice of the generating function $W(x)$ or the phases ϕ_j to be real quantities. In the next section we show that by allowing for complex generating functions $W(x)$ or phases ϕ_j we can, in fact, obtain scattering states with any predetermined intensity (pressure) distribution such that a constant-intensity (constant-pressure) wave can be seen as a special case of this much broader class of wave states.

2.4 Predetermined-intensity waves

The call for a CI-wave restricts the generating function $W(x)$ to be real-valued, however, the ansatz $\psi(x) = A \exp\left[ik_0 \int_{-L}^{x} W(x')dx'\right]$ also solves the Helmholtz Eq. (2.1) when the generating function $W(x)$ is complex, i.e., $W(x) = W_R(x) + iW_I(x)$, with $W_R(x)$ and $W_I(x)$ being the real and imaginary part, respectively. One can easily see that a complex generating function results in a wave with varying intensity profile $|\psi(x)|^2 = |A|^2 \exp\left[-2k_0 \int_{-L}^{x} W_I(x')dx'\right]$ which is completely determined by the imaginary part of the generating function $W_I(x)$. Thus, properly choosing $W_I(x)$ allows us to design the intensity distribution of a scattering state as required. The CI-wave in Eq. (2.2) is then just a special solution of these generalized wave states where the imaginary part $W_I(x)$ is zero. In order to still satisfy the perfect transmission boundary conditions in Eq. (2.7), the imaginary part $W_I(x)$ has to vanish at the boundaries of the scattering region, i.e., $W_I(-L) = 0 = W_I(L)$.

In order to illustrate this new concept, we jump right to one example. Of practical interest in wave engineering is to create a sharp intensity peak, i.e., a focus at a desired position. We want to emphasize, however, that our concept is not restricted to this specific intensity profile – it can follow any intensity profile. We choose the imaginary part of the generating function to be the derivative of a Gaussian function $G(x) = a \exp(-x^2/\sigma^2)$ with a certain amplitude a and a certain width σ, i.e., $W_I(x) = \partial G(x)/\partial x$, since this function follows the required boundary conditions already per construction (assuming that σ is small enough such that the derivative of the Gaussian is negligible at the boundaries $x = \pm L$). Even though it is not obvious, this specific choice of $W_I(x)$ leads to a strongly peaked intensity $|\psi(x)|^2 = |A|^2 \exp\left[-2k_0 a \exp(-x^2/\sigma^2)\right]$, as shown later. The real part of the generating function $W_R(x)$ does not affect the intensity of the wave state, but it does affect the refractive index. To make the formation of the intensity peak more spectacular, we choose $W_R(x)$ to be a randomly fluctuating function formed by

a superposition of Gaussian functions with random widths and random positions resulting in a disordered real part of the refractive index $n_R(x)$. The complex refractive index that supports the desired wave state, i.e., the focus, can be calculated by

$$n^2(x) = [W_R(x) + \mathrm{i}W_I(x)]^2 - \frac{\mathrm{i}}{k_0}\frac{\partial}{\partial x}[W_R(x) + \mathrm{i}W_I(x)], \qquad (2.16)$$

i.e., in analogy to Eq. (2.3) but now with a complex (instead of a purely real) generating function $W(x)$. In Fig. 2.13(a) we can see the real part of the refractive index calculated from Eq. (2.16) with the corresponding intensity of a wave injected from the left-hand side. The disorder, which originates from the disordered function $W_R(x)$ leads to high variations in the intensity pattern. Figure 2.13(b) shows that by adding the correct gain and loss distribution to the system shown in Fig. 2.13(a), we can create a well-defined intensity peak at the predetermined position and additionally make the wave lose all its intensity variations despite the fact that the system is still disordered.
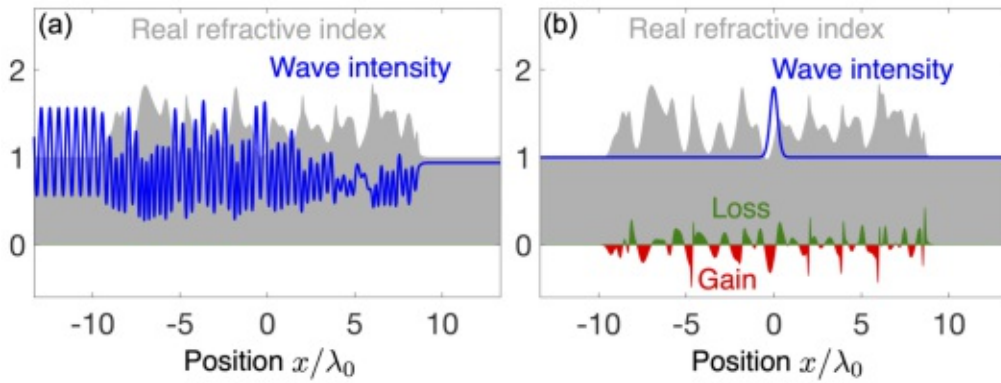
Fig 2.13: (a) Strongly fluctuating intensity of a wave (blue) with wavelength $\lambda_0 = 0.15$ impinging from the left onto a disordered refractive index distribution that is obtained from the real part of $n(x)$ calculated with Eq. (2.16). The real part of the generating function $W_R(x)$ is a superposition of randomly placed Gaussian functions with the same amplitude of 0.2 but with random widths (uniformly distributed between 0.005 and 0.055). The imaginary part $W_I(x)$ is given by $W_I(x) = \partial/\partial x [a\exp(-x^2/\sigma^2)]$ with $a = 0.007$ and $\sigma = 0.05$. (b) The wave shows a strong intensity build-up at the predetermined position $x = 0$ and gets perfectly transmitted when the correct gain and loss [imaginary part of $n(x)$ from Eq. (2.16)] is added to the disorder.

Having demonstrated that a generalization of the concept of CI-waves to a much broader class of waves can lead to waves with a predetermined intensity profile, we show in the next section how to transfer this generalization also to the transmission line model which is discussed in the previous section.

2.5 Predetermined-pressure waves in acoustic waveguides[4]

The idea of this section is to transfer the concept of waves with a predetermined intensity profile also to the transmission line model for acoustic waves introduced in section 2.3. The motivation behind this effort is to study two interesting acoustic devices. The first one will be a structure allowing for a so-called "quiet zone", i.e., a region inside a structure with a negligibly small sound amplitude. The second device we study is a structure that perfectly absorbs sound waves when put, e.g., on a wall, to minimize sound emission from this room.

In analogy to the complex generating function $W(x)$ in the last section, we now also extend the phases of the wave ansatz in Eq. (2.13) to complex numbers ϕ_j, i.e., $\phi_j = \phi_{R_j} + i\phi_{I_j}$, giving us

$$p_{j+1} = \exp\left(-k_0 \sum_{l=1}^{j} \phi_{I_l}\right) \exp\left(ik_0 \sum_{l=1}^{j} \phi_{R_l}\right) p_1. \qquad (2.17)$$

We can see that the first term including the imaginary parts of the phases ϕ_{I_j} determines the amplitude profile A_j of the wave

$$A_j = |p_j| = \exp\left(-k_0 \sum_{l=1}^{j-1} \phi_{I_l}\right) |p_1|, \qquad (2.18)$$

whereas the second term determines the phase evolution of the wave. Our aim is to choose the phases ϕ_j in such a way that we get a predetermined amplitude distribution A_j. This can be done by solving Eq. (2.18) for ϕ_{I_j},

$$\phi_{I_j} = -\frac{1}{k_0}\left[\ln\left(\frac{A_{j+1}}{|p_1|}\right) - \ln\left(\frac{A_j}{|p_1|}\right)\right], \qquad (2.19)$$

i.e., given the amplitude profile A_j one can easily calculate the required imaginary parts of the phases ϕ_{I_j} with Eq. (2.19). The imaginary parts of the phases ϕ_{I_j} have to fulfill the boundary conditions $\phi_{I_0} = \phi_{I_n} = 0$. The corresponding acoustic impedances supporting this pressure wave can be calculated in the same way as for the constant-pressure wave described in Section 2.3 through Eq. (2.15).

In order to verify our theoretical concept, we perform numerical simulations. Our first choice is to minimize the pressure of a sound wave in a predetermined region of the medium, i.e., we want to realize a so-called "quiet zone". For this purpose we use a pressure profile A_j which is constant everywhere except at three chosen positions

---

[4] The results presented in this section were obtained together with Nikolaus de Zordo and Lukas Leczek whose student projects I co-supervised [62, 63].

where the amplitude is small (here $A_6 = A_7 = A_8 = 0.1$, $A_j = 1$ everywhere else). With the choice of the amplitude profile A_j, the imaginary parts of the phases ϕ_I are fixed by Eq. (2.19). Since the amplitude is only affected by the imaginary parts of ϕ, i.e., ϕ_I, we can choose arbitrary real parts of the phases ϕ_R which we choose to be constant, except for the first two phases which are optimized in such a way, that the reflection coefficient R gets minimal (in analogy to the constant-pressure waves in Section 2.3). With the choice of the phases ϕ_j we know all pressures p_j as a function of p_1 or R, respectively. With Eq. (2.15) we are able to calculate our acoustic impedances Z_j that support our pressure wave with the chosen amplitude profile, see Fig. 2.14. As shown in Fig. 2.14(b), the scattering state (blue) shows the predicted amplitude profile, i.e., the "quiet zone" with a small pressure at scatterer positions 6 to 8. The real and the imaginary parts of the acoustic impedances Z_j that lead to this amplitude profile are shown in red/green and gray, respectively. If we, however, remove the gain and loss from the system, i.e., if we neglect the real part of the impedances Z_j as can be seen in Fig. 2.14(a), we get fluctuations in our amplitude profile (blue) due to reflections.

Fig 2.14: (a) Pressure p_j of a sound wave injected from the left-hand side into a system consisting only of imaginary impedances Z_j (gray), i.e., a Hermitian system. (b) Adding the correct gain (red) and loss (green) distribution (i.e., real parts of the impedances Z_j) to the system, the pressure wave p_j follows the predicted amplitude profile $A_j = |p_j|$ showing a so-called "quiet zone", i.e., an extended region of small sound pressure (here located at sites 6-8).

After demonstrating that this idea of generating waves with a predetermined pressure profile works also for the transmission line model, we show now that we can use this concept to build an absorber for sound waves. Together with Manfred Kaltenbacher and his PhD-student Sebastian Floss from TU Wien we were working on a proof-of-principle experiment showing that waves entering an acoustic waveguide get absorbed strongly enough to prevent waves from being transmitted through the waveguide and from being back-reflected from it. In order to achieve

this goal we can directly apply the idea of a predetermined-pressure wave by demanding an exponentially decreasing pressure distribution inside the waveguide. The restriction that we impose on ourselves is to make the waveguide as short as possible and to use lossy elements only, in contrast to the experiment in Section 2.3 where we used both, gain and loss. The lossy elements can be realized by micro perforated plates (MPPs) which are thin flat plates with small holes punched in it, where the acoustic impedance of the plate Z can be tuned by varying the number of holes [87]. The goal is to design a waveguide with a certain number n of MPPs characterized by their impedances Z_j such that waves entering the waveguide from one side get absorbed as much as possible with no waves being back-reflected. The task now is to tune the parameters n, the distance d between the MPPs, the desired amplitude profile A_j and the real part of the phases ϕ_{R_j} in such a way that the required impedances Z_j only have a positive real part, i.e., only loss. Using a simple gradient descent optimization routine, we found a system as shown in Fig. 2.15(b), where the pressure at the last plate is only around 19% of the incident pressure and the reflection coefficient only $R \approx 10^{-4}$; in other words, almost nothing gets back-reflected and only 19% get transmitted. Removing the loss from the system as shown in Fig. 2.15(a), we get a reflection coefficient of $R \approx 0.99$ and a pressure at the output of the waveguide of about 39% of the incident pressure. The waveguide is optimized for a wavelength of $\lambda_0 = 1.5\,\mathrm{m}$ for which conventional absorbers would be much larger. The next steps of this project are to perform full-wave simulations and, finally, build the acoustic waveguide. We hope that our concept can help to create new types of absorbers that can be used, e.g., in anechoic chambers. In such chambers, conventional absorbing materials such as foam are placed on the inside of the room to avoid back-reflections from the walls. These absorbing materials efficiently absorb sound waves above $100\,\mathrm{Hz}$ and have a typical length of $1.5\,\mathrm{m}$. Our concept has the potential to yield absorbers that are considerably smaller than conventional absorbers and to efficiently absorb sound waves with frequencies lower than $100\,\mathrm{Hz}$.

In the previous sections we study many aspects of constant-intensity (pressure) waves and waves with predetermined intensity (pressure) profile in one-dimensional or quasi one-dimensional systems. A natural question that arises now is if such waves also exist in more than one dimension. Surprisingly, such constant-intensity waves also exist in two-dimensions which we show in the next section.
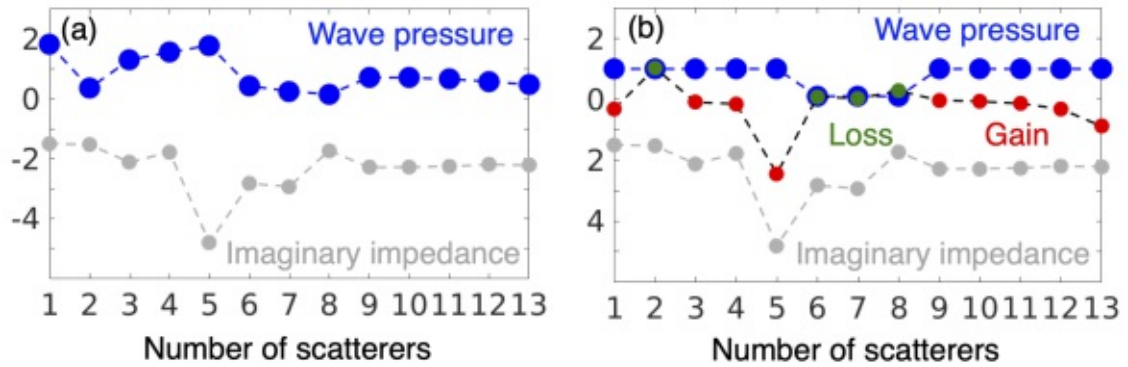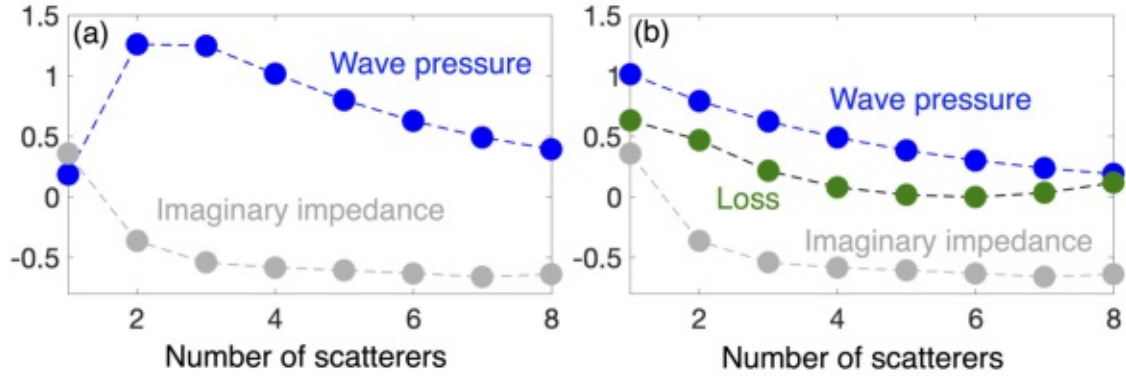
Fig 2.15: (a) Pressure p_j of a sound wave injected from the left-hand side into a system consisting only of imaginary impedances Z_j (gray), i.e., a Hermitian system. (b) Adding the correct loss (green) distribution (i.e., real parts of the impedances Z_j) to the system, the pressure wave p_j follows the predicted uniformly damped amplitude profile $A_j = |p_j| = \exp(-\gamma x_j)$, where $\gamma \approx 2.65$ is the absorption rate and x_j the positions of the MPPs. The pressure at the last MPP has an amplitude of only 19% of the incident pressure, i.e., the absorption is quite efficient, and the reflection coefficient is only $R \approx 10^{-4}$. In the Hermitian system shown in (a) the reflection coefficient is $R \approx 0.99$ and the pressure at the last MPP around 39% of the incident pressure. The system consists of $n = 8$ MPPs being separated by a distance $d = 9.35\,\mathrm{cm}$, and having a thickness of $2\,\mathrm{mm}$ i.e., the system has a total length of $L \approx 86\,\mathrm{cm}$.

2.6 Constant-intensity waves in two-dimensional structures[5]

While most of the previous works on CI-waves focused on one-dimensional scattering systems [27, 28, 30, 61], a recent work showed how to generalize this concept also to non-paraxial scattering problems with two spatial dimensions [88]. While the work in Ref. [88] focuses on epsilon-near-zero (ENZ) materials, we study now two-dimensional CI-waves in structures with $\varepsilon(x, y) = n^2(x, y) \geq 1$.

We start our analysis by considering the two-dimensional Helmholtz equation that describes the scattering of a linearly polarized wave $\psi(x, y)$ in the x-y plane (for details see appendix A.1):

$$\left[\frac{\partial^2}{\partial x^2} + \frac{\partial^2}{\partial y^2} + k_0^2 n^2(x, y) \right] \psi(x, y) = 0. \tag{2.20}$$

The scattering region $[-L_x, L_x] \times [-L_y, L_y]$ is defined as the region in space where

---

[5] This work was carried out together with my colleague Ivor Krešić who performed the numerical simulations and Konstantinos Makris who derived most of the analytical results [64]. I was involved in the development of the theory and generated the figures for our joint publication [64].

the complex refractive index $n(x, y) = n_R(x, y) + \mathrm{i}n_I(x, y)$ is different from the asymptotic refractive index n_0. The question we are interested in is if it is possible to find CI-waves in two-dimensional dielectric structures with gain and loss. In other words, we are looking for solutions of the constant-intensity form:

$$\psi(x, y) = e^{\mathrm{i}k_0\theta(x,y)}, \tag{2.21}$$

where $\theta(x, y)$ plays the role of the generating function here. In order to obtain CI-solutions for a given function $\theta(x, y)$, the corresponding refractive index is non-Hermitian and of the form:

$$n^2(x, y) = \left(\frac{\partial}{\partial x}\theta\right)^2 + \left(\frac{\partial}{\partial y}\theta\right)^2 - \frac{\mathrm{i}}{k_0}\left[\left(\frac{\partial^2}{\partial x^2}\theta\right) + \left(\frac{\partial^2}{\partial y^2}\theta\right)\right], \tag{2.22}$$

where we skipped all arguments for better readability. In a next step, we have to find boundary conditions for the generating function $\theta(x, y)$. We assume that outside the scattering region the wave is a simple right-propagating plane wave with wave vector parallel to the x-axis, i.e., $\psi^{\mathrm{out}}(x, y) = \exp(\mathrm{i}k_0 n_0 x)$, such that we impose continuity conditions along the boundaries. In other words, we have the following boundary conditions for the electrical field and its derivative:

$$\psi^{\mathrm{out}}(\pm L_x, y) = \psi(\pm L_x, y), \tag{2.23}$$

$$\frac{\partial\psi^{\mathrm{out}}}{\partial x}(\pm L_x, y) = \frac{\partial\psi}{\partial x}(\pm L_x, y), \tag{2.24}$$

$$\psi^{\mathrm{out}}(x, \pm L_y) = \psi(x, \pm L_y), \tag{2.25}$$

$$\frac{\partial\psi^{\mathrm{out}}}{\partial y}(x, \pm L_y) = \frac{\partial\psi}{\partial y}(x, \pm L_y). \tag{2.26}$$

By direct substitution of the CI-wave in Eq. (2.21) into these boundary conditions, we can rewrite them in terms of $\theta(x, y)$:

$$\pm L_x n_0 = \theta(\pm L_x, y), \tag{2.27}$$

$$n_0 = \frac{\partial\theta}{\partial x}(\pm L_x, y), \tag{2.28}$$

$$n_0 x = \theta(x, \pm L_y), \tag{2.29}$$

$$0 = \frac{\partial\theta}{\partial y}(x, \pm L_y). \tag{2.30}$$

Also here we directly jump to one specific CI-refractive index and demonstrate the CI-wave it gives rise to. One generating function $\theta(x, y)$ satisfying these boundary conditions is

$$\theta(x, y) = n_0 x + a \exp\left(-\frac{x^2}{2\sigma^2} - \frac{y^2}{2\sigma^2}\right), \tag{2.31}$$

provided that σ is small enough such that the Gaussian term can be neglected at the boundaries of the scattering region. This generating function yields the following CI-refractive index [via Eq. (2.22)]:

$$n^2(x) = \left[n_0 - \frac{a}{\sigma^2} x \exp\left(-\frac{x^2}{2\sigma^2} - \frac{y^2}{2\sigma^2} \right) \right]^2 + \left[\frac{a}{\sigma^2} y \exp\left(-\frac{x^2}{2\sigma^2} - \frac{y^2}{2\sigma^2} \right) \right]^2$$
$$- \frac{\mathrm{i}}{k_0} \frac{a}{\sigma^4} (x^2 + y^2 - 2\sigma^2) \exp\left(-\frac{x^2}{2\sigma^2} - \frac{y^2}{2\sigma^2} \right). \tag{2.32}$$

The real part of this refractive index distribution can be seen in Fig. 2.16(a) and its imaginary part in Fig. 2.16(b). Since experimentally it is not possible to inject an infinitely extended plane wave onto a structure, we have to truncate the incident wave at a certain width. Numerically, we can achieve this by injecting a beam with a super-Gaussian transverse profile wider than the scattering region. In Fig. 2.16(c) we see how such a truncated wave hits the Hermitian structure with a refractive index as shown in Fig. 2.16(a). We can see that the wave strongly scatters at the inhomogeneity resulting in a high intensity peak. If we now add the gain-loss distribution [see Fig. 2.16(b)] to the system and inject the same beam again, we can see in Fig. 2.16(d) that the wave propagates through the system as if there were no inhomogeneities at all proving that the CI-concept works for two-dimensional structures as well.

After studying such a simple system serving as a proof-of-concept, we jump now to a more complex system, which will be a disordered one. We choose $\theta(x,y)$ to be a superposition of $N = 300$ Gaussian functions with random amplitudes a_n, random widths σ_n and random positions (x_n, y_n), i.e.,

$$\theta(x,y) = \sum_{n=1}^{N} a_n \exp\left[-\frac{(x-x_n)^2}{2\sigma_n^2} - \frac{(y-y_n)^2}{2\sigma_n^2} \right]. \tag{2.33}$$

The real and imaginary parts of the corresponding CI-refractive index can be seen in Figs. 2.17(a) and (b). Again, we first shine a wave onto the Hermitian system leading to a highly complex intensity pattern [see Fig. 2.17(c)]. The wave can be engineered to lose all its intensity variations and back-reflections by adding the correct gain-loss distribution to it, thus creating a CI-wave, see Fig. 2.17(d). This clearly demonstrates that even two-dimensional strongly scattering structures can be made perfectly transmitting by engineering its gain-loss distribution.

In a next step we study the sensitivity of the designed CI-system with respect to changes of the input angle φ and to the incident wave number k (at normal incidence). The robustness is measured by the L^2-error as follows:

$$d(I, I^{\varphi/k}) = \frac{\sqrt{\int_{-L_x}^{L_x} \int_{-L_y}^{L_y} [I(x,y) - I^{\varphi/k}(x,y)]^2 dxdy}}{\sqrt{\int_{-L_x}^{L_x} \int_{-L_y}^{L_y} [I^{\varphi/k}(x,y)]^2 dxdy}}, \tag{2.34}$$
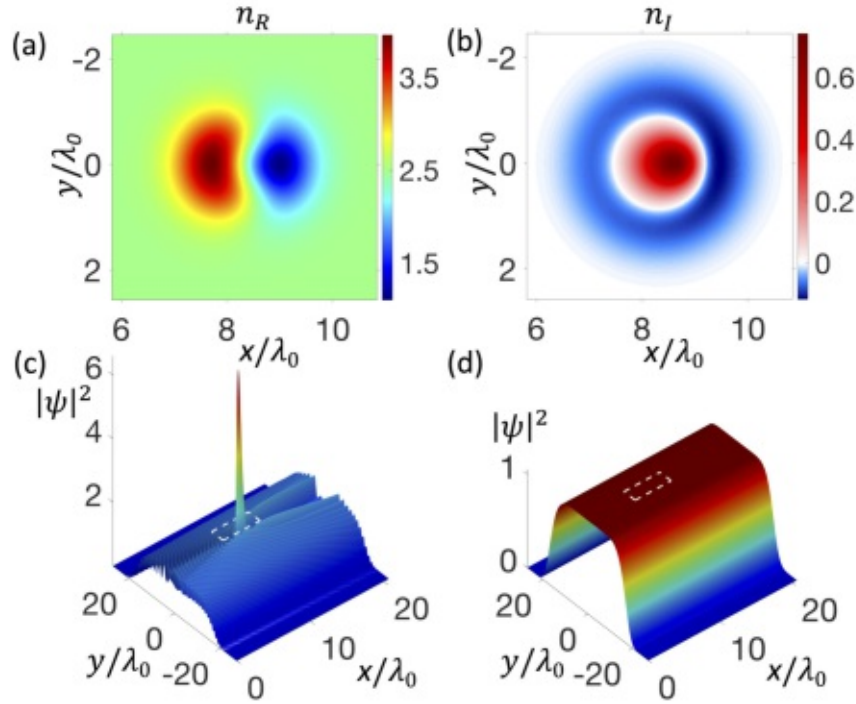
Fig 2.16: (a) Real and (b) imaginary part of the CI-refractive index in Eq. (2.32) with $n_0 = 2.5$, $\sigma = 0.2$ and $a = 0.48$. (c) A plane wave illumination is mimicked by a wave with a super-Gaussian transverse profile much larger than the width of the scattering region (dashed white box). The wave scatters at the refractive index in (a), whereas the wave gets perfectly transmitted featuring a constant intensity when the correct gain and loss distribution from (b) is added, see (d). Here, we solve the Helmholtz Eq. (2.20) numerically using an advanced finite-element method (NGSolve Finite Element Library, https://ngsolve.org/).

where $I(x, y)$ is the intensity distribution of the CI-wave inside the region marked with white dashed lines in Fig. 2.17(d) and $I^{\varphi,k}(x, y)$ is the intensity distribution of the wave with changed incidence angle φ, I^{φ}, or with different wave number k, I^k. We compute the L^2-errors for angle and wave number detuning for both a CI-system designed for wave number k_0 and normal incidence ($\varphi = 0$) and for the corresponding Hermitian system without gain and loss. In Fig. 2.17(e) we show the L^2-error scan of the angle φ, where we can see that near normal incidence, the CI-wave prescription works well to produce a beam without intensity modulations (see blue line), as compared to the Hermitian case (red line) showing a relatively large error for all angles. At angles larger than $5°$, the non-Hermitian solution starts having similar distances to the perfect CI-wave as the Hermitian solution. The wave number scan [see Fig. 2.17(f)] shows a relatively high degree of robustness. The scan yields relatively small L^2-errors for deviations below 10% from the design
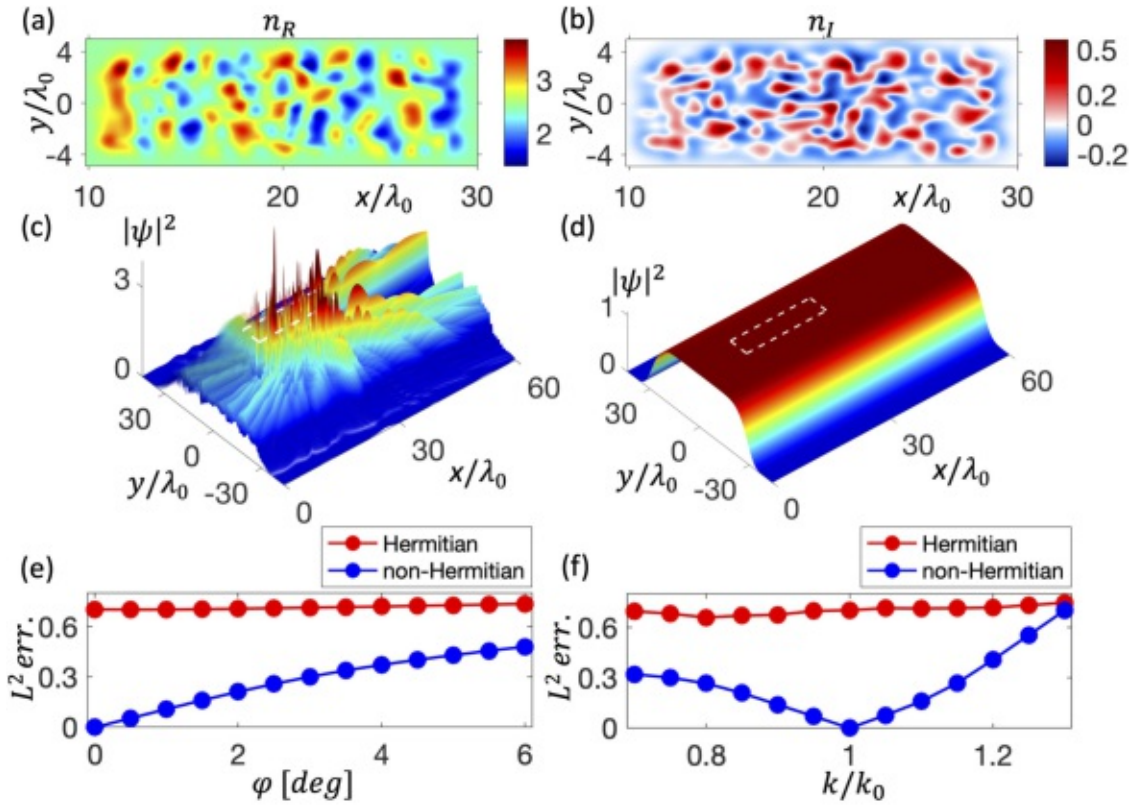
Fig 2.17: (a) Real and (b) imaginary part of a disordered refractive index calculated with Eq. (2.22) with a generating function shown in Eq. (2.33). (c) A super-Gaussian beam injected into the system shown in (a) leads to a highly oscillatory wave function that can be made completely flat [see (d)] by adding the correct gain-loss distribution shown in (b). (e) L^2-error [see definition in Eq. (2.34)] of the intensity distribution of the wave in the region marked with white dashed lines in (c) and (d) between the perfect CI-wave shown in (d) and beams with different incidence angles φ for both the CI-system (blue line) and the corresponding Hermitian system (red line). (f) Same quantities as in (e) but for a scan of the incident wave number k at normal incidence $\varphi = 0$.

wave number k_0 which is a remarkably broad frequency window. This reflects exactly the general frequency stability of CI-waves that we showed already for the one-dimensional case, see e.g., Fig. 2.2.

Summarizing, we demonstrate here that engineering the complex refractive index of a medium one can fully eliminate multiple scattering even in two dimensions. Specifically, we show how to construct a refractive index distribution that – for a particular wavelength – leads to CI-waves inside disordered media.

Having shown in this chapter that adding gain and loss can be used to overcome multiple scattering induced by disordered structures, we follow in the next chapters

quite the opposite approach. Instead of controlling the medium itself (by adding gain and loss), we now focus instead on controlling the incident wavefront to achieve a desired intensity distribution of the wave inside the scattering region. In order to find out how the incident wavefront has to be shaped to produce a certain wave state, we make use of the Wigner-Smith time-delay operator which we introduce at the beginning of the next chapter.

Chapter 3

Time-delay operator and particle-like states

The concept of time-delay in scattering theory was first introduced in the thesis of Eugene Wigner's PhD-student Leonard Eisenbud for nuclear scattering problems [89]. What Eisenbud and Wigner discovered was that the duration of a scattering process can be extracted from the energy derivative of the scattering phase [90]. Later, Felix Smith generalized this concept to a multi-channel scattering problem [91] by introducing the so-called Wigner-Smith (or Eisenbud-Wigner-Smith) time-delay operator, that includes the system's multi-channel scattering matrix S (see Chapter 1 for details on the scattering matrix) by way of a frequency derivative,

$$Q_\omega = -\mathrm{i}S^{-1}\frac{\partial S}{\partial \omega}. \qquad (3.1)$$

In case of a unitary scattering matrix (i.e., in the absence of gain and loss), this operator is Hermitian and its eigenstates $\vec{u}^{(i)}$ form an orthogonal basis, where the index i represents the i-th eigenvector. (For reasons of better readability, we skip the index i for the derivations below.) The real-valued eigenvalues τ_ω of Q_ω, also called proper delay times, can be interpreted as the time-delay the wave accumulates by traversing the scattering region. To be more precise, the eigenvalues τ_ω are given by $\tau_\omega = \partial\phi/\partial\omega$, where ϕ is the global phase of the outgoing wave $\vec{v} = S\vec{u}$, i.e., $\vec{v} = |\vec{v}|\hat{v}e^{\mathrm{i}\phi}$, with $\hat{v}$ being the unit vector of $\vec{v}$ (see Chapter 1 for details on the scattering formalism). Physically speaking, the eigenvalues τ_ω are given by the frequency derivative of the global scattering phase ϕ and are therefore proportional to the time-delay [89]. It is worth mentioning that the Wigner-Smith time-delay operator features interesting connections to the system's density of states [92–95] and, as shown recently, can also be used to maximize the energy stored in resonators [96].

Probably unaware of the works by Wigner and Smith, Fan and Kahn showed much later in multi-mode fibers that there are certain modes (so-called principal modes), whose output speckle patterns (i.e., the wavefront at the fiber exit) are to first order independent with respect to a frequency change of the incident wave at the input of the fiber (apart from a global change of the brightness) [97]. We show

now in a short derivation that these robust modes are nothing else than eigenstates of the Wigner-Smith time-delay operator: the input and output waves of a fiber [similar to Fig. 1.1(c)] are described by two coefficient vectors $\vec{u}_l$ and $\vec{v}_r$ in a certain basis, respectively. They are related to each other by the transmission matrix t, i.e., $\vec{v}_r = t\vec{u}_l$. In general, the output vector $\vec{v}_r$ is frequency dependent [due to the frequency dependence of the transmission matrix $t(\omega)$] and can thus be expanded around ω_0,

$$\vec{v}_r(\omega_0 + \Delta\omega) = \vec{v}_r(\omega_0) + \Delta\omega \frac{\partial\vec{v}_r}{\partial\omega}\Big|_{\omega_0} + \dots$$
$$= t(\omega_0)\vec{u}_l + \Delta\omega\frac{\partial t(\omega)}{\partial\omega}\Big|_{\omega_0}\vec{u}_l + \dots, \tag{3.2}$$

where $\Delta\omega$ is a small change of the frequency ω_0 and we keep the input vector $\vec{u}_l$ fixed for all ω. Since the output speckle patterns of principal modes are robust with respect to changes of ω, we demand now that the first order term in Eq. (3.2) is parallel to the zeroth order term, i.e, they should only differ by a (complex) constant z,

$$t(\omega_0)\vec{u}_l = z\Delta\omega\frac{\partial t(\omega)}{\partial\omega}\Big|_{\omega_0}\vec{u}_l. \tag{3.3}$$

We now multiply both sides of Eq. (3.3) with $(it)^{-1}$ and rewrite it as an eigenvalue equation,

$$\frac{1}{iz\Delta\omega}\vec{u}_l = -it^{-1}\frac{\partial t(\omega)}{\partial\omega}\Big|_{\omega_0}\vec{u}_l = \tau_\omega\vec{u}_l = q_\omega\vec{u}_l \tag{3.4}$$

with

$$q_\omega := -it^{-1}\frac{\partial t(\omega)}{\partial\omega} \tag{3.5}$$

being the operator with eigenvalues $\tau_\omega := (iz\Delta\omega)^{-1}$ and eigenvector $\vec{u}_l$. The robustness with respect to changes of the frequency of the speckle pattern $\vec{v}_r = t\vec{u}_l$ of this eigenvector $\vec{u}_l$ is mathematically expressed as

$$\vec{v}_r(\omega_0 + \Delta\omega) \approx \exp(i\tau_\omega\Delta\omega)\vec{v}_r(\omega_0), \tag{3.6}$$

i.e., there is only a global change of the output speckle described by the factor $\exp(i\tau_\omega\Delta\omega)$ including the eigenvalue τ_ω.

Considering now that for perfect multi-mode fibers there are no reflections and no losses, the transmission matrix t is unitary – just as the entire scattering matrix S. The operators Q_ω from Eq. (3.1) and q_ω from Eq. (3.5) are thus the same thing, such that the principal modes are nothing else but the eigenstates of the Wigner-Smith time-delay operator [57, 58]. If the transmission matrix t is not unitary, differences start to arise between eigenstates of Q_ω and q_ω. Whereas for the non-Hermitian operator q_ω only the transmitted wave $\vec{v}_r$ of its eigenstates are insensitive (up to a global factor) with respect to a change of the input frequency ω

[see Eq. (3.6)], eigenstates of the Hermitian operator Q_ω yield output profiles that are insensitive not only in their transmitted part $\vec{v}_r$ but also in their reflected part $\vec{v}_l$. Mathematically, this translates into

$$\vec{v}(\omega_0 + \Delta\omega) \approx \exp(\mathrm{i}\tau_\omega \Delta\omega)\vec{v}(\omega_0), \tag{3.7}$$

with $\vec{v} = (\vec{v}_l, \vec{v}_r)^T = S\vec{u}$ and $\vec{u}$ being an eigenstate of Q_ω. Contrary to eigenvalues of the Hermitian operator Q_ω, eigenvalues of q_ω are complex [97] and take the form:

$$\tau_\omega = \frac{\partial \phi_t}{\partial \omega} - \mathrm{i}\frac{\partial \ln(|\vec{v}_r|)}{\partial \omega}, \tag{3.8}$$

where ϕ_t is the global transmission phase, i.e., $\vec{v}_r = |\vec{v}_r|\hat{v}e^{\mathrm{i}\phi_t}$ ($\hat{v}_r$ is the unit vector of $\vec{v}_r$). The real part of τ_ω, i.e., $\mathrm{Re}(\tau_\omega) = \partial\phi_t/\partial\omega$, reflects the frequency derivative of the transmission phase and is therefore proportional to the time-delay of the eigenstate $\vec{u}_l$. The imaginary part, $\mathrm{Im}(\tau_\omega)$, describes how the transmission $|\vec{v}_r|$ changes with respect to a change of the frequency ω as can be seen from Eq. (3.6), $|\vec{v}_r(\omega_0 + \Delta\omega)| \approx \exp[-\mathrm{Im}(\tau_\omega)\Delta\omega]|\vec{v}_r(\omega_0)|$. Whereas the operator Q_ω can be computed straightforwardly, computing q_ω and its eigenstates is more challenging, since the ordinary inverse of t appearing in Eq. (3.5) does not exist if t is non-square or singular. In the appendix A.4 we thus introduce an effective inverse that still allows for the calculation of q_ω.

After introducing the Wigner-Smith time-delay operator Q_ω, its non-Hermitian counterpart q_ω and the properties of principal modes, we show in the next section that we can use these operators to generate so-called particle-like states, which are scattering states that have a trajectory-like wave function.

3.1 Particle-like states in a microwave cavity[6]

When an arbitrary wave enters a cavity, it gets reflected multiple times at the boundaries such that, finally, the wave will be distributed throughout the cavity, as can be seen for example in Fig. 1.2(a). As numerically shown in Ref. [65] and experimentally demonstrated in Ref. [66], shaping the wave at the input of the cavity according to eigenstates of the time-delay operator in Eq. (3.1), we may get wave states that feature a beam-like (or particle-like) wave function instead of being spread in the entire cavity. The wave function of such particle-like states stays collimated along the whole scattering region, or in other words, the wave function

---

[6] The results presented in this section were achieved in close collaboration with Ulrich Kuhl and his former PhD-student Julian Böhm from the Université Côte d'Azur as well as with Philipp Ambichl who is a former member of our group. I performed the numerical simulations under the supervision of Philipp Ambichl, whereas Julian Böhm conducted the experiment under the supervision of Ulrich Kuhl. The text in this section partially follows our joint publication [67], from which also the figures were taken.

occupies a bundle of classical particle trajectories. Such particle-like states live in the subspace of fully transmitted or fully reflected states, just like particles that can either traverse the scattering region or get reflected back at some boundary or obstacle. In a two-port system as, e.g., shown in Fig. 1.1(b), the time-delay operator in Eq. (3.1) takes the block-form $Q_\omega = [Q_{11}, Q_{12}; Q_{21}, Q_{22}]$. It was shown that particle-like states are those eigenvectors of Q_ω that are simultaneously eigenvectors of the sub-block $Q_{11} = -\mathrm{i}(r^\dagger \partial r/\partial \omega + t^\dagger \partial t/\partial \omega)$ and additionally lie in the nullspace of Q_{21} [65]. In view of an experimental realization of such particle-like states, the Wigner-Smith time-delay operator suffers from the disadvantage that the construction of Q_{11} involves the transmission matrix t as well as the reflection matrix r (measuring both t and r is challenging experimentally).

Here, we present a microwave realization of particle-like states that involves only the knowledge of the transmission matrix t. A first experimental realization of particle-like states using elastic waves in a cavity was reported in Ref. [66], where, however, the states were obtained by a numerical synthesis of experimentally measured system excitations. Our microwave experiment is an *in situ* realization by means of an active input shaping, thus generating such particle-like states directly.
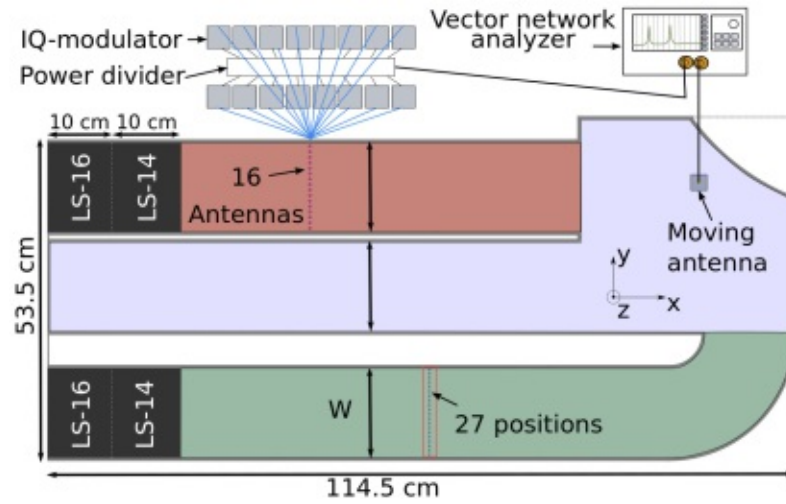
Fig 3.1: Sketch of the experimental setup. A two-dimensional microwave cavity is excited by 16 antennas (left upper corner) placed in the incoming lead (red-colored area). The antennas are connected to IQ-modulators controlling amplitude and phase of the microwave signal, whereas the IQ-modulators themselves are fed by a vector network analyzer. The chaotic scattering region (light blue area) is connected to the incoming lead and an outgoing one (green area). Both leads are closed by absorbing foam material (LS-14,LS-16). The dotted line in the exit lead indicates the 27 positions where the movable antenna is placed for the measurement of the complex transmission matrix t. The red square in the exit lead marks the area for the computation of I_{ob} and I_{em} (see text).

The scattering setup with which we investigate the appearance of particle-like states is shown in Fig. 3.1. A chaotic scattering region is attached to an incoming lead and an outgoing lead (see red, light blue, and green areas in Fig. 3.1 respectively). The width of the lead W of $14\,\mathrm{cm}$ allows the propagation of 16 transverse-electrical modes (TE modes) in the entrance and the exit lead at the working frequency of $\nu_0 = \omega_0/2\pi = 17.5\,\mathrm{GHz}$ which corresponds to a wavelength in air of $1.71\,\mathrm{cm}$. These 16 modes are excitable via 16 antennas where each antenna is connected to one IQ-modulator, which controls amplitude and phase of the microwave signal passing through. The IQ-modulators themselves are fed by a vector network analyzer connected to a power splitter. The ends of the waveguide are filled with absorbing foam material to reduce reflections. The cavity is closed by a top metallic plate with a $5 \times 5\,\mathrm{mm}^2$ grid of holes allowing us to introduce a movable antenna which measures the electric field at any given hole position. The long middle part located between incoming and outgoing lead serves as a verification to show that particle-like states avoid this region which is usually entered by arbitrary scattering states.

The goal is now to create scattering states that get fully transmitted through the setup by shaping the wave in the incoming lead with the 16 antennas placed there. The strategy that we follow to obtain such scattering states is the concept of the time-delay operator in Eq. (3.1) introduced in the last section. As in most experiments, we do not have access to the full scattering matrix S which is needed to calculate Q_ω, however, we show in the following that the information of the transmission matrix t (which is accessible in our setup) is sufficient to find particle-like states by using the operator q_ω in Eq. (3.5). In order to identify particle-like states among all the other eigenstates of q_ω we make use of the corresponding eigenvalues $\tau_\omega^{(i)}$ in Eq. (3.8). Since particle-like states are highly collimated and are not distributed all over the scattering region, the time it takes them to traverse the scattering region is typically much smaller than for other scattering states that get scattered multiple times inside the scattering region. Because $\mathrm{Re}[\tau_\omega^{(i)}]$ measures this scattering time, particle-like states can be identified by a small value of $\mathrm{Re}[\tau_\omega^{(i)}]$. Furthermore, particle-like states feature a small $\mathrm{Im}[\tau_\omega^{(i)}]$ since for fully transmitting and spatially confined scattering states the transmitted intensity barely changes with input frequency ω as compared to states that get scattered multiple times. In the following, we skip the index i of the eigenstates/eigenvalues to ensure a better readability.

The first step in calculating eigenstates of q_ω is to measure the full transmission matrix $t(\omega)$ in a certain frequency window around the working frequency ω_0, followed by a Fourier filtering to reduce noise effects (for details see supplementary material of Ref. [67]). The transmission matrix is set up by injecting a signal through one of the 16 antennas in the incoming lead at one time and measuring the signal in the outgoing lead with the moving antenna at 27 positions which are

marked in Fig. 3.1, i.e., the transmission matrix is a rectangular matrix of size 27×16. Since the transmission matrix is non-square we cannot calculate its ordinary inverse which is needed to construct q_ω in Eq. (3.5). Therefore, we apply the technique described in the appendix A.4 and work with the operator $\tilde{q}_\omega$ which only includes a sub-part of t associated with a certain number N_η of highly transmitting channels, with η being the cut-off transmission value. We tested empirically that the smallest imaginary parts of the eigenvalues, $\mathrm{Im}(\tau_\omega)$, which provide an indicator for the quality of particle-like states, are obtained by taking the highest $N_\eta = 7$ transmitting channels for the calculation of $\tilde{q}_\omega$. Once $\tilde{q}_\omega$ is constructed, we can calculate its eigenstates, inject them into our system and verify their particle-like shape by measuring the corresponding electric field with the movable antenna.
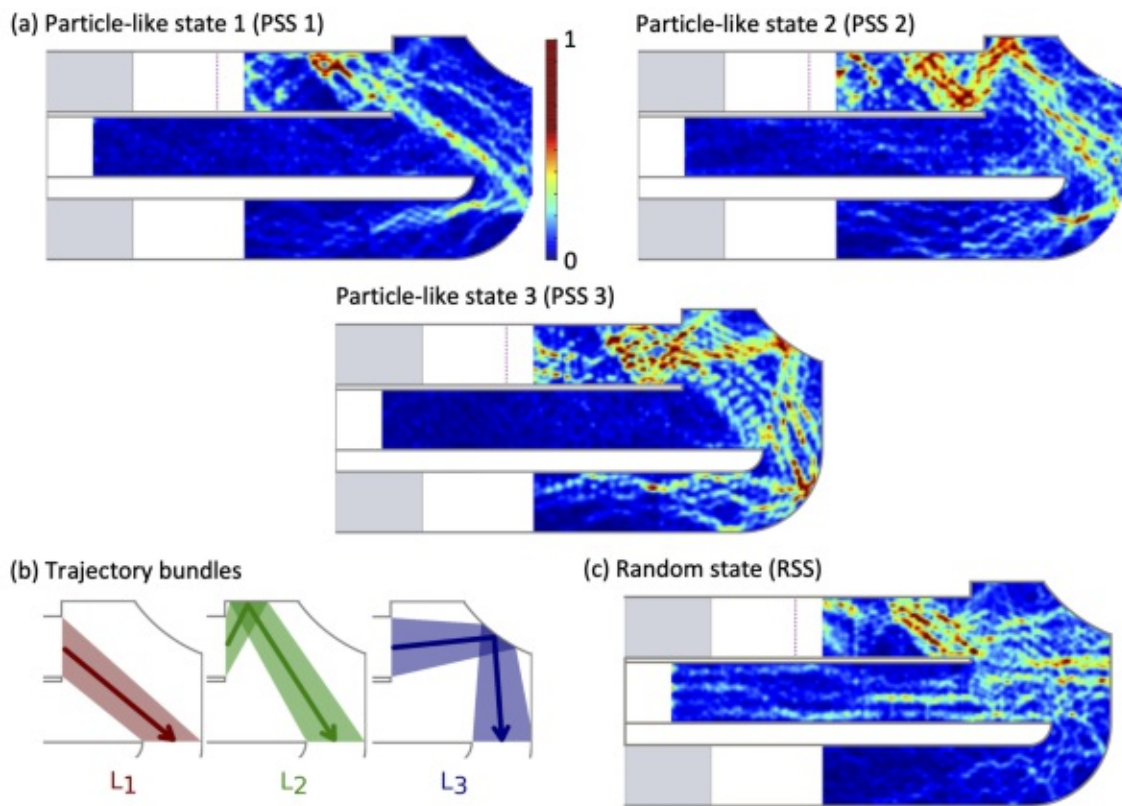
Fig 3.2: (a) Intensity distribution of the particle-like scattering states which are experimentally obtained by wavefront shaping of the incident wave in the incoming lead. (b) Central path lengths of the corresponding classical trajectory bundles of the particle-like scattering states ($L_1 = 33.3\,\mathrm{cm}$, $L_2 = 50.0\,\mathrm{cm}$, $L_3 = 49.1\,\mathrm{cm}$). (c) Typical intensity distribution when only one single antenna is excited (here: second antenna from top). Note that the intensities in panels (a) and (c) are normalized each to a maximum (minimum) value of 1 (0).

At first we investigate the eigenstate with the smallest value of $\text{Re}(\tau_\omega)$, i.e., with the shortest time-delay. The corresponding intensity distribution can be seen in Fig. 3.2(a) top left panel (PSS 1), where the wave function shows the predicted behavior of following the shortest trajectory bundle going directly from the incoming to the outgoing lead [see red bundle in Fig. 3.2(b) left]. In a next step we investigate particle-like states with larger time-delays, which correspond to the green and the blue classical trajectory bundles shown in Fig. 3.2(b). The trajectories of these two bundles turn out to have almost the same length ($L_2 = 50.0\,\text{cm}$ and $L_3 = 49.1\,\text{cm}$) and since similar path lengths lead to similar time-delays, the operator q_ω cannot fully discriminate between these two scattering states. While the particle-like state with the second smallest eigenvalue corresponds quite well to the green classical bundle [see Fig. 3.2(a) top right panel (PSS 2)], the state with the third largest eigenvalue [see Fig. 3.2(a), bottom panel (PSS 3)] mixes both bundles, green and blue. In other words, PSS 2 and PSS 3 corresponding to these bundles are in a near degenerate superposition with path contributions of both length L_2 and L_3.

In order to demix degenerate particle-like scattering states, for example PSS 3 in Fig. 3.2(a), we can analyze the state's angular contribution. As described in Chapter 1 one can use angular eigenstates $\vec{k}_y^{(n)}$ (where n denotes the n-th eigenstate of the wave number operator k_y) as a basis to analyze the different angular components of an arbitrary incident wave. One such eigenstate with a well-defined incidence angle can be seen in Fig. 1.2(c). Due to the fact that the classical trajectory bundles L_2 and L_3 in PSS 3 obviously belong to different angles of incidence, we show that demixing PSS 3 is possible by discriminating between the angular components that belong to one or the other classical trajectory bundle. In order to show the efficiency of this method numerically, we first reconstruct the experimental observation of PSS 3 by coherently superimposing two particle-like states that correspond to the trajectory bundles L_2 and L_3, which do not mix in our numerical simulations due to the absence of experimental imperfections. This scattering state is now decomposed into the basis spanned by the angular eigenstates $\vec{k}_y^{(n)}$ with corresponding expansion coefficients c_n and weighting factors $|c_n|^2$, see Fig. 3.3(a). The coefficients are sorted by the eigenvalues of the corresponding eigenstates $\vec{k}_y^{(n)}$ starting from large negative eigenvalues (i.e., large negative angles) to large positive eigenvalues (i.e., large positive angles). We can see that the angular decomposition of PSS 3 has two main contributions – one for very steep angles (with positive and negative sign) and one for rather flat injection angles, corresponding to the trajectory bundles L_2 and L_3, respectively. In a next step, we inject two wave states into the system that consist only of angular components with one of these two contribution (the respective other wave component is suppressed). We end up with two demixed particle-like states with scattering wave functions that follow nicely the trajectory bundles L_2 and L_3, see Fig. 3.3(b) and (c).

In order to highlight the highly collimated wave function of the particle-like
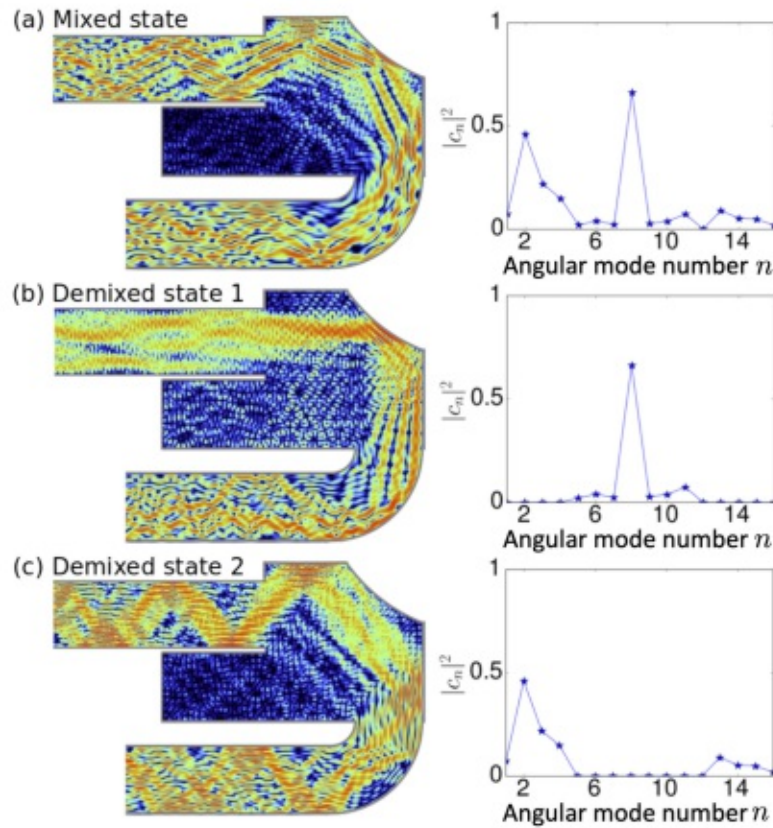
Fig 3.3: (a) (Left panel) Intensity of a wave state similar to PSS 3 [see Fig. 3.2(a) bottom panel], created by numerically superimposing two particle-like states that belong to the classical trajectory bundles L_2 and L_3 shown in Fig. 3.2(b). (Right panel) The corresponding decomposition in angular components is shown through the weights $|c_n|^2$. The angles are sorted in ascending order starting from steep negative angles (on the left) to positive steep angles (on the right). One can see that the mixed state features two main contributions: one for very steep angles (positive and negative) and one for rather flat angles. By sorting these angular components into two separate states, we can demix the state in (a) to obtain two separate particle-like states shown in (b) and (c) whose wave function patterns nicely follow the classical trajectory bundles L_2 and L_3. The simulations here were again performed with the modular recursive Green's function technique (see appendix A.5 for more details)

scattering states, we show in Fig. 3.2(c) the intensity distribution obtained by exciting only a single randomly chosen antenna. We can see that also such a random state shows some intensity maxima within the cavity, however, these maxima do not follow classical trajectory bundles and additionally the state extends into the middle part of the scattering region, which is avoided by all particle-like states.

In a next step we show that particle-like states have a significantly higher spectral robustness of their transverse output profile $\vec{v}_r(\nu)$ as compared to random states, where $\vec{v}_r(\nu) = t(\nu)\vec{u}_l$ is the transverse output profile corresponding to an incoming wave $\vec{u}_l$ (where $\vec{u}_l$ can be a particle-like state or a random state). To be more specific, we define the spectral robustness as

$$\mathrm{Corr}(\nu) = \frac{|\vec{v}_r^\dagger(\nu) \cdot \vec{v}_r(\nu_0)|}{|\vec{v}_r(\nu)||\vec{v}_r(\nu_0)|}, \tag{3.9}$$

which is the normalized correlation between the output vector $\vec{v}_r$ at frequency ν compared to its output at ν_0 (the frequency at which the states are evaluated). In Fig. 3.4 we calculated the correlations with Eq. (3.9) for the three particle-like states and the random state shown in Fig. 3.2. PSS 1 is the state showing the highest output robustness since it goes directly from the incoming to the outgoing lead. PSS 2 and PSS 3 perform a reflection at the convex cavity boundary and are thus more sensitive to small changes in the frequency. This explains why the correlation curve in Fig. 3.4 is flatter for PSS 1 than the one of PSS 2 and PSS 3. The correlation of the random state is, as expected, the lowest.

As particle-like states are highly collimated beams, putting an obstacle in the way of their corresponding classical trajectory bundle would decrease the observed transmission, whereas putting an obstacle outside of the occupied region would affect the wave function only slightly. To test this idea explicitly experimentally, we place altogether 13 cylindrical obstacles forming a rhombic shape into the scattering region of the cavity, see Fig. 3.5(b). The obstacles have an equidistant spacing of about 3.3 wavelengths to make sure that their perturbations are uncorrelated. In order to quantify the change of the transmitted intensity, we evaluate the relative change

$$\Delta I_{\mathrm{rel}} = \frac{I_{\mathrm{ob}} - I_{\mathrm{em}}}{I_{\mathrm{em}}}, \tag{3.10}$$

where I_{ob} is the transmitted intensity when the obstacle is placed inside the cavity and I_{em} is the transmitted intensity for the empty system without the obstacle. The transmitted intensities are obtained by computing the sum of the measured transmitted intensities at 135 positions indicated by the red square in Fig. 3.1. As expected, we can see in Fig. 3.5 that the particle-like states are affected by a strong drop of 30% or more of the transmitted intensity when the scatterer is placed within the bundle supporting the particle-like state. This observation is interesting from a practical point of view if one aims to transmit intensity from the input to the output lead in the presence of obstacles. Once a specific particle-like state is blocked, one can maintain efficient transmission by switching to another state (e.g., from PSS 1 to PSS 2), an option that will not work when operating with random scattering states. Also a global perturbation like uniform absorption will affect particle-like states much less due to their short time-delays.
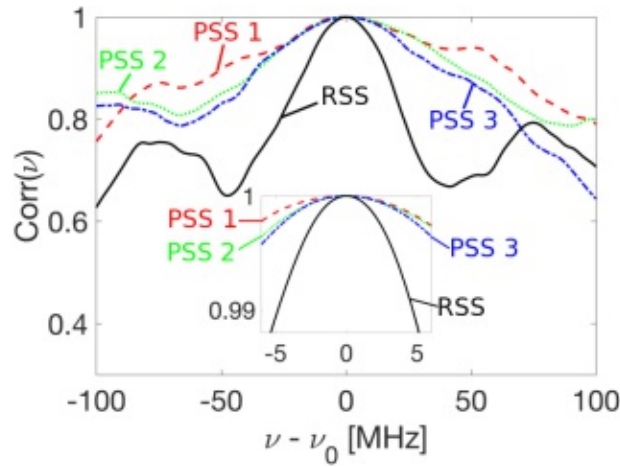
Fig 3.4: Correlation function according to Eq. (3.9) of the output profile of the three particle-like states and the random state shown in Fig. 3.2. The particle-like states are more stable with respect to changes of the incident frequency ν compared to the random state.
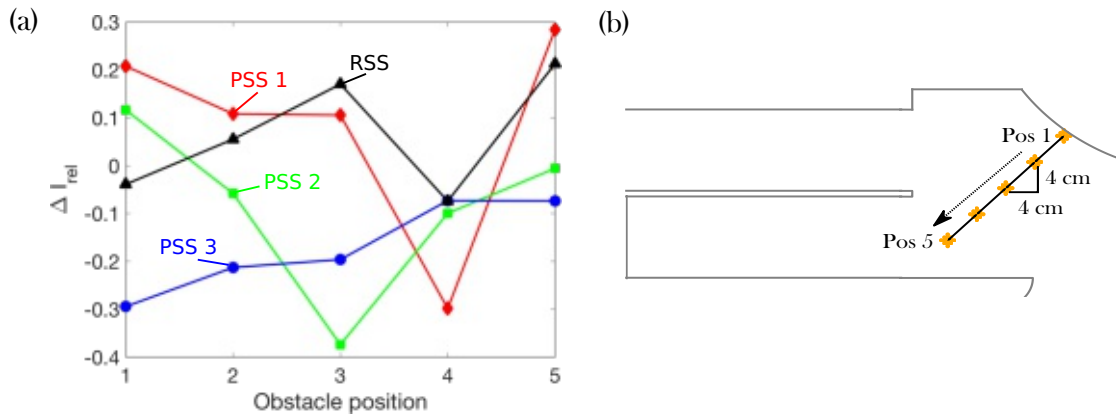
Fig 3.5: (a) Change of the transmitted intensity ΔI_{rel} as defined in Eq. (3.10) of the particle-like scattering states and the random state while moving the rhombic obstacle between position 1 (Pos 1) to position 5 (Pos 5) [see (b)]. PSS 1 and PSS 2 show a significant drop at only one position where the obstacle crosses the corresponding classical trajectory bundle, whereas PSS 3, which is a superposition of two classical bundles, is, as expected, affected by all obstacle positions. The random state shows no indication of a particle-like pattern.

Concluding this section, we experimentally realized particle-like scattering states by means of incident wavefront shaping in a microwave cavity. Such states follow bundles of classical particle trajectories and can be identified with the help of the Wigner-Smith time-delay formalism. We found altogether three particle-like states

and tested their stability with respect to changes of the incident wavelength.

Having shown that particle-like states can be used to generate wave states that stay focused during their entire transmission process even in chaotic cavities, we study in the next section particle-like states in systems with a smooth and correlated disorder which allow for a so-called branched flow.

3.2 Branched flow[7]

When physicists studied how coherent electrons propagate in a two-dimensional semiconductor heterostructure with high mobility, they were very surprised to find in their measurements that the electrons do not spread out isotropically in all directions but rather form a distinct branching pattern along which they seem to flow preferentially [98, 99]. The reason for this unexpected branching lies in the smooth and spatially correlated background potential of the heterostructure [100], which acts like a collection of imperfect lenses [101] that give rise to caustics at which the electronic density is enhanced [102–104]. It was soon understood that the phenomenon of branched flow occurs not only for electron waves in semiconductors but rather for many types of waves and for different length scales up to the formation of hot spots in tsunami waves as a result of the propagation through the rough ocean sea bed [105–111].

Many studies focused on the statistics of this phenomenon [101, 108, 112, 113] and on its origins [100, 101, 114–117], however, the question of how branched flow can be controlled to steer waves through a complex medium has not been addressed so far, since the possibility to shape and manipulate electrons or ocean waves are rather limited. In a new generation of experiments, however, branched flow was observed when coherent laser light propagates through very thin disordered materials such as the surface layer of a soap bubble [118]. Due to this transfer of branched flow to the optical domain, the whole arsenal of wavefront shaping techniques to shape the wavefront of such branched light beams [33, 35] can now be applied.

What we aim to show is that a suitably shaped wavefront that is injected into a system showing branched flow allows us to steer these waves along individual branches, rather than along many of them in parallel. In other words, we try to use the branches as highways for wave propagation such as to navigate a wave to a desired location while maintaining its collimation during the entire scattering process. Our strategy to find the correct wavefronts is to apply the concept of particle-like scattering states, as introduced in the previous section. We expect

---

[7] The results presented in this section were achieved in collaboration with two of my former colleagues Adrian Girschik and Philipp Ambichl. I developed the theory and the concept of addressing individual branches together with Philipp Ambichl, whereas the numerical simulations were performed together with Adrian Girschik. The text and the figures in this section partially go back to our joint publication [68].

our approach to be useful in a variety of different contexts, where steering waves through a complex environment to a predetermined target is a key goal, like in wireless communication [119], in adaptive optics [120], underwater acoustics [121], for wave focusing [7, 36, 48, 69], biomedical imaging [122, 123], as well as for wave control in disordered systems in general [33, 35, 124, 125].
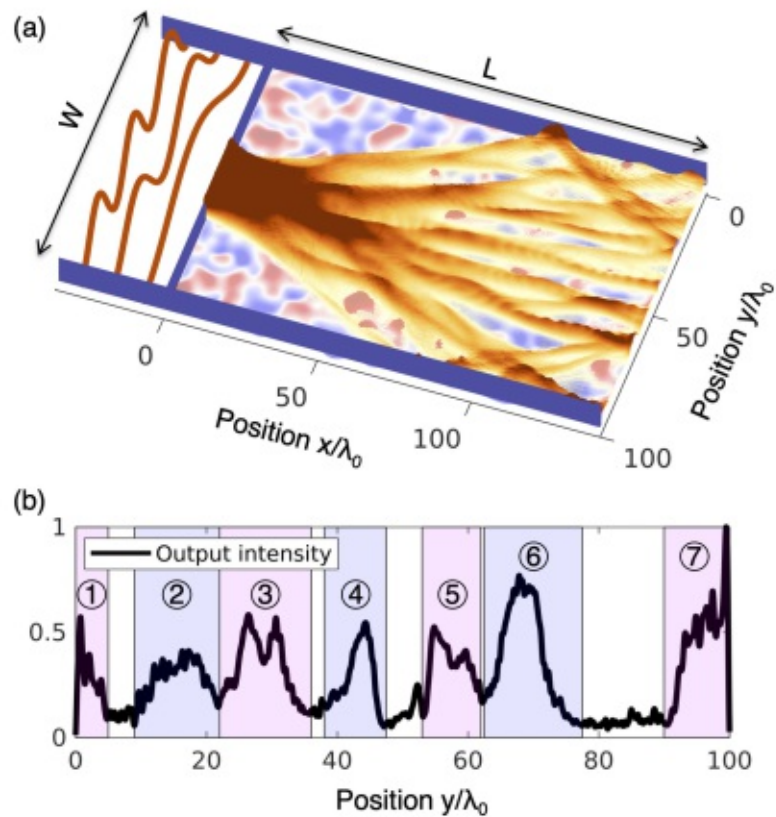
Fig 3.6: (a) Illustration of the setup under study: a waveguide filled with a correlated disorder (center region) of width $W \approx 100\lambda_0$ is attached to an incoming lead on the left (through an aperture, blue) and an outgoing lead on the right (not shown). The smooth disorder refractive index in the waveguide of length $L = 1.4W \approx 140\lambda_0$ is illustrated in blue/red colors. On top of the refractive index the wave intensity is plotted, corresponding to a superposition of the wave intensities of mode 1 to 100 injected through the left lead, resulting in a pronounced branched structure. The first three lead modes are depicted in orange on the left-hand side. The main goal of our study is to separate these branches by suitably shaping the incoming wavefront in the left lead. (b) Intensity output profile as a function of the transverse coordinate y at the right end of the disordered region ($x = L$). The seven maxima labeled from 1 to 7 (highlighted in light blue/magenta) are produced by the arrival of different branches at the output.

The system we consider for our study is shown in Fig. 3.6(a) and consists of a rectangular scattering region of width W and length $L = 1.4W$ that is attached to two straight semi-infinite leads of the same width W on the left and right (only left lead shown), just as described in Fig. 1.1(c). In all the calculations reported in this section, we choose the number of propagating open lead modes to be $N = 200$ and a fixed wave number $k_0 = \mu\pi/W$ of the incoming light [the first three lead modes are indicated in Fig. 3.6(a)]. For simplicity we set $W = \mu = 200.01$ resulting in the following simple expressions for the wave number $k_0 = \pi$ and the wavelength $\lambda_0 = 2$. In units of wavelengths, the system has a width of $W \approx 100\lambda_0$ and a length of $L \approx 140\lambda_0$.

In analogy to the first observation of branched flow where electrons were injected through a constriction (quantum point contact) into a high-mobility electron gas [98], we also include such a constriction in the form of an aperture of width $d = 50.5 \approx 25\lambda_0$ between the left lead and the disordered scattering region (at $x = 0$). In many previous studies the width of the constriction was chosen such that it only allows for one or two modes to propagate through. Here, the 50 modes that we allow to pass provide us with many tunable degrees of freedom as required for shaping the incoming wavefront. We just want to mention here that in a narrow quantum point contact that transmits only a single mode, our method cannot be applied since no wavefront shaping would be possible. The smooth and long-range disorder necessary to observe branched flow is modeled by a spatially dependent index of refraction $n(\vec{r})$ throughout the whole scattering region indicated by the light red/blue color in Fig. 3.6(a). This correlated refractive index $n(\vec{r})$ is characterized by a correlation length $\xi = 6 = 3\lambda_0$, minimum/maximum values: $\min[n(\vec{r})] = 1$ and $\max[n(\vec{r})] \approx 1.19$, and a mean value $\mathrm{mean}[n(\vec{r})] \approx 1.1$ (for more details on the correlated disorder see appendix A.6).

The scalar scattering problem in this two-dimensional setup is again described by the two-dimensional Helmholtz Eq. (A.20) which is solved numerically with the modular recursive Green's function technique [126, 127] (see appendix A.5 for more details). This technique allows not only for efficiently evaluating the scattering states $\psi(\vec{r})$ but also the unitary scattering matrix S.

In order to observe the branched flow of light, we inject the different lead modes as described in Eq. (1.2) from the left into the system through the aperture and superimpose the corresponding wave intensities they give rise to. In the superposition we consider only the first 100 lead modes (out of 200) to avoid high angle scattering and to ensure a high visibility of the individual branches. The branched structure in the propagation of waves through our setup is clearly visible in Fig. 3.6(a).

The challenge we rise to in a next step is to address these branches individually through a suitable coherent superposition of incoming modes in the left lead. The methods we choose for this purpose involve only the transmission matrix t. As the branched flow in our system naturally leads to a concentration of intensity at certain spots at the output, we find that the knowledge of the transmission matrix

t for modes concentrated around these spots is sufficient for a clean separation of branches. In other words, we may restrict ourselves to those regions in space at the output, where the branches arrive. These regions are determined from the intensity profile at the output facet of our system at $x = L$, see Fig. 3.6(b). Seven intensity maxima corresponding to the arrival of different branches are clearly visible in Fig. 3.6(b) and highlighted in light blue/magenta. For each intensity maximum we manually set lower and upper boundaries, which are indicated by vertical lines in Fig. 3.6(b) and define a reduced transmission matrix $\bar{t}$ connecting the incoming lead with the corresponding region at the output (labeled from 1 to 7). In order to obtain $\bar{t}$, we first transform the transmission matrix t given in the mode basis into the spatial basis (see Chapter 1 for details on the transformation). The elements $\bar{t}_{ba}$ of this matrix hence describe the coherent transmission amplitudes from all points a at the input (we choose 200 equidistant points in the input lead corresponding to 200 open lead modes) to all points b around a specific intensity maximum at the output. In this basis, one row of t describes the transmission from the entire incoming lead to only one peak on the right-hand side of the scattering geometry. Thus, if we are interested in the transmission matrix from the left lead to a designated region on the right side, we just need to cut out the corresponding rows falling outside the desired region to finally obtain $\bar{t}$.

Our first approach to achieve clean branch separation is to employ a singular value decomposition (SVD) of $\bar{t}$, i.e.,

$$\bar{t} = U\Sigma V^{\dagger}, \tag{3.11}$$

allowing us to access the transmission eigenvalues $\tau^{(i)}$ in this truncated spatial basis as contained in the real diagonal matrix $\Sigma = \text{diag}\left[\sqrt{\tau^{(i)}}\right]$. The matrix U consists of eigenvectors of $\bar{t}\bar{t}^{\dagger}$ and V consists of eigenvectors of $\bar{t}^{\dagger}\bar{t}$. The largest transmission eigenvalues $\tau^{(i)}$ correspond to those transmission eigenchannels $\vec{\tau}^{(i)}$ (contained in the columns of V) that transmit the most intensity to the desired region at the output. At this point one might be tempted to think that these highly transmitting channels will already constitute the branches we are after. To test this hypothesis, we inject for each of the seven transmission matrices $\bar{t}$, the corresponding transmission eigenchannels with the largest transmission eigenvalues. Checking the corresponding scattering wave functions [see Fig. 3.7(b),(e)-(i),(p),(t)], we find that a clean branch separation is, indeed, possible for a number of cases. We also find, however, that several among the highly transmitting eigenchannels follow two different branches in parallel instead of only one. Figure 3.7(o) shows an example of such a state, where one can clearly see a mixing of one branch propagating directly into the selected region (marked with blue bars at the output) with another branch bouncing off the lower boundary. Demanding high transmission into a desired region by choosing high transmission eigenchannels is thus clearly not enough to guarantee clean branch separation since high transmission can also be obtained by propagating along multiple branches at once. In a possible optical

experiment such a mixing can be expected to be even more prevalent than in our numerical example, simply because optical implementations can typically involve a large number of branches [118].

In order to be able to address also such mixed branches individually, we now apply the concept of particle-like states as introduced in the last section. The key idea here is that two branches that may both be highly transmitting [like those in Fig. 3.7(o)] can be distinguished by their different time-delays (as determined by the different branch lengths). Thus, we calculate eigenstates of $q_\omega = -\mathrm{i}\bar{t}^{-1}\partial\bar{t}/\partial\omega$ for each of the seven reduced transmission matrices $\bar{t}$. Since the ordinary inverse of $\bar{t}$, which is needed to calculate q_ω, cannot be taken due to its non-regularity, we have to apply again the technique introduced in appendix A.4, where we only include a sub-part of $\bar{t}$ associated with a certain number N_η of highly transmitting channels (with η being the cut-off transmission value). Using this technique, we obtain the reduced time-delay operator $\tilde{q}_\omega$ operating in the subspace of highly transmitting states only. In practice, a value of $\eta = 0.8$ proved suitable for all our calculations. The imaginary parts of the complex eigenvalues of $\tilde{q}_\omega$ are, again, very small and the real parts can still be used as a good measure for the physical time-delays [67].

To put this method directly to the test, we turn our attention to the state shown in Fig. 3.7(o) featuring a mixture of two branches with different path lengths and, correspondingly, different time-delays. A singular value decomposition of $\bar{t}$ reveals that it contains 9 singular values larger than $\eta = 0.8$. With this knowledge we can now construct $\tilde{q}_\omega$ and, indeed, find among its eigenstates $\vec{u}^{(i)}$ the desired wave fields that follow the two involved branches individually [see Fig. 3.7(r) and (s)]. Since the eigenvectors $\vec{u}^{(i)}$ feature injection only from the left-hand lead, they should carry the subscript l, i.e., $\vec{u}_l^{(i)}$, however, we skip this subscript for better readability.

Restricting the construction of time-delay eigenstates to the subspace of high transmission thus yields already very good results. Using this method, we, however, also observed a few time-delay eigenstates that mix two different branches as, e.g., shown in Fig. 3.7(j). These two branches, on the other hand, turn out to be individually addressable through those transmission eigenstates $\vec{\tau}^{(i)}$ with the smallest time-delays [see Fig. 3.7(g) and (i)]. The time-delay of a transmission eigenstate $\vec{\tau}^{(i)}$ can simply be calculated by taking the expectation value with the time-delay operator q_ω, i.e., $[\vec{\tau}^{(i)}]^\dagger q_\omega \vec{\tau}^{(i)}$.

One may thus also decide to turn the above strategy on its head and look for transmission eigenstates in the subspace of short time-delays. Since neither one of these opposite strategies seems to have an a priori advantage, we now combine them with each other in a synergistic way to improve our results even further:

(i) We evaluate all eigenstates $\vec{\tau}^{(i)}$ of $\bar{t}^\dagger\bar{t}$ and $\vec{u}^{(i)}$ of $\tilde{q}_\omega$, for all of the seven transmission matrices $\bar{t}$ corresponding to regions of maximum intensity shown in Fig. 3.6(b).

(ii) We select those states that are identical in both eigenstate sets, since they turn out to be individual branch excitations in all of the observed cases. To do this,
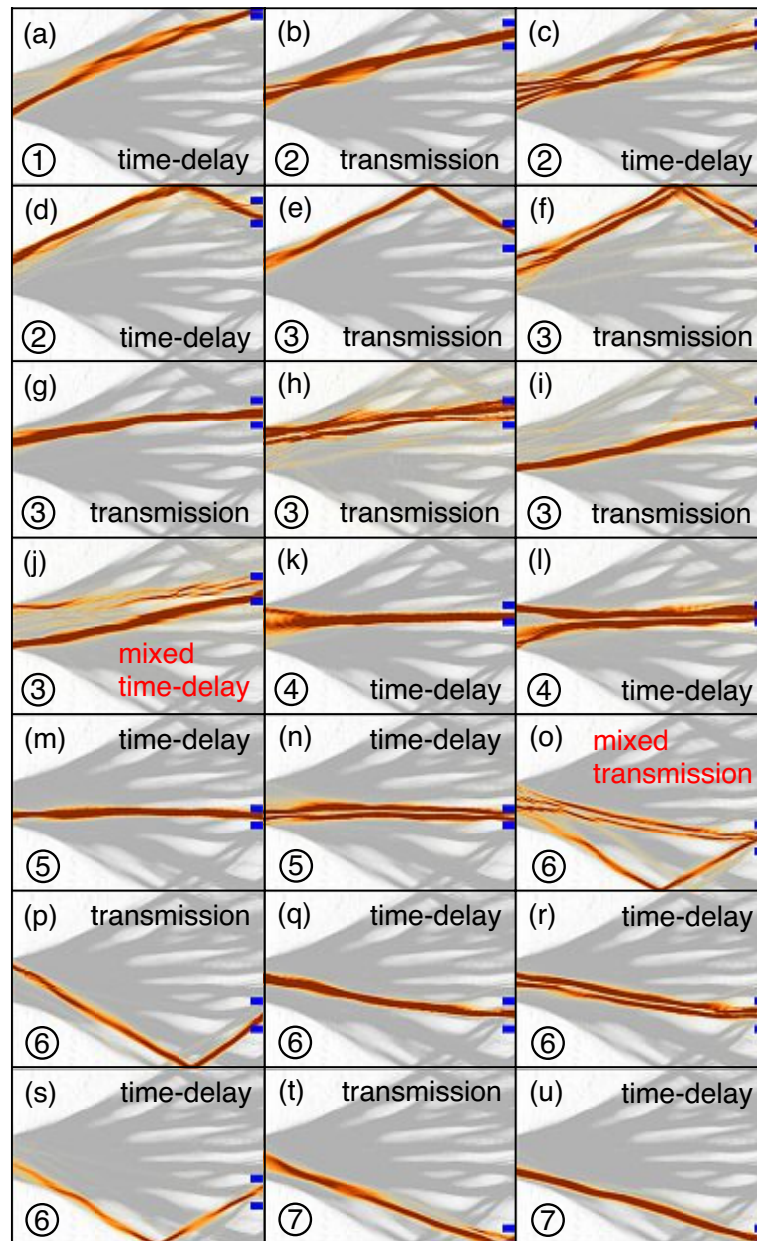
Fig 3.7: Transmission and time-delay eigenstates of the system shown in Fig. 3.6 calculated from the transmission matrices $\bar{t}$ connecting the incoming lead with the seven different output regions marked in Fig. 3.6(b) (see blue horizontal bars here). The branched structure [see Fig. 3.6(a)] is drawn as a gray background. We show all eigenstates that are selected by our procedure [steps (i)-(iii) in the main text] with black text labels and two examples of eigenstates that are filtered out by our procedure since they address two different branches at once (red label). The states are ordered according to their output region on the right (see numbers 1 to 7). The average transmittance of all states with black label is around 89% into the region marked by the blue bars.

we project each time-delay eigenvector $\vec{u}^{(i)}$ onto each transmission eigenvector $\vec{\tau}^{(i)}$, such that we end up with the matrix elements $m_{ij} = [\vec{u}^{(i)}]^\dagger \vec{\tau}^{(j)}$. (The matrix m is not unitary since the eigenstate-sets are not complete). For the case that two eigenvectors are the same, the matrix m has only one significant non-zero element in the corresponding row/column. Practically, we consider two eigenvectors to be the same when $|m_{ij}| > 0.9$.

(iii) In a last step, we deal with those eigenstates that consist of more than one contribution from the respective other eigenstate set, i.e., that have more than one non-zero element in the corresponding row/column of m. Our task here is to select those states that consist of only single branches and to discard those states that propagate along more than one branch at once, since the coefficients m_{ij} do not indicate per se which states consist of single branches only. As we show here, the spatial and/or angular distribution of an eigenstate at the input aperture provides us with sufficient information to perform this task since an eigenstate exciting only one branch will be spatially more confined and will radiate into a smaller angular region than a state addressing multiple branches. Assuming that the transmission matrix $\bar{t}$ is measured in the spatial pixel basis, the eigenvectors $\vec{u}^{(i)}$ and $\vec{\tau}^{(i)}$ are naturally given in this spatial basis as well. By plotting the absolute value of the coefficients $|c_n^y|$, where n is the n-th component of the vector $\vec{u}^{(i)}$ or $\vec{\tau}^{(i)}$, as a function of the transverse coordinate at the aperture ($x = 0$), we can easily generate the spatial distribution of an eigenstate. To estimate the angular distribution of an eigenstate at the aperture, we decompose the eigenvectors $\vec{u}^{(i)}$ and $\vec{\tau}^{(i)}$ into the angular basis spanned by the eigenvectors $\vec{k}_y^{(n)}$ (see Chapter 1 for more details on the angular basis) which have a well-defined transverse wave vector component and analyze the different angular components $|c_n^k|$. Figure 3.8(a) and (b) display the spatial and angular components of the transmission eigenstate shown in Fig. 3.7(o) (red) and the time-delay eigenstate in Fig. 3.7(r) (blue). We see that the spatial profile of the transmission state is broader and that it features more angular components than the time-delay state. We can therefore conclude that the transmission state is more likely to address multiple branches, whereas the time-delay state addresses only one single branch, which is confirmed by the wave plots shown Fig. 3.7(o) and Fig. 3.7(r). In Fig. 3.8(c) and (d) we plot the same distributions for the time-delay state shown in Fig. 3.7(j) and the transmission state shown in Fig. 3.7(i). From Fig. 3.8(c) we deduce that the time-delay state consists of more than one branch due to the larger spatial distribution, which is confirmed by the wave plots. We successfully applied this procedure to all eigenstates $\vec{u}^{(i)}$ and $\vec{\tau}^{(i)}$ from which we can conclude that the spatial and angular distribution of the time-delay and transmission states can be used to find those states out of both eigenstate sets (time-delay and transmission eigenstates) that excite only one single branch.
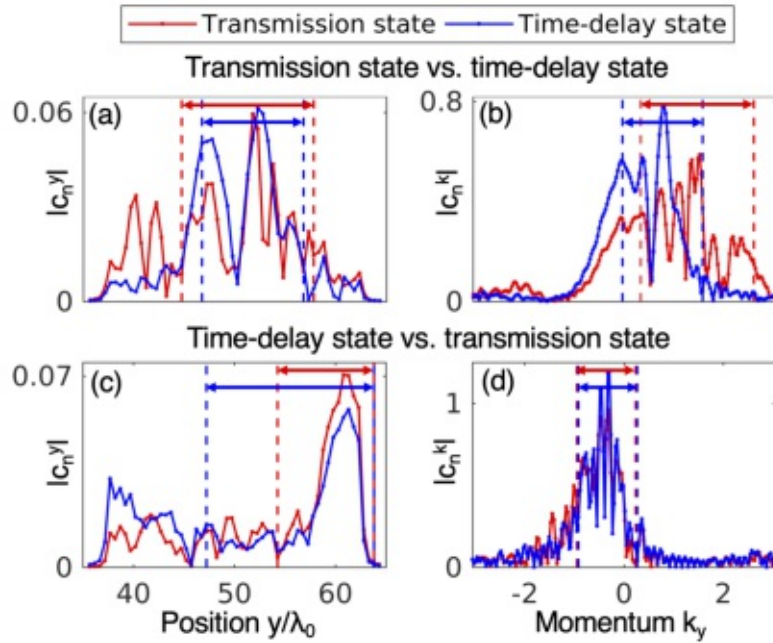
Fig 3.8: (a),(b) Spatial (left) and angular distribution (right) at the input aperture (located at $x = 0$ between $y/\lambda_0 \approx 37$ and $y/\lambda_0 \approx 62$) of the transmission (red) and time-delay state (blue) shown in Fig. 3.7(o) and Fig. 3.7(r), respectively. The different widths of the distributions indicate that the transmission state is likely to excite more than one branch at once. (c),(d) Spatial (left) and angular distribution (right) of the time-delay (blue) and transmission (red) state shown in Fig. 3.7(j) and Fig. 3.7(i). From the widths of the spatial distributions shown in (c) we can conclude that the transmission state is more likely to excite only one single branch, which is confirmed by the wave plots. The widths of the normalized distributions are quantified by the interval around the maximum value of the distribution (indicated by the vertical dashed lines) in which 60% of the distribution lies.

Following the above three steps (i)-(iii), which notably rely only on the experimentally accessible transmission matrices $\bar{t}$, we obtain well-separated branch states (see all states in Fig. 3.7 with a black text label) that stay collimated throughout the entire scattering region and that feature an average transmittance of over 89% into one of the designated seven output regions. These results show that our method leads to a channeling of waves through the disordered region and to a well-controlled branched flow. An interesting detail that we emphasize here is that our approach not only yields a single state for each individual branch but, in fact, also states that propagate along the same branch but with a higher transverse quantization; see, e.g., Fig. 3.7(c),(f),(h),(l),(n),(r) [65].

To underscore the non-trivial nature of these collimated branch states that we identify here, we inject several of the states shown in Fig. 3.7 into a clean waveguide

without any disorder. The results are displayed in Fig. 3.9, showing that these states feature a considerably reduced collimation as compared to the case including the disorder (see figure insets). This observation demonstrates that the states we identify here do not just rely on a trivial injection with a narrow angular distribution at the input and that the disorder plays a crucial role for the states' collimation.
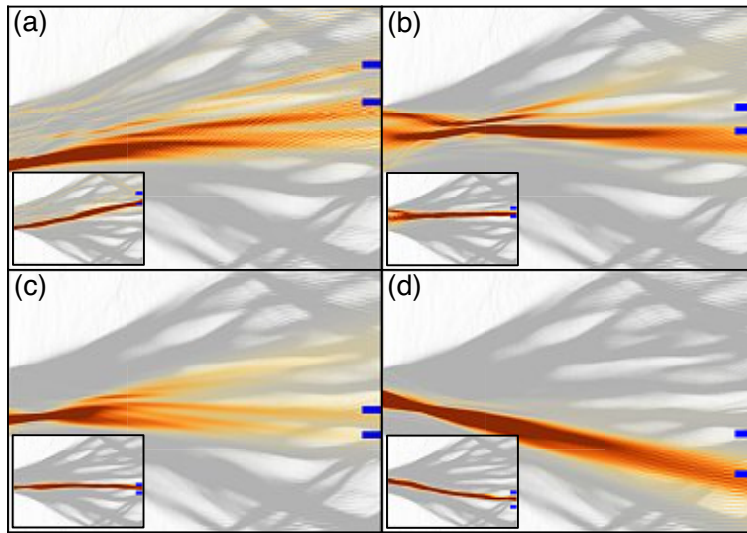

Fig 3.9: (a)-(d) Eigenstates from Fig. 3.7(i),(k),(m),(q) injected into an empty waveguide without the disordered refractive index. The fact that removing the disorder refractive index leads to a defocusing demonstrates that the formation of collimated branch states crucially relies on the presence of the underlying disorder landscape. The blue bars indicate the region where the branch exits the scattering region in the presence of the disorder (see insets).

In a last part of this study, we also demonstrate explicitly that our collimated single-branch states allow for the transmission of pulses along a branch. The frequency stability that is necessary to allow for a stable pulse propagation is experimentally shown for particle-like states in the last section in Fig. 3.4. Thus, we expect that the propagation of a pulse should also be possible in our branched flow system. Consider here, as an example, the time-delay eigenstate shown in Fig. 3.10(a) that propagates along a certain branch. Taking a superposition of this branch state at different frequencies to form a Gaussian wave packet, we obtain a pulse propagating along the selected branch as shown in Fig. 3.10(b)-(d) at three different time-steps ($t_1 < t_2 < t_3$). We observe that the pulse transits the system while staying on the selected branch throughout the entire transmission process.

In summary, this section demonstrates how to control the flow of waves through a correlated and weak disorder refractive index landscape. Such systems give rise to branches along which incoming waves travel through the disorder. We introduce a method that allows us to inject waves in such a way that almost all the flow travels
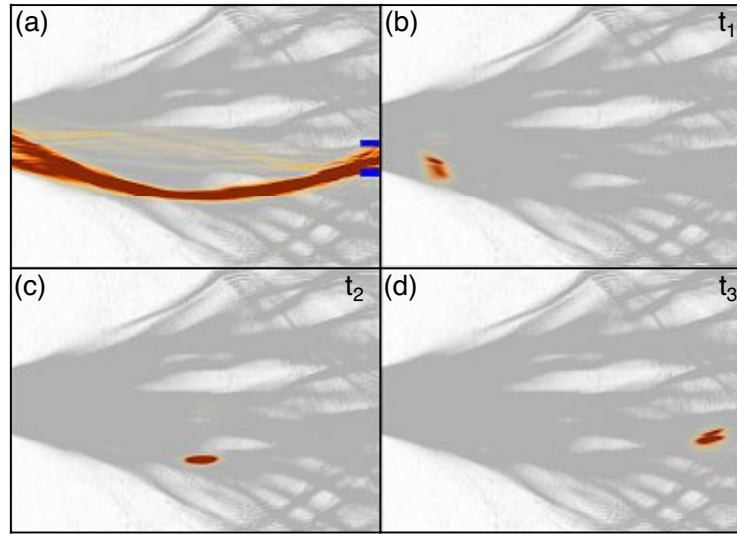
Fig 3.10: (a) Time-delay eigenstate propagating along one single branch in a disorder landscape [to prove the general applicability of our approach, a different disorder realization was used as in Fig. 3.6(a)]. (b)-(d) Pulse propagating along the branch shown in (a) at three different time-steps ($t_1 < t_2 < t_3$). The pulse remains spatially confined while traversing the disorder along the branch shown in (a). The Fourier spectrum of the pulse is Gaussian-shaped with a standard deviation of $\sigma \approx 0.034 k_0$, with k_0 being the wave number.

along a single branch alone. This non-trivial finding can even be extended to the temporal domain, as we show by creating pulses that remain on a single branch throughout the entire transmission process. Implementing such concepts in optics requires only a small sub-part of the transmission matrix and is thus within reach of present-day technology. We expect our work to be generalizable from scalar to vector waves and from two to three dimensions, where it may give rise to interesting applications in communication and imaging technology.

In the previous two sections we show that eigenstates of q_ω, which are states that are by construction robust with respect to changes of ω, can have very interesting properties, like having a particle-like wave function. In the next chapter we take the concept of principal modes and time-delay eigenstates to a new level such as to produce states that – instead of being insensitive with respect to a frequency variation – are invariant with respect to changes in system configurations, like a local shift of a designated scatterer inside the disordered medium. We show in the next chapter that with eigenstates of such a corresponding operator we can transfer a well-defined momentum onto a specific target buried inside a disorder. Moreover, we show that we can also generate states that apply to a target a well-defined pressure or torque as well as to achieve a focus inside the target.

Chapter 4

Generalized Wigner-Smith operator[8]

While the time-delay operator and principal modes have already led to numerous insights, we now introduce a new approach in which we generalize the Wigner-Smith operator by using derivatives with respect to different parameters than the frequency. In Eq. (3.1) we can simply substitute $\omega \to \alpha$ and obtain what we call the Generalized Wigner-Smith (GWS) operator

$$Q_\alpha = -\mathrm{i}S^{-1}(\alpha)\frac{\partial S(\alpha)}{\partial \alpha}, \tag{4.1}$$

featuring eigenstates whose output patterns are stable to first order with respect to changes of the parameter α, in the same way as principal modes are invariant to changes of the incident frequency ω. We emphasize here that the parameter α can literally be any parameter the scattering matrix depends on, such that Eq. (4.1) defines a whole new class of operators that inherit the favorable characteristics of the Wigner-Smith time-delay operator which can now be seen as just one example of GWS-operators with $\alpha = \omega$. In order to give the eigenvalues of Q_α, $\tau_\alpha^{(i)}$, a physical meaning, one can proceed by analogy: the eigenvalues $\tau_\omega^{(i)}$ of the Wigner-Smith operator Q_ω (involving a derivative with respect to the frequency ω) are the time-delays of the corresponding eigenstates. As time and frequency are conjugate quantities (in the sense used for a Fourier transform), the GWS-operator Q_α (involving the derivative with respect to α) should have eigenvalues $\tau_\alpha^{(i)}$ that are the conjugate quantity to α. Important to mention is the fact that the quantity α can not only be a global parameter that describes the entire scattering system (like the frequency ω), but also a local parameter such as the position of a single scatterer. For this specific case where α is the position of a scatterer, i.e., $\alpha = x$,

---

[8] The results presented in this chapter were obtained in collaboration with my former colleague Philipp Ambichl, my current colleagues Michael Horodynski, Matthias Kühmayer and Kevin Pichler, Ulrich Kuhl and his former PhD-student Julian Böhm from the Université Côte d'Azur and Yan V. Fyodorov from King's College in London. The theoretical analysis was carried out by Philipp Ambichl, Michael Horodynski, Matthias Kühmayer and myself, whereas the numerical simulations were mainly performed by Matthias Kühmayer. The experiments were conducted by Julian Böhm and Kevin Pichler under the supervision of Ulrich Kuhl. The text and the figures in this section partially go back to our joint publications [69, 70].

the corresponding GWS-operator would give eigenstates whose eigenvalues have the dimension of a momentum.

In the following we study these new operators Q_α in a waveguide system as shown, for example, in Fig. 1.1(c), where a designated target is surrounded by a disorder formed by randomly placed scatterers. We demonstrate that by choosing different parameters α such as the target's position, radius, angular orientation or refractive index, the corresponding eigenstates of Q_α apply to the target a well-defined momentum, pressure or torque as well as to achieve a focus inside the target.

In order to understand the eigenvalues of the GWS-operator Q_α, $\tau_\alpha^{(i)}$, we can use the following relation which is derived in the supplemental material of Ref. [70]:

$$\langle u|Q_\alpha|u\rangle = \frac{1}{2}\langle\psi_u|\frac{\partial V}{\partial\alpha}|\psi_u\rangle, \qquad (4.2)$$

where $|u\rangle$ is an arbitrary incoming wave state written as a ket in the bra-ket notation (typically a vector $\vec{u}$ in a certain basis), $|\psi_u\rangle$ is the resulting wave field inside the scattering system (typically a spatially resolved field distribution) and V is defined as $V = k_0^2 n^2(x, y)$ with k_0 being the vacuum wave number and $n(x, y)$ the refractive index. Equation (4.2) is a very powerful tool since it relates asymptotic quantities such as Q_α and the incident wavefront $|u\rangle$ with local quantities such as the wave function $|\psi_u\rangle$ and the variations of the refractive index landscape $\partial V/\partial\alpha$. Please note that the derivative with respect to α in Eq. (4.2) does only act on V and not on the wave function $|\psi_u\rangle$. Using Eq. (4.2) one can ask the question on how to shape the incident wavefront $|u\rangle$ to manipulate a target in a specific way (via $\partial V/\partial\alpha$). In the following we choose for α different parameters of a target and study the physical meaning of the eigenvalues of the corresponding GWS-operator Q_α with the help of Eq. (4.2). Specifically, we show in the following that a small rotation of a target yields eigenstates that transfer a well-defined angular momentum onto the target; shifting the target's position $\alpha = \vec{r}$ provides the momentum transfer; varying the radius of a circular target $\alpha = R$ grants control over the radiation pressure exerted on it; and changing the value of the dielectric constant $\alpha = \varepsilon = n^2$ determines the wave intensity stored inside the target.

We investigate the different GWS-operators Q_α directly in the experiment using a rectangular microwave waveguide as shown in Fig. 4.1, similar to the one used in Section 3.1. The setup gives access to the full scattering matrix and allows for the measurement of the electric field through holes in the top plates. Eight antennas on both ends of the waveguide allow to inject any desired wavefront into the scattering region. The operation frequency is 12.75 GHz, resulting in a wavelength of $\lambda_0 = 2.35$ cm at which eight transverse modes can propagate. The disorder is simulated by randomly placed Teflon scatterers around the target which is located in the middle of the setup.
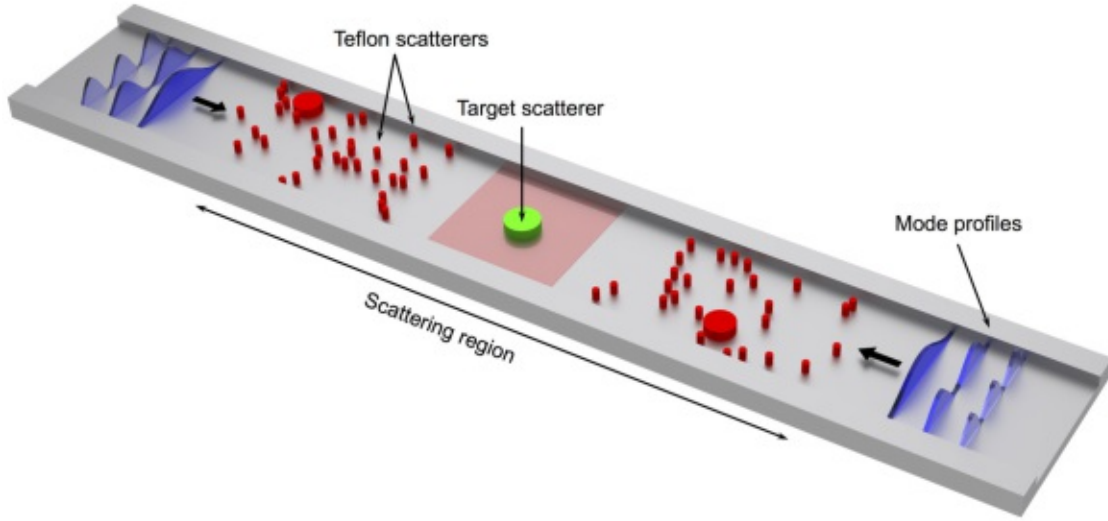
Fig 4.1: Illustration of the waveguide geometry used in the experiment. The top plate (not shown) features a grid of small holes through which an antenna can enter the system to measure the electric field. Red cylinders indicate the randomly distributed circular Teflon scatterers (dielectric constant $\varepsilon = 2.0736$ and radii $2.55\,\mathrm{mm}$ or $11\,\mathrm{mm}$) and the green cylinder in the middle indicates a target scatterer, whose material, size and shape is chosen specifically for each GWS-operator we investigate. The red-shaded area indicates the region shown in Figs. 4.2-4.5. Eight antennas on each side (not shown) are used to measure the full scattering matrix and to inject the desired scattering states.

In the first example we choose the orientation angle φ of a complex-shaped metallic target embedded in an empty waveguide to be the parameter α, see Fig. 4.2(a). In order to calculate the corresponding GWS-operator $Q_\varphi = -\mathrm{i}S^{-1}\partial S/\partial\varphi$, we measure the scattering matrix for three different angular positions of the target $\varphi = \pm 5°$ and $0°$ to approximate the derivative $\partial S/\partial\varphi$ with a finite difference. As analytically shown in the supplemental material in Ref. [70], the eigenvalues of Q_φ are linear proportional to the torque M_z the corresponding eigenstate $\vec{u}_\varphi^{(i)}$ exerts onto the target:

$$M_z[\vec{u}^{(i)}] \equiv \int_{\mathcal{C}}[\vec{m}_\perp(\vec{c}) \times \vec{n}(\vec{c})|\partial_{\vec{n}}\psi(\vec{c})|^2]_z ds = 2\tau_\varphi^{(i)}, \tag{4.3}$$

where the integral is taken along the target's boundary described by the curve $\mathcal{C}$ and parameterized by $\vec{c}$. The expression $\vec{n}(\vec{c})|\partial_{\vec{n}}\psi(\vec{c})|^2$ describes the normal force at every point of the boundary exercised by the electric field ψ and $\vec{m}_\perp(\vec{c})$ is the lever (the part of the distance from the boundary to the target's center of mass that is normal to $\vec{n}$). Thus, Eq. (4.3) directly connects the eigenvalues of Q_φ, $\tau_\varphi^{(i)}$, with the torque the corresponding eigenstate $\vec{u}_\varphi^{(i)}$ transfers onto the target. We now inject

the eigenstate of Q_φ with the largest eigenvalues $\tau_\varphi^{(i)}$ through the antennas into the waveguide and measure the electric field, see Fig. 4.2(a). We can clearly see that the wave focuses onto the target's corners, where the lever is maximal and thereby applying the largest torque. In analogy to Fig. 4.2(a), we show in Fig. 4.2(c) the eigenstate of Q_φ with the largest eigenvalue for a square target embedded inside randomly distributed scatterers. Even for such a multiply scattering system, the resulting wave state focuses onto one corner of the square, thus applying a well-defined torque onto it. For comparison, we show in Fig. 4.2(d) the eigenstate with a small eigenvalue where we can see that the wave's intensity is negligibly small at the target's boundaries which is equivalent to applying no torque onto it.

One can observe in Fig. 4.2(a) that the displayed eigenstate exerts not only a torque, but also a force that moves the target in a certain direction. If one is interested in rotating the target without moving its center of mass, one can choose two eigenstates $\vec{u}_\varphi^{(1)}$ and $\vec{u}_\varphi^{(2)}$ of Q_φ that both apply a high torque to the target in the same direction, but whose linear momentum transfer has opposite signs. In Fig. 4.2(b) we can see a wave state resulting from a superposition of such two states, i.e., $\vec{s} = \vec{u}_\varphi^{(1)} + \vec{u}_\varphi^{(2)}$, for which the linear momentum transfer disappears by focusing onto both of the opposite corners of the target.

In a next step we investigate the GWS-operator where the parameter α is the radius R of a metallic circular scatterer. With Eq. (4.2) we can find again a relation between the eigenvalues of Q_R, $\tau_R^{(i)}$, and a meaningful physical quantity. To be more precise, we can show that the eigenvalues $\tau_R^{(i)}$ are linear proportional to the radiation pressure P the corresponding eigenstate $\vec{u}_R^{(i)}$ applies to the target:

$$P[\vec{u}_R^{(i)}] \equiv \int_0^{2\pi} |\partial_\rho \psi(\rho = R)|^2 d\varphi = -2\tau_R^{(i)}/R, \qquad (4.4)$$

where the integral is taken along the boundary of the circular scatterer with radius R and ψ is the electric field distribution of the corresponding eigenstate $\vec{u}_R^{(i)}$. In other words, the eigenstates $\vec{u}_R^{(i)}$ apply a well-defined radiation pressure P to the dielectric target scatterer such that the radiation pressure can be maximized by injecting the eigenstate with the largest eigenvalues into the system. The experimentally measured eigenstate with the largest eigenvalue can be seen in Fig. 4.3(a), where the circular metallic scatterer is surrounded by randomly placed Teflon scatterers. We can clearly see that the state has a strong intensity build-up on all sides of the scatterer. In order to emphasize the ability of applying a large pressure onto a target, we shown in Fig. 4.3(b) an eigenstate with a small eigenvalue which clearly avoids the target.

The next property of a target that we want to investigate now is the dielectric constant ε. We find that the corresponding GWS-operator Q_ε yields eigenstates $\vec{u}_\varepsilon^{(i)}$ whose eigenvalues $\tau_\varepsilon^{(i)}$ are proportional to the integrated intensity I of the wave
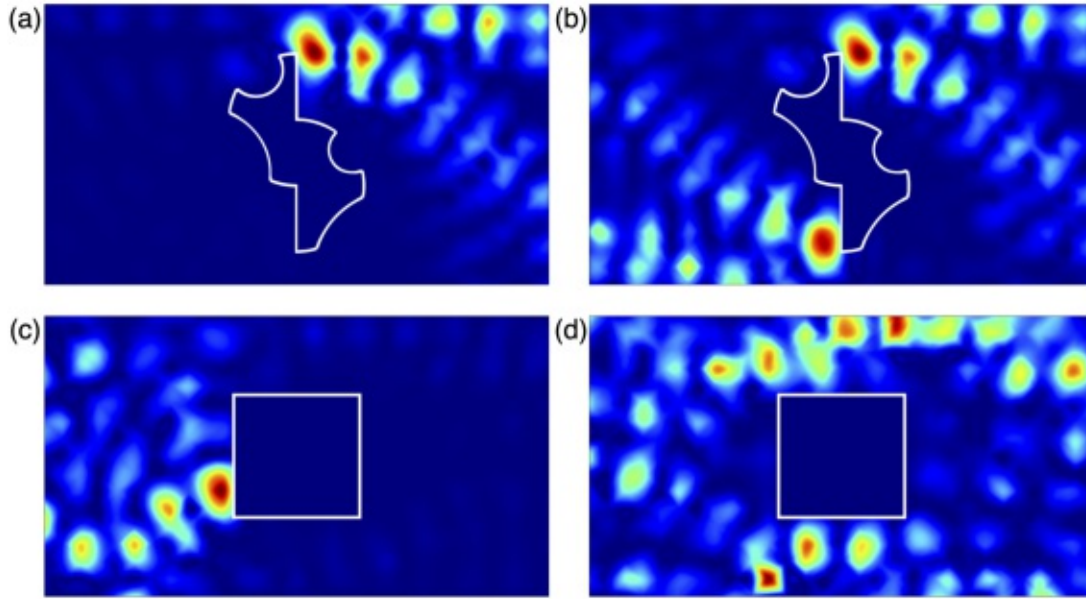
Fig 4.2: Intensity of the electric field for eigenstates of Q_φ for a metallic target (white outline) for (a,b) an asymmetric target in an empty waveguide and for (c,d) a square target in a waveguide filled with randomly placed scatterers. The region displayed here corresponds to the red-shaded area in Fig. 4.1. (a) Intensity of the eigenstate corresponding to the largest eigenvalue $\tau_\varphi^{(\mathrm{max})}$ showing a focus on the point of maximal lever, thus transferring the most torque. (b) Intensity of a superposition of the eigenstates with the two largest eigenvalues, that transfers only angular, but no linear momentum to the target. The corresponding intensity builds up on both of the most protruding parts of the target. (c,d) For a metallic square target inside the disordered waveguide, we compare the eigenstates with the (c) largest eigenvalue $|\tau_\varphi^{(\mathrm{max})}| \approx 5.85$ to an eigenstate that has a (d) small eigenvalue $|\tau_\varphi^{(\mathrm{small})}| \approx 0.2$.

field inside the target. Specifically, we find

$$I[\vec{u}_\varepsilon^{(i)}] \equiv \int |\psi(x,y)|^2 dA = 2\tau_\varepsilon^{(i)}/k_0^2, \tag{4.5}$$

where the integral domain A is the area of our target scatterer, for which ε is changed in the differentiation of $Q_\varepsilon = -\mathrm{i}S^{-1}\partial S/\partial \varepsilon$ and ψ is the electric field distribution of the corresponding eigenstate $\vec{u}_\varepsilon^{(i)}$. Equation (4.5) tells us that if we want to maximize the intensity of a wave inside a target, we can just inject eigenstates of Q_ε into the system with large eigenvalues. Transferring this idea to our microwave experiment, we implement an effective change in the dielectric constant necessary to calculate Q_ε (from $\varepsilon = 1.4884$ to 1.7689 to 2.0736) by varying the height (from $h = 4$ to 6 to 8 mm) of the target Teflon cylinder with radius
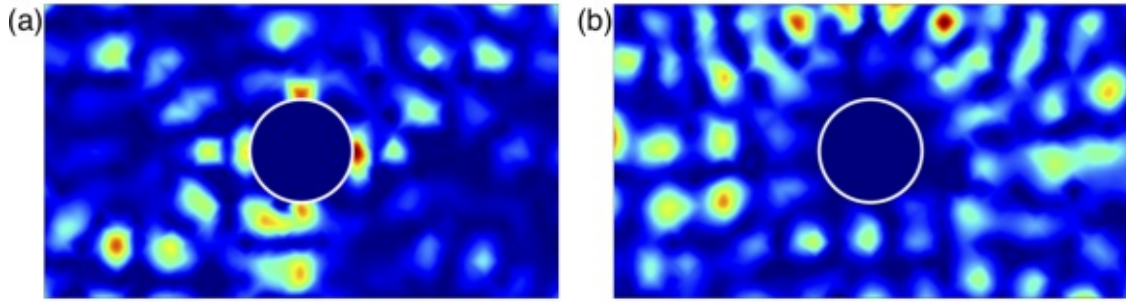
Fig 4.3: (a) Intensity distribution of a scattering state obtained by injecting the eigenvector of Q_R with the largest eigenvalues $|\tau_R^{(\text{max})}| \approx 709$ into the waveguide showing a strong focus on the boundaries of the target (radius $R = 14\,\text{mm}$). (b) Intensity distribution corresponding to an eigenstate of Q_R with a small eigenvalue $|\tau_R^{(\text{small})}| \approx 86$. The measured experimental data verify our prediction that we can tune the degree of pressure applied to the target by choosing eigenstates with different eigenvalues.

$R = 3.75\,\text{mm}$. In Fig. 4.4(a) we display the intensity distribution corresponding to the injection of the eigenstate $\vec{u}_\varepsilon^{(\text{max})}$ with the largest eigenvalue which shows a strong intensity build-up inside the chosen target. Injecting, in turn, an eigenstate with a small eigenvalue [see Fig. 4.4(b)] yields a wave distribution which clearly avoids the target – in perfect agreement to our theory.
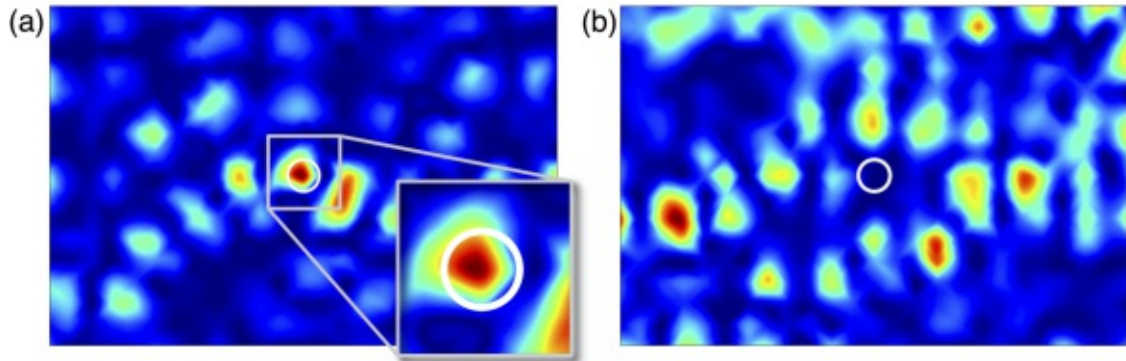
Fig 4.4: (a) Intensity distribution of the eigenstate of Q_ε with the largest eigenvalue $|\tau_\varepsilon^{(\text{max})}| \approx 1.96$ showing a clear intensity build-up inside the circular target. (b) Intensity distribution of an eigenstate corresponding to a small eigenvalue $|\tau_\varepsilon^{(\text{small})}| \approx 0.46$ showing that the wave clearly avoids the target.

In a last step we consider the GWS-operator we obtain when the parameter α is the position of a target, i.e., the corresponding eigenvalues have the dimension of

a momentum. For a metallic target with radius R, the result reads

$$F[\vec{u}_{\hat{\vec{n}}}^{(i)}] \equiv \hat{\vec{n}} \cdot \int_0^{2\pi} \begin{pmatrix} \cos\varphi \\ \sin\varphi \end{pmatrix} |\partial_\rho \psi(\rho = R)|^2 d\varphi = -\frac{2\tau_{\hat{\vec{n}}}^{(i)}}{R}, \tag{4.6}$$

where the direction of the shift and the corresponding momentum transfer is parameterized by the unit vector $\hat{\vec{n}}$ and the integral is performed along the boundary of the circular target. The symbol F is chosen since in the stationary case the momentum transfer is equal to the average force. In practice this means that we are able to find states that receive a well-defined momentum shift when spatially moving one scatterer in a certain direction $\hat{\vec{n}}$. Until now we only consider the case where we have access to the full scattering matrix S, however, it is experimentally very challenging to measure the entire scattering matrix. We show now that the GWS-concept, in particular the operator $Q_{\hat{\vec{n}}}$, works also for the case where we have only access to parts of the scattering matrix [69]. Specifically, we consider the same microwave setup as shown in Fig. 4.1 but now at an operation frequency of 15.5 GHz where 10 transverse lead modes can propagate that can be controlled with 10 antennas placed in the input lead. For this experiment, we restrict ourselves to the measurement of the 10×10 transmission matrix t and consider the case where we shift the metallic target scatterer in transverse direction, i.e., $\hat{\vec{n}} = y$. In analogy to the time-delay operator Q_ω, we use now its non-Hermitian counterpart $q_y = -it^{-1}\partial t/\partial y$ involving only the transmission matrix t. In Fig. 4.5(a) we can see the intensity distribution of the scattering states associated to the eigenstates with the three largest eigenvalues. The displayed intensity profiles demonstrate clearly that the states with the largest eigenvalues show a strong intensity build up at one side of the target, thus applying a large momentum in y-direction onto it. The eigenstates with the smallest eigenvalues, in turn, produce intensity patterns with negligible intensity in the vicinity of the target, see Fig. 4.5(b). Since the construction of the operator q_y involves only the transmission matrix, its complex eigenvalues no longer correspond directly to the transferred momentum in Eq. (4.6). However, there is still a strong correlation between these two quantities as shown in the supplemental material of Ref. [69]. For the case of singular transmission matrices, where the ordinary inverse of t cannot be calculated anymore, we can again apply the procedure described in appendix A.4 to still calculate the operator $\tilde{q}_y$.

The relations between the eigenvalues $\tau_\alpha^{(i)}$ and the physical quantity they are connected to in Eqs. (4.3), (4.4) and (4.6) are all derived for metallic targets. We show in the supplementary material of Ref. [70] that similar relations can also be derived for dielectric targets, which are still strictly linear.

We expect that our GWS-approach presented in this chapter can be particularly useful for the community of optical micromanipulation. The key idea in that field is that the field pattern of laser beams creates forces at the position of the target that

can be used for very different purposes such as cellular manipulation [128, 129], fluid dynamics [130], microrobotics [131] and for tests of fundamental physics [132, 133]. A critical challenge, especially for applications in biology, stems from the fact that the target is often embedded inside complex media (e.g., tissue) or that the target is arbitrarily shaped. With our GWS-concept we can overcome both limitations, i.e., we can micromanipulate an arbitrarily shaped target which can also be embedded in a disordered environment. Thus, we expect that our work may serve as a guide-post towards a new generation of micromanipulation experiments based on wavefront shaping techniques.
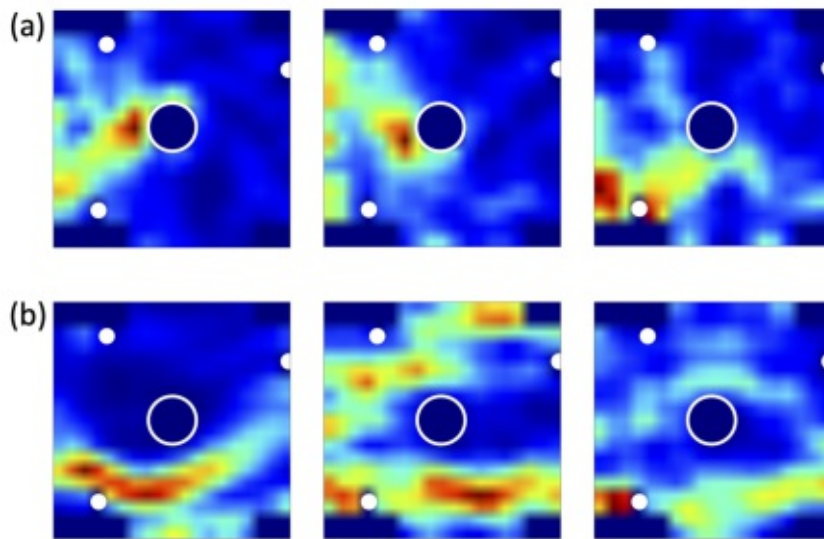
Fig 4.5: (a) Intensity distributions corresponding to eigenstates of q_y with the three largest eigenvalues $|\tau_y^{(i)}| \approx 96.9, 81.6$ and 66.9 showing a clear intensity build-up at one side of the metallic scatterer resulting in a large momentum transfer onto it. (b) Intensity distributions corresponding to the eigenstates with the three smallest eigenvalues $|\tau_y^{(i)}| \approx 1.9, 2.1$ and 6.0 which clearly avoid the scatterer to transfer the least amount of momentum onto it.

In the last chapter of this thesis we introduce the idea of a random anti-laser, which is the time-reversed process of a random laser. This concept combines both core topics of this thesis – disorder and absorption – in an elegant way allowing us to perfectly absorb an incoming wave through a lossy element embedded in a complex scattering environment.

Chapter 5

Random anti-lasing through coherent perfect absorption[9]

One of the most important inventions in modern physics is that of the laser. In its simplest form, a laser consists of a gain medium that is placed inside a resonator. An incident light beam gets trapped inside the resonator and gets amplified each time it passes the gain material. At some specific gain value (lasing threshold), the medium starts to emit coherent radiation without sending in light from the outside. In the framework of scattering theory, this scenario can be described as follows: in systems without gain and loss, the scattering matrix S features poles and zeros in the extended complex plane of frequency ν. Poles are located in the lower half $[\mathrm{Im}(\nu) < 0]$ and zeros in the upper half $[\mathrm{Im}(\nu) > 0]$ of the complex plane, symmetrically around the real axis. Adding gain to the system moves the poles up towards the real ν-axis until one pole hits it. At this specific frequency ν, the laser starts lasing. Also the opposite is possible: adding loss to the system drags the zeros down until one reaches the real axis. At this frequency and absorption strength, incoming light gets perfectly absorbed, resulting in a so-called coherent perfect absorber (CPA) [3, 4, 134, 135].

Such coherent perfect absorbers can be seen as the time-reversed process of a laser and have been experimentally realized in several setups [4, 135–142], with the notable exception of a CPA in a disordered medium. Such a "random CPA" would be the time-reverse of a "random laser" [40, 71], in which light is resonantly enhanced by multiple scattering inside a disorder. Realizing such a random CPA is challenging because the wavefront emitted by a random laser is spatially complex and requires the time-reversing of this light field in all its degrees of freedom. Here, we present the first experimental realization of such a random CPA (or random anti-laser) in a microwave waveguide, similar to the setup used in the last chapters.

---

[9] The results presented in this section were achieved in collaboration with my colleagues Kevin Pichler, Matthias Kühmayer, Philipp Ambichl, and Ulrich Kuhl, Julian Böhm from the Université Côte d'Azur. Kevin Pichler carried out the experiment that was designed by Julian Böhm under the supervision of Ulrich Kuhl. Matthias Kühmayer performed the numerical tasks whereas the theory was developed by Philipp Ambichl, Matthias Kühmayer, Stefan Rotter and myself. The text and the figures partially go back to our joint publication [7].

The system in which we investigate the random CPA is a microwave waveguide as shown in Fig. 5.1. The operation frequency between 6 GHz and 7.5 GHz allows four transverse modes to propagate in the waveguide. In order to control all degrees of freedom of the wave – which is necessary for the realization of a CPA – we place four antennas on each end of the waveguide. Inside the waveguide we randomly place 60 cylindrical Teflon scatterers to simulate the disorder. In the middle of the scattering region we insert an antenna, which provides a localized and very strong loss channel. In order to change the degree of loss in the system, the length of the absorbing antenna inside the waveguide can be changed. The goal of the experiment is to find the correct absorption strength of the central antenna and the correct frequency and shape of the wavefront (in amplitude and phase) injected through the eight antennas such that the incident wave scatters in the disorder to get finally perfectly absorbed by the central antenna without any back-reflections.
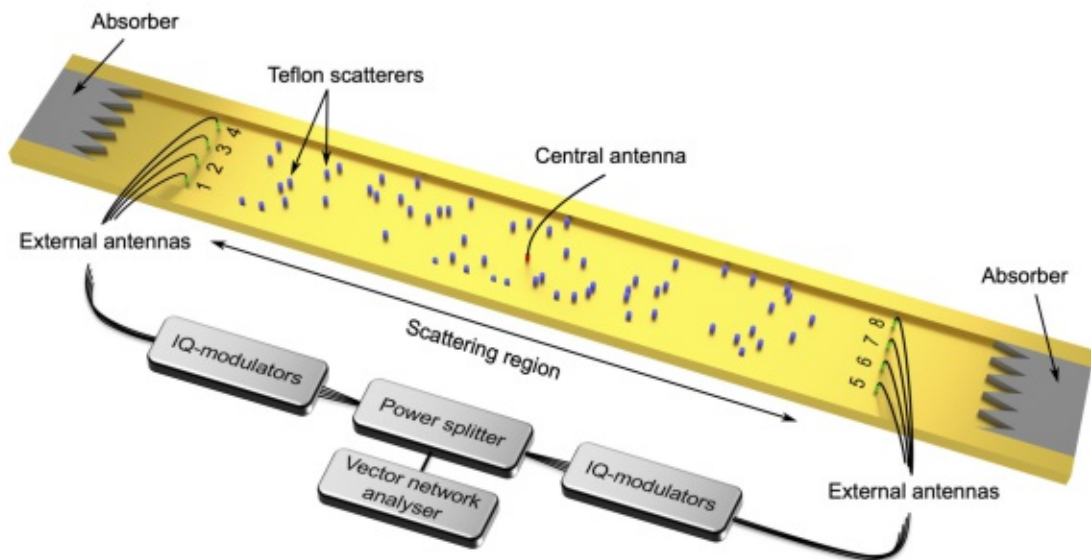
Fig 5.1: Microwave waveguide where waves can be injected through the eight antennas (four on each side) connected to IQ-modulators to independently control amplitude and phase of each antenna signal. The waveguide has a width of $10\,$cm such that at an operation frequency between 6 GHz and 7.5 GHz four transverse modes can propagate. Absorbers are placed at the ends of the waveguide to avoid back-reflections. The central scattering region contains a disorder formed by 60 randomly placed Teflon scatterers with radius $r = 2.55\,$mm. In the middle of the scattering region a monopole antenna is inserted through the top plate of the waveguide (not shown). This central antenna introduces loss into the waveguide that can be tuned by varying the length of the antenna inside the waveguide. This setup allows for the measurement of the scattering matrix S of the system by measuring the field in the space between the scattering region and the external antennas using a movable antenna (not shown).

The central quantity that allows us to find the correct wavefront for a CPA is the scattering matrix S. A random CPA-state would be an eigenstate of the scattering matrix S with eigenvalue $\tau_{\mathrm{CPA}} = 0$ such that $S\vec{u}_{\mathrm{CPA}} = \vec{0}$, where $\vec{u}_{\mathrm{CPA}}$ is the incoming radiation field and the empty $\vec{0}$ field is the outgoing one. In order to obtain the CPA-state $\vec{u}_{\mathrm{CPA}}$ we measure the scattering matrix S of the system in a frequency interval broad enough to contain many zeros of S and for a number of loss values of the central absorbing antenna that are strong enough to drag the zeros with the smallest imaginary parts down to the real ν-axis. In a next step, we evaluate the eigenvalues of all these different scattering matrices S and identify the parameter configuration for which we get the smallest eigenvalue. Finally, we adjust the frequency and the absorption strength to the point at which CPA occurs and inject the eigenstate corresponding to this small eigenvalue into the system and evaluate the degree of absorption.

Following the above protocol, we end up with a scattering state that gets absorbed by 99.78%. In Fig. 5.2(a) we show the ratio between the outgoing and the incoming intensity $I_{\mathrm{out}}/I_{\mathrm{in}}$ of one specific CPA-state as a function of the frequency ν (blue line). We can see a very pronounced minimum at the frequency where the CPA-state was evaluated, which is a first revealing hallmark of a CPA.

In the following we perform a number of tests to make sure that we have, indeed, realized a disordered CPA rather than a coherent enhancement of absorption (CEA) [5] or one of the previously employed focusing schemes [36, 143–145]. First of all, since we expect our CPA-state to be mainly absorbed by the central absorbing antenna, the time-reversed state should be a state that features no back-reflections when being injected through the central absorbing antenna. Such a time-reversal is easy to implement in our setup and we find indeed, that the signal injected through the central absorbing antenna shows no reflections back into the antenna at the target frequency, see Fig. 5.2(a) red dashed line. The observed dip is slightly shifted (by 0.025%) with respect to the frequency of the CPA found before because of the weak global absorption caused primarily by the absorption in the metallic plates on the top and bottom of the waveguide.

In a second test, we study how the CPA minimum changes as a function of the coupling strength of the central antenna. As described above, a CPA requires a zero of the scattering matrix S to be located exactly at the real frequency axis. Increasing or decreasing the coupling strength of the antenna would move this zero away from the real axis such that we should find a reduced amount of absorption of the CPA-state not only when we reduce the coupling strength but even if we increase it. The coupling strength of the central antenna can easily be changed by varying the length of the central antenna inside the waveguide. We, indeed, find that not only a smaller, but also a larger amount of loss (i.e., the central antenna reaching deeper into the waveguide) leads to a dramatic decrease of the CPA minimum, see Fig. 5.2(b). We find that an antenna extending 7 mm into the waveguide yields the optimal CPA-state.
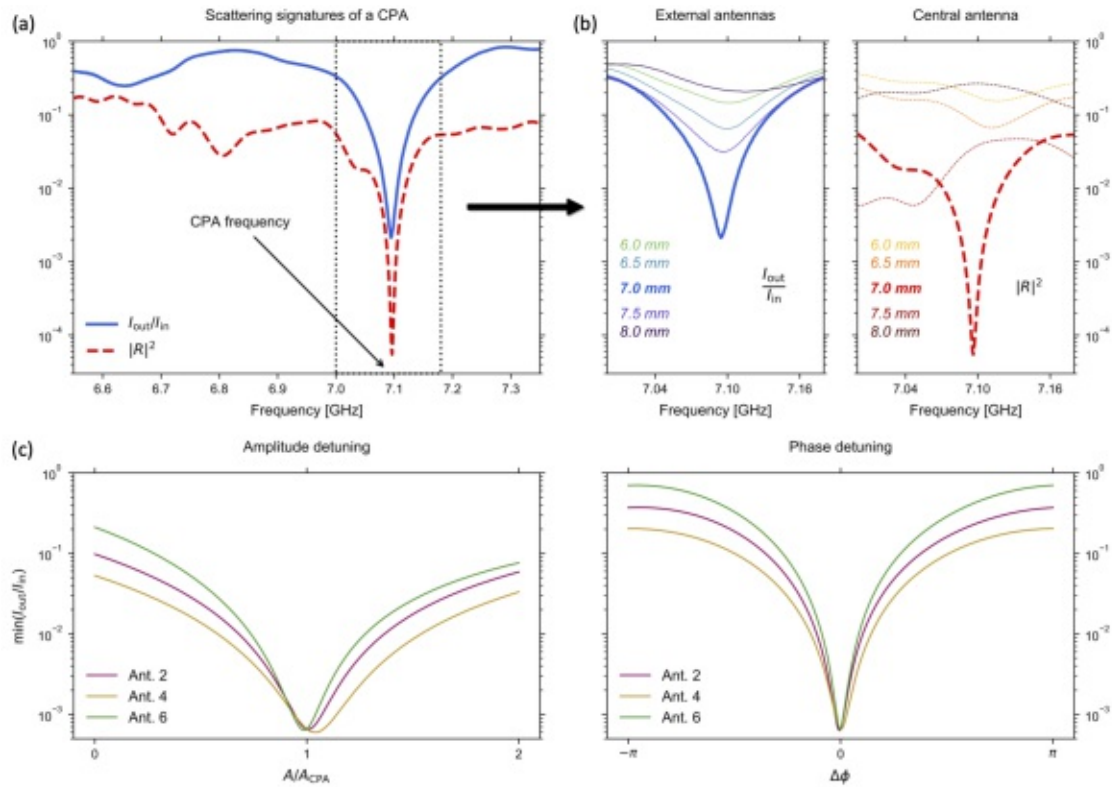
Fig 5.2: (a) Ratio $I_{\mathrm{out}}/I_{\mathrm{in}}$ of a CPA-state as a function of the frequency ν (blue line), where I_{in} is the incoming intensity injected through the external antennas (measured in the space between the external antennas and the disordered region) and I_{out} is the corresponding outgoing intensity. The red dashed line is the reflection signal $|R|^2$ measured when the microwave signal is injected through the central antenna. Both curves show a pronounced minimum at the CPA-frequency around 7.1 GHz that depends very sensitively on the frequency. (b) Ratio $I_{\mathrm{out}}/I_{\mathrm{in}}$ (left) and reflection coefficient $|R|^2$ (right) as a function of the frequency ν for different lengths of the central absorbing antenna. Starting with an antenna length of 6 mm, the CPA absorption dip in both $I_{\mathrm{out}}/I_{\mathrm{in}}$ and $|R|^2$ first deepens when increasing the antenna length until a minimum is reached for an antenna length of 7 mm. Increasing the loss of the antenna by further increasing its length results in less absorption efficiency and a larger reflection signal. (c) Sensitivity of the CPA minimum on detunings of the amplitude A (left) and phase ϕ (right) of antenna 2, 4 or 6 while the signals at all other antennas are injected as required for the CPA-state (amplitude A_{CPA} and phase ϕ_{CPA}). We can see that the absorption efficiency of the CPA-state is very sensitive to changes of the CPA configuration.

In a next test we study the sensitivity of the CPA with respect to changes in the input wavefront. Specifically, we show what happens when either the amplitude or the phase of just one of the eight input antennas is detuned away from the perfect

CPA-state $\vec{u}_{\mathrm{CPA}}$. In Fig. 5.2(c) we show that the CPA dip (i.e., the minimum of the ratio $I_{\mathrm{out}}/I_{\mathrm{in}}$) gets dramatically shifted upwards by factors up to approximately 10^3 when the phase (right panel) or the amplitude (left panel) of antenna 2, 4 or 6 are detuned.

In a fourth test we study the wave function of the CPA-state around the absorbing antenna, since we expect that the corresponding flux as given by the Poynting vector $\vec{S}$ is solely pointing inwards close to the antenna. The field is, however, experimentally not accessible in the direct vicinity of the central antenna, such that we reconstruct the entire scattering system numerically with a finite-element code (for details on the simulation see methods section in Ref. [70]). We find that the numerically simulated CPA wave function has a 95.6% correlation with the experimentally realized one such that we can use the simulated CPA-state to study its field in the vicinity of the absorbing antenna, see Fig. 5.3(a). We find, indeed, that the corresponding flux pattern is directed solely towards the absorbing antenna, see inset in Fig. 5.3(a).

In a last test we verify that the transmission into the central absorbing antenna has a maximum at the CPA-frequency, as shown in Fig. 5.3(b). The CPA-state gets thus mostly absorbed by the central antenna and is only weakly affected by the global loss in the waveguide.

To summarize, we present the first experimental realization of a random CPA (or random anti-laser), which provides the proof-of-principle that coherent perfect absorption can also be realized in disordered structures. The high sensitivity of the CPA-state with respect to the incident wavefront can be exploited, e.g., for designing tunable absorbers whose degree of absorption can be controlled by a phase-detuning of the incident wave. Our approach requires only the knowledge of the scattering matrix of the system – no information of the inner structure of the medium is necessary. We expect that our results serve as a bridge between the two communities of wavefront shaping and non-Hermitian physics.
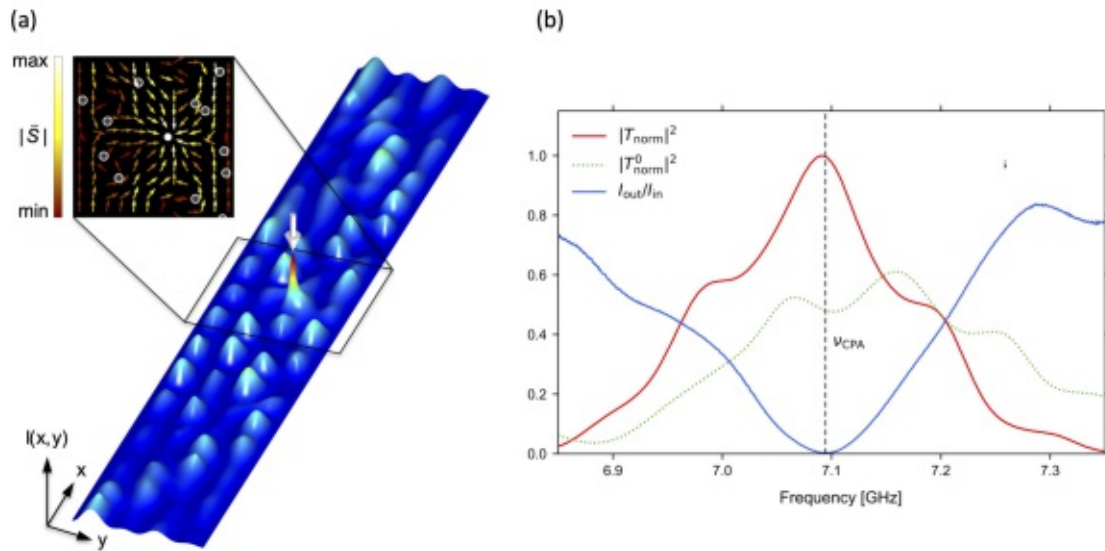
Fig 5.3: (a) Simulated intensity of the CPA-state in the disordered waveguide. The white arrow marks the position of the central absorbing antenna. In the vicinity of the antenna the time-averaged Poynting vector $\vec{S} \propto (i\psi(\partial/\partial_x\psi)^*, i\psi(\partial/\partial_y\psi)^*, 0)^T$ (see inset) only has inward pointing components, where the semi-transparent circles in the inset mark the scatterers and the filled white circle represents the central absorbing antenna. (b) Measured transmission of a CPA-state into the absorbing antenna. Close to the CPA-frequency ν_{CPA}, where the absorption of the CPA-state is most efficient, the transmission into the absorbing antenna has its maximum. The plot compares the normalized transmission $|T_{\mathrm{norm}}|^2$ (normalized with respect to its maximum within the measured interval) into the absorbing antenna with the ration $I_{\mathrm{out}}/I_{\mathrm{in}}$. As reference measurement we also investigate the transmission T^0_{norm} into the absorbing antenna of the same CPA-state but in the absence of any scatterers in the waveguide. Since the CPA-state is customized for each specific scatterer configuration, the transmission into the absorbing antenna is strongly reduced when the scatterers are removed.

Summary and outlook

As we show in this thesis, we can overcome the detrimental effects of loss and disorder and take advantage of them either by designing the corresponding loss and disorder landscape in a system or by shaping the incident wavefront.

We first introduce the concept of constant-intensity waves which are waves that get perfectly transmitted without any back-reflections or intensity variations even in the case of localizing media if a proper gain and loss distribution is added. We study the frequency stability of such constant-intensity waves and demonstrate how to design unidirectionally invisible structures by engineering their gain and loss distribution. In order to do so, we tune the transmission phase of a constant-intensity wave to match exactly the phase a wave would accumulate in a uniform structure. Extending this concept to three dimensions would result in an invisibility cloak, which would not guide the light around a given object (as in traditional cloaks) but rather right through the object, without, however, distorting the wave at inhomogeneities. We show that the general frequency stability of constant-intensity waves even allows for a pulse to propagate without diffraction through a disordered constant-intensity structure. We transfer the idea of constant-intensity waves to discrete systems allowing us to implement them in an acoustic setup. Specifically, we present the first experimental realization of constant-pressure waves in a one-dimensional disordered acoustic waveguide, thus nicely demonstrating our concept. Generalizing the idea of constant-intensity waves also allows us to create scattering states with any predetermined intensity profile rather than a constant one. We expect this method to fall on a fertile ground since controlling a wave's intensity profile is an important task in many fields of wave physics. Furthermore, we show that constant-intensity waves can be extended to full two-dimensional systems allowing us to study a much broader class of structures.

In the context of wavefront shaping, we work with the Wigner-Smith time-delay operator and its eigenstates, the so-called principal modes. They have the remarkable property that their output pattern is robust to first order against changes of the frequency. Some of these principal modes have the counterintuitive property of having a particle-like wave function. We successfully implement such particle-like states in a microwave cavity showing that they can be used for efficient, focused and robust transmission through complex environments. Moreover, we numerically show how to address individual branches of the complex propagation pattern evolving when waves propagate through a correlated disorder. This separation works by injecting time-delay eigenstates into the system since different branches can be asso-

ciated to different time-delays. We expect that our work will soon be implemented in the experiment where branched flow was recently observed.

The functional principle of the Wigner-Smith time-delay operator involving a frequency derivative of the scattering matrix can be generalized to a whole new operator class that involves the derivative of the scattering matrix with respect to any parameter of the scattering system. Choosing different parameters, we demonstrate in a microwave experiment that these new operators allow us to create wave states that transfer onto a target a well-defined momentum, pressure or torque as well as to achieve a focus inside the target. The target can be arbitrarily shaped and can even be surrounded by a strongly disordered environment. We are confident that the results presented here can be particularly useful for optical micromanipulation where manipulating a target with light fields is essential. We envision, for example, developing a new concept for the so-called optical tweezer that allows us to navigate a movable object along a predetermined path through a disordered environment by directing well-defined wavefronts onto the medium from the outside. Using a similar concept, one could also set up a protocol for reconstructing images of objects which are hidden inside a strongly disordered medium. While imaging techniques are usually limited by the scattering strength of the surrounding medium, our concept has the potential to work even in the strongly scattering regime.

In the last part of this thesis we show that carefully shaping the incident wavefront impinging onto a disordered lossy structure can lead to perfect absorption of the wave's incoming flux. This phenomenon of coherent perfect absorption in disordered media is studied for the first time in the experiment using a microwave setup. Our approach requires only the knowledge of the scattering matrix – no information on the inner structure of the medium is necessary. Our work can be relevant for practical applications, including perfect focusing of electromagnetic signals and sound fields in complex environments, such as in office spaces or in biological tissue.

We are confident that with the results presented in this thesis we could contribute to changing the prevailing view that loss and disorder are solely detrimental ingredients of photonic structures that have to be stayed away from. Loss and disorder can indeed be useful tools for certain tasks and they still have considerable potential for innovation in photonics.

Appendix

A.1 Derivation of the Helmholtz equation

In the following we derive the equations describing the time-harmonic electric field of a light wave propagating in an inhomogeneous, linear and isotropic medium. We start from the full Maxwell's equation (in SI units)

$$\vec{\nabla} \cdot \vec{D}(\vec{r}, t) = \rho_f(\vec{r}, t), \tag{A.1}$$

$$\vec{\nabla} \cdot \vec{B}(\vec{r}, t) = 0, \tag{A.2}$$

$$\vec{\nabla} \times \vec{E}(\vec{r}, t) = -\frac{\partial}{\partial t}\vec{B}(\vec{r}, t), \tag{A.3}$$

$$\vec{\nabla} \times \vec{H}(\vec{r}, t) = \vec{j}_f(\vec{r}, t) + \frac{\partial}{\partial t}\vec{D}(\vec{r}, t), \tag{A.4}$$

where $\vec{D}$ is the electric flux density (or displacement field), $\vec{E}$ the electric field strength, $\vec{B}$ the magnetic flux density, $\vec{H}$ the magnetic field strength, $\vec{j}_f$ the free current density, ρ_f the free charge density and $\vec{r} = (x, y, z)^T$ the position vector. First we assume that there are no free charges ($\rho_f = 0$) and no free currents ($\vec{j}_f = \vec{0}$). Assuming furthermore that the medium is linear, the relation between $\vec{D}$ and $\vec{E}$, and $\vec{B}$ and $\vec{H}$ is given by:

$$\vec{D}(\vec{r}, t) = \varepsilon_0 \boldsymbol{\varepsilon_r}(\vec{r}, t)\vec{E}(\vec{r}, t) = \varepsilon_0 \begin{pmatrix} \varepsilon_{r,11}(\vec{r}, t) & \varepsilon_{r,12}(\vec{r}, t) & \varepsilon_{r,13}(\vec{r}, t) \\ \varepsilon_{r,21}(\vec{r}, t) & \varepsilon_{r,22}(\vec{r}, t) & \varepsilon_{r,23}(\vec{r}, t) \\ \varepsilon_{r,31}(\vec{r}, t) & \varepsilon_{r,32}(\vec{r}, t) & \varepsilon_{r,33}(\vec{r}, t) \end{pmatrix} \vec{E}(\vec{r}, t), \tag{A.5}$$

$$\vec{B}(\vec{r}, t) = \mu_0 \boldsymbol{\mu_r}(\vec{r}, t)\vec{H}(\vec{r}, t) = \mu_0 \begin{pmatrix} \mu_{r,11}(\vec{r}, t) & \mu_{r,12}(\vec{r}, t) & \mu_{r,13}(\vec{r}, t) \\ \mu_{r,21}(\vec{r}, t) & \mu_{r,22}(\vec{r}, t) & \mu_{r,23}(\vec{r}, t) \\ \mu_{r,31}(\vec{r}, t) & \mu_{r,32}(\vec{r}, t) & \mu_{r,33}(\vec{r}, t) \end{pmatrix} \vec{H}(\vec{r}, t), \tag{A.6}$$

where $\boldsymbol{\varepsilon_r}(\vec{r}, t)$ is the relative permittivity tensor, $\boldsymbol{\mu_r}(\vec{r}, t)$ the relative permeability tensor, ε_0 the (scalar) vacuum permittivity and μ_0 the (scalar) vacuum permeability. In the following we only consider non-magnetic materials, i.e., $\boldsymbol{\mu_r}(\vec{r}, t) = \mathbb{1}$, with a static relative permittivity, i.e., $\boldsymbol{\varepsilon_r}(\vec{r}, t) = \boldsymbol{\varepsilon_r}(\vec{r})$. Depending on their permittivity tensors, we can classify materials into four groups: structures where the permittivity tensor is diagonal (but not proportional to the unit matrix) with three (two)

different elements are called biaxial (uniaxial) anisotropic structures, whereas structures without any symmetry are simply called anisotropic. In this thesis we only consider isotropic media, where the permittivity tensor is proportional to the unit matrix such that the permittivity tensor can be replaced by a (position-dependent) scalar, i.e., $\vec{D}(\vec{r}, t) = \varepsilon_0 \varepsilon_r(\vec{r}, t) \vec{E}(\vec{r}, t)$.

Applying the curl operator onto Eq. (A.3) and using the vector calculus identity $\vec{\nabla} \times (\vec{\nabla} \times \vec{A}) = \vec{\nabla}(\vec{\nabla} \cdot \vec{A}) - \vec{\nabla}^2 \vec{A}$, we get

$$\vec{\nabla} \times \left[\vec{\nabla} \times \vec{E}(\vec{r}, t) \right] = \vec{\nabla} \left[\vec{\nabla} \cdot \vec{E}(\vec{r}, t) \right] - \vec{\nabla}^2 \vec{E}(\vec{r}, t)$$

$$= -\frac{\partial}{\partial t} \vec{\nabla} \times \vec{B}(\vec{r}, t) = -\mu_0 \frac{\partial}{\partial t} \vec{\nabla} \times \vec{H}(\vec{r}, t), \tag{A.7}$$

where we used $\vec{B} = \mu_0 \vec{H}$. Using Eq. (A.1) and $\vec{D}(\vec{r}, t) = \varepsilon_0 \varepsilon_r(\vec{r}) \vec{E}(\vec{r}, t)$, we can derive the following expression:

$$\vec{\nabla} \cdot \vec{E}(\vec{r}, t) = -\frac{1}{\varepsilon_r(\vec{r})} \vec{\nabla} \varepsilon_r(\vec{r}) \cdot \vec{E}(\vec{r}, t)$$

$$= -\vec{\nabla} \ln[\varepsilon_r(\vec{r})] \cdot \vec{E}(\vec{r}, t). \tag{A.8}$$

Inserting Eq. (A.8) and Eq. (A.4) into Eq. (A.7), we get

$$-\vec{\nabla} \left\{ \vec{\nabla} \ln[\varepsilon_r(\vec{r})] \cdot \vec{E}(\vec{r}, t) \right\} - \vec{\nabla}^2 \vec{E} = -\mu_0 \frac{\partial^2}{\partial t^2} \vec{D}(\vec{r}, t) = -\mu_0 \varepsilon_0 \varepsilon_r(\vec{r}) \frac{\partial^2}{\partial t^2} \vec{E}(\vec{r}, t). \tag{A.9}$$

Assuming a time-harmonic dependence of the electric field with frequency ω_0, i.e., $\vec{E}(\vec{r}, t) = \vec{E}_0(\vec{r}) e^{i\omega_0 t}$, we get the following equation for the (position-dependent) electric field $\vec{E}_0(\vec{r})$:

$$-\vec{\nabla} \left\{ \vec{\nabla} \ln[\varepsilon_r(\vec{r})] \cdot \vec{E}_0(\vec{r}) \right\} - \vec{\nabla}^2 \vec{E}_0 = \frac{\omega_0^2}{c^2} \varepsilon_r(\vec{r}) \vec{E}_0(\vec{r}), \tag{A.10}$$

where we use $c^2 = \frac{1}{\mu_0 \varepsilon_0}$ with c being the speed of light in vacuum. Writing out this vector equation into its components yields

$$\left(\frac{\partial^2}{\partial x^2} + \frac{\partial^2}{\partial y^2} + \frac{\partial^2}{\partial z^2} \right) E_{0,x} \tag{A.11}$$

$$= -\frac{\omega_0^2}{c^2} \varepsilon_r E_{0,x} - \frac{\partial}{\partial x} \left[E_{0,x} \frac{\partial}{\partial x} \ln(\varepsilon_r) + E_{0,y} \frac{\partial}{\partial y} \ln(\varepsilon_r) + E_{0,z} \frac{\partial}{\partial z} \ln(\varepsilon_r) \right],$$

$$\left(\frac{\partial^2}{\partial x^2} + \frac{\partial^2}{\partial y^2} + \frac{\partial^2}{\partial z^2} \right) E_{0,y} \tag{A.12}$$

$$= -\frac{\omega_0^2}{c^2} \varepsilon_r E_{0,y} - \frac{\partial}{\partial y} \left[E_{0,x} \frac{\partial}{\partial x} \ln(\varepsilon_r) + E_{0,y} \frac{\partial}{\partial y} \ln(\varepsilon_r) + E_{0,z} \frac{\partial}{\partial z} \ln(\varepsilon_r) \right],$$

$$\left(\frac{\partial^2}{\partial x^2} + \frac{\partial^2}{\partial y^2} + \frac{\partial^2}{\partial z^2}\right) E_{0,z} \tag{A.13}$$

$$= -\frac{\omega_0^2}{c^2}\varepsilon_r E_{0,z} - \frac{\partial}{\partial z}\left[E_{0,x}\frac{\partial}{\partial x}\ln(\varepsilon_r) + E_{0,y}\frac{\partial}{\partial y}\ln(\varepsilon_r) + E_{0,z}\frac{\partial}{\partial z}\ln(\varepsilon_r)\right],$$

where we skipped all arguments for better readability. In the following we show how these equations simplify for one- and two-dimensional systems.

First consider the case where the relative permittivity (also called dielectric function) shows variations along only one direction (say x) and stays constant in y- and z-direction. Due to this translation invariance in y- and z-direction, all derivatives with respect to y and z vanish. Thus, Eqs. (A.11)-(A.13) turn into

$$\frac{\partial^2}{\partial x^2}E_{0,x} = -\frac{\omega_0^2}{c^2}\varepsilon_r E_{0,x} - \frac{\partial}{\partial x}\left[E_{0,x}\frac{\partial}{\partial x}\ln(\varepsilon_r)\right], \tag{A.14}$$

$$\frac{\partial^2}{\partial x^2}E_{0,y} = -\frac{\omega_0^2}{c^2}\varepsilon_r E_{0,y}, \tag{A.15}$$

$$\frac{\partial^2}{\partial x^2}E_{0,z} = -\frac{\omega_0^2}{c^2}\varepsilon_r E_{0,z}, \tag{A.16}$$

which are three decoupled differential equations for each component of the electric field. Choosing the incident field as, e.g., $\vec{E}_0 = (0, 0, E_{0,z})^T$, the propagation of the z-component of the electric field can easily be calculated with the Helmholtz Eq. (A.16), whereas the x and y components stay zero.

For systems showing variations in two dimension (say x and y), i.e., $\varepsilon_r(\vec{r}) = \varepsilon_r(x, y)$, all derivatives with respect to z vanish. Thus, Eqs. (A.11)-(A.13) turn into

$$\left(\frac{\partial^2}{\partial x^2} + \frac{\partial^2}{\partial y^2}\right) E_{0,x} = -\frac{\omega_0^2}{c^2}\varepsilon_r E_{0,x} - \frac{\partial}{\partial x}\left[E_{0,x}\frac{\partial}{\partial x}\ln(\varepsilon_r) + E_{0,y}\frac{\partial}{\partial y}\ln(\varepsilon_r)\right], \tag{A.17}$$

$$\left(\frac{\partial^2}{\partial x^2} + \frac{\partial^2}{\partial y^2}\right) E_{0,y} = -\frac{\omega_0^2}{c^2}\varepsilon_r E_{0,y} - \frac{\partial}{\partial y}\left[E_{0,x}\frac{\partial}{\partial x}\ln(\varepsilon_r) + E_{0,y}\frac{\partial}{\partial y}\ln(\varepsilon_r)\right], \tag{A.18}$$

$$\left(\frac{\partial^2}{\partial x^2} + \frac{\partial^2}{\partial y^2}\right) E_{0,z} = -\frac{\omega_0^2}{c^2}\varepsilon_r E_{0,z}, \tag{A.19}$$

where Eq. (A.17) and (A.18) are coupled differential equations for the x and y component of the electric field and Eq. (A.19) is a decoupled equation for the z-component. Choosing again the incident field as, $\vec{E}_0 = (0, 0, E_{0,z})^T$, the propagation of the z-component of the electric field can easily be calculated with the Helmholtz Eq. (A.19), whereas the x and y components stay zero.

For systems where the dielectric function shows variations in all three dimensions, Eqs. (A.11)-(A.13) do not decouple anymore such that the full vectorial problem has to be solved.

In this thesis, we only consider one- and two-dimensional systems where we study the out-of-plane component $E_{0,z}$ of the electric field. Labeling this field component as $\psi = E_{0,z}$, using the dispersion relation for electromagnetic waves $\omega_0 = k_0 c$ (with k_0 being the wave number) and substituting the relative permittivity ε_r by the square of the refractive index n, i.e., $n^2 = \varepsilon_r$, we get the following version of the Helmholtz equation used throughout this thesis:

$$\left[\frac{\partial^2}{\partial x^2} + \frac{\partial^2}{\partial y^2} + n^2(x,y)k_0^2 \right] \psi(x,y) = 0, \tag{A.20}$$

derived from Eq. (A.19) for two-dimensional structures and:

$$\left[\frac{\partial^2}{\partial x^2} + n^2(x)k_0^2 \right] \psi(x) = 0, \tag{A.21}$$

derived from Eq. (A.16) for one-dimensional systems.

A.2 Transfer-matrix method

In order to solve the Helmholtz Eq. (A.21) for a one-dimensional structure we can use the transfer-matrix method [146]. This method divides a continuous (complex) refractive index $n(x)$ into a large number N of small slices of width d, assuming that the refractive index is constant within each slice. This allows us to decompose the electric field in the m-th layer with refractive index n_m into two counter-propagating plane waves,

$$\psi_m = E_m e^{ik_0 n_m x} + E'_m e^{-ik_0 n_m x}, \tag{A.22}$$

where E_m and E'_m are the complex amplitudes of the wave traveling to the right and left side, respectively. At the interface between two consecutive layers, these amplitudes have to fulfill the following boundary condition:

$$\begin{pmatrix} 1 & 1 \\ n_m & -n_m \end{pmatrix} \begin{pmatrix} E_m \\ E'_m \end{pmatrix} = \begin{pmatrix} 1 & 1 \\ n_{m+1} & -n_{m+1} \end{pmatrix} \begin{pmatrix} E_{m+1} \\ E'_{m+1} \end{pmatrix}. \tag{A.23}$$

The propagation of the wave within one layer of width d leads to a phase accumulation which can be described by the following matrix:

$$\begin{pmatrix} \tilde{E}_m \\ \tilde{E}'_m \end{pmatrix} = \begin{pmatrix} e^{i\phi_m} & 0 \\ 0 & e^{-i\phi_m} \end{pmatrix} \begin{pmatrix} E_m \\ E'_m \end{pmatrix}, \tag{A.24}$$

where E_m, E'_m denotes the amplitudes at the beginning of the layer, $\tilde{E}_m, \tilde{E}'_m$ the amplitudes at the end of the layer and $\phi_m = k_0 n_m d$ is the accumulated phase. Since both operations (the propagation within one layer as well as the transition from one layer to the next one) can be described by matrices, it is possible to derive the

transfer-matrix M_j, connecting the electric field at the beginning of the structure ($m = 0$) with the electric field in the j-th layer ($m = j$), just by iteratively using matrices in Eq. (A.23) and in Eq. (A.24):

$$\begin{pmatrix} E_j \\ E_j' \end{pmatrix} = \begin{pmatrix} e^{\mathrm{i}\phi_j} & 0 \\ 0 & e^{-\mathrm{i}\phi_j} \end{pmatrix} \begin{pmatrix} 1 & 1 \\ n_j & -n_j \end{pmatrix}^{-1} \begin{pmatrix} 1 & 1 \\ n_{j-1} & -n_{j-1} \end{pmatrix} \tag{A.25}$$

$$\cdots \begin{pmatrix} e^{\mathrm{i}\phi_1} & 0 \\ 0 & e^{-\mathrm{i}\phi_1} \end{pmatrix} \begin{pmatrix} 1 & 1 \\ n_1 & -n_1 \end{pmatrix}^{-1} \begin{pmatrix} 1 & 1 \\ n_0 & -n_0 \end{pmatrix} \begin{pmatrix} E_0 \\ E_0' \end{pmatrix} = \begin{pmatrix} M_{11} & M_{12} \\ M_{21} & M_{22} \end{pmatrix} \begin{pmatrix} E_0 \\ E_0' \end{pmatrix},$$

where M_{xy} are the elements of the matrix M_j. Knowing the electric field at the beginning of the structure, i.e., E_0 and E_0', one can easily calculate the electric field in the entire structure using the transfer-matrices M_j and Eq. (A.22).

On the basis of the transfer-matrix M_{N+1}, i.e., the transfer-matrix connecting the first with the last layer, we can easily calculate the scattering matrix S, connecting incoming with outgoing amplitudes,

$$\begin{pmatrix} E_0' \\ E_{N+1} \end{pmatrix} = \begin{pmatrix} S_{11} & S_{12} \\ S_{21} & S_{22} \end{pmatrix} \begin{pmatrix} E_0 \\ E_{N+1}' \end{pmatrix}, \tag{A.26}$$

with the help of the following relations:

$$S_{11} = -\frac{M_{21}}{M_{22}}, \quad S_{12} = \frac{1}{M_{22}},$$
$$S_{21} = M_{11} - \frac{M_{12}M_{21}}{M_{22}}, \quad S_{22} = \frac{M_{12}}{M_{22}}. \tag{A.27}$$

The elements of the scattering matrix S can be interpreted as following,

$$S = \begin{pmatrix} r & t' \\ t & r' \end{pmatrix}, \tag{A.28}$$

where r, t are the complex reflection and transmission amplitudes for injection from the left-hand side of the structure, and r', t' are the corresponding amplitudes for injection from the right-hand side of the structure (see Chapter 1 details on the scattering matrix).

A.3 Transmission line model and constant-pressure waves[10]

The propagation of sound waves in an acoustic waveguide loaded with a set of discrete inclusions at low frequency, where only one single mode can be excited,

---

[10] The derivation of the transmission line model and the equations for the constant-pressure waves shown in this section partially follow the bachelor thesis of Nikolaus de Zordo that I co-advised [62].

can be described by the transmission line model [86]. The acoustic pressures p_j and volume flows q_j in front of each inclusion are connected by

$$\begin{pmatrix} p_j \\ q_j \end{pmatrix} = \begin{pmatrix} 1 & Z_j \\ 0 & 1 \end{pmatrix} \begin{pmatrix} A_j & B_j \\ C_j & D_j \end{pmatrix} \begin{pmatrix} p_{j+1} \\ q_{j+1} \end{pmatrix}, \tag{A.29}$$

where Z_j is the impedance of the j-th inclusion and $M_j = [A_j, B_j; C_j, D_j]$ is the transfer-matrix connecting inclusion j and $j+1$ (see Fig. A.1).
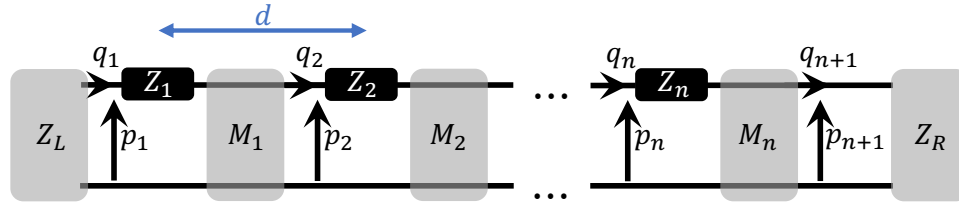

Fig A.1: Schematic of the transmission line model where we consider a one-dimensional chain of n inclusions with acoustic impedances Z_j. The pressures p_j and the volume flows q_j are connected through transfer matrices M_j. The beginning and the end of the system is connected to two semi-infinite leads with impedances Z_L and Z_R.

In the experiment presented in Section 2.3, the transfer-matrix M_j can be built from three sub-matrices representing three segments of one tube section as can be seen in Fig. A.2. These three sections have the length d_1, d_2 and $d - d_1 - d_2$ with corresponding impedances Z_0, Z_2 and Z_0. Our transfer-matrix M_j is then just a multiplication of the partial transfer matrices M_p:

$$M_j = \begin{pmatrix} A_j & B_j \\ C_j & D_j \end{pmatrix} = M_p(Z_0, d_1) M_p(Z_2, d_2) M_p(Z_0, d - d_1 - d_2), \tag{A.30}$$

with

$$M_p(Z, x) = \begin{pmatrix} \cos(k_0 x) & \mathrm{i} Z \sin(k_0 x) \\ \mathrm{i} \sin(k_0 x)/Z & \cos(k_0 x) \end{pmatrix}. \tag{A.31}$$

The goal of Section 2.3 is to realize a constant-pressure wave in the experiment described by the transmission line model, therefore, we make an ansatz for the constant-pressure wave p_j,

$$p_{j+1} = \exp\left(\mathrm{i} k_0 \sum_{l=1}^{j} \phi_l\right) p_1, \tag{A.32}$$

where ϕ_j is the accumulated phase in the j-th section. Just like the generating function $W(x)$ in our CI-waves in Eq. (2.2), the phases ϕ_j can be chosen arbitrarily.
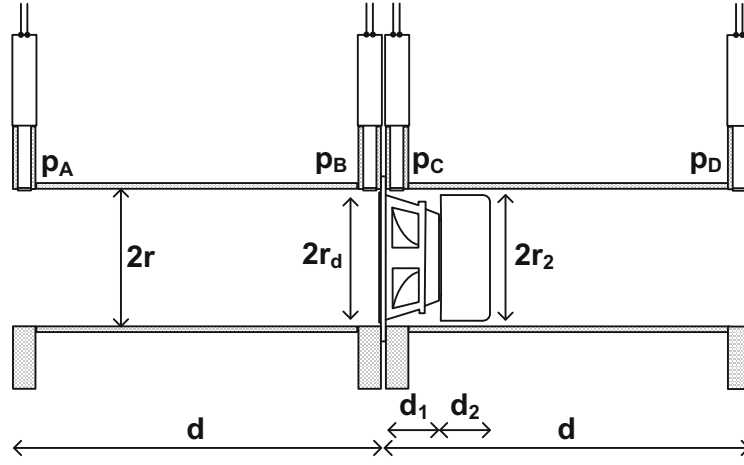
Fig A.2: One tube segment of the acoustic waveguide presented in Section 2.3 consisting of three parts with lengths $d_1 = 2.6\,\mathrm{cm}$, $d_2 = 2.8\,\mathrm{cm}$, $d = 34.4\,\mathrm{cm}$ and corresponding impedances Z_0, $Z_2 = S/(S-S_2)Z_0$ with $S = \pi r^2 = 40.7\,\mathrm{cm}^2$ and $S_2 = \pi r_2^2 = 37.4\,\mathrm{cm}^2$ and Z_0.

Our aim is to find the acoustic impedances Z_j that enable such a constant-pressure wave in Eq. (A.32). From Eq. (A.29) we find

$$Z_j = \frac{p_j - A_j p_{j+1} - B_j q_{j+1}}{C_j p_{j+1} + D_j q_{j+1}}, \tag{A.33}$$

i.e., the acoustic impedances Z_j as a function of the pressures p_j and volume flows q_j. Since the pressures p_j are determined by Eq. (A.32), we have to find an expression for the volume flows q_j. Solving the recursive formula for the volume flows q_j obtained from Eq. (A.29), $q_j = C_j p_{j+1} + D_j q_{j+1}$, yields

$$q_j = \frac{1}{\prod_{l=1}^{j-1} D_l} q_1 - \sum_{l=1}^{j-1} \frac{C_l}{\prod_{m=l}^{j-1} D_m} p_{l+1}. \tag{A.34}$$

Assuming an incident wave from the left with amplitude $p_{\mathrm{inc}} = 1\,\mathrm{Pa}$, we can use the boundary conditions

$$p_{n+1}/q_{n+1} = Z_R, \tag{A.35}$$
$$p_1/p_{\mathrm{inc}} = 1 + R, \tag{A.36}$$
$$q_1/p_{\mathrm{inc}} = (1 - R)/Z_L, \tag{A.37}$$

with R being the reflection coefficient. With these boundary conditions and Eq. (A.34) we know all p_j and q_j as a function of R. In order to calculate the

reflection coefficient R, we use Eqs. (A.32), (A.35) and (A.36):

$$(1 + R) \exp \left(\mathrm{i} k_0 \sum_{l=1}^{n} \phi_l \right) = Z_R \cdot q_{n+1}. \tag{A.38}$$

Inserting Eq. (A.34) for q_{n+1} into Eq. (A.38) yields

$$(1 + R) \exp \left(\mathrm{i} k_0 \sum_{l=1}^{n} \phi_l \right) = Z_R \left(\frac{1}{\prod_{l=1}^{n} D_l} q_1 - \sum_{l=1}^{n} \frac{C_l}{\prod_{m=l}^{n} D_m} p_{l+1} \right). \tag{A.39}$$

We now know all quantities except the reflection coefficient R, such that we can resolve Eq. (A.39) for R,

$$R = \frac{Z_{\mathrm{in}} - Z_L}{Z_{\mathrm{in}} + Z_L}. \tag{A.40}$$

with Z_{in} being the input impedance

$$Z_{\mathrm{in}} = Z_R \frac{1}{\prod_{l=1}^{n} D_l} \frac{1}{\exp \left(\mathrm{i} k_0 \sum_{l=1}^{n} \phi_l \right) + Z_R \sum_{l=1}^{n} \frac{C_l}{\prod_{m=l}^{n} D_m} \exp \left(\mathrm{i} k_0 \sum_{r=1}^{l} \phi_r \right)}. \tag{A.41}$$

Now, that we know all acoustic quantities, we are able to calculate the acoustic impedances Z_j with Eq. (A.33) for a given set of phases ϕ_j.

To summarize our protocol for generating constant-pressure waves, we first choose values for our phases ϕ_j determining the pressures p_j [via Eq. (A.32)] as a function of either p_1 or R, respectively. In a next step, we solve the recursion for q_j, such that we know all q_j as a function of R. Using Eqs. (A.41) and (A.40) we are able to calculate R that finally allows us to determine our acoustic impedances Z_j with Eq. (A.33). Fixing all the phases ϕ_j, the reflection coefficient R and the impedances Z_j are fixed as well. Our aim, however, is to generate reflectionless scattering states, i.e., $R = 0$. To realize this, we have to relax two degrees of freedom, e.g., ϕ_1 and ϕ_2 (i.e., two phases) and tune them in such a way that the reflection coefficient R is minimized. Since there are many other parameters such as the wavelength of the incident wave λ_0, the length and the size of the tube etc. it is not possible to get $R = 0$ for every arbitrary parameter set. For most cases, however, it is possible to get a constant-pressure wave featuring zero reflection.

A.4 Time-delay operator for non-regular transmission matrices

The construction of $q_\omega = -\mathrm{i} t^{-1} \partial t / \partial \omega$ involves the inverse of the transmission matrix t^{-1}. If t is non-square or singular, which can be the case in poorly transmitting systems, an ordinary inversion cannot be computed anymore. However, an effective

inverse can be calculated by separating off poorly transmitting channels of t, as we explain in the following. We start with a singular value decomposition (SVD) of the transmission matrix $t = U\Sigma V^\dagger$, where U consists of the eigenvectors of $tt^\dagger$ stored in its columns and V consists of the eigenvectors of $t^\dagger t$, respectively. For an $M \times N$ transmission matrix, the matrices U and V are square $M \times M$ and $N \times N$ matrices. The rectangular $M \times N$ matrix Σ contains the singular values $\sigma^{(i)}$ on its diagonal, which are the square roots of the common eigenvalues of both $t^\dagger t$ and $tt^\dagger$. For a singular or non-square transmission matrix t, at least one singular value is zero. In a next step, we only keep a certain number N_η of singular values $\tilde{\Sigma}$ that are larger than some cutoff value η with corresponding singular vectors stored in $\tilde{U}$ and $\tilde{V}$. Projecting the full transmission matrix t onto the kept transmitting channels according to $\tilde{t} = \tilde{U}^\dagger t \tilde{V}$, we end up with an $N_\eta \times N_\eta$ invertible transmission matrix $\tilde{t}$. Projecting back onto the original vector space gives the effective inversion

$$t^{-1} := \tilde{V}(\tilde{U}^\dagger t \tilde{V})^{-1}\tilde{U}^\dagger. \tag{A.42}$$

Projecting also the derivative onto the selected subspace with the corresponding projection operators $P_{\tilde{U}} = \tilde{U}\tilde{U}^\dagger$ and $P_{\tilde{V}} = \tilde{V}\tilde{V}^\dagger$, we end up with the construction rule for the operator

$$\tilde{q}_\omega = -\mathrm{i}\tilde{V}(\tilde{U}^\dagger t \tilde{V})^{-1}\tilde{U}^\dagger \tilde{U}\tilde{U}^\dagger \frac{\partial t}{\partial \omega}\tilde{V}\tilde{V}^\dagger, \tag{A.43}$$

from which its eigenvectors can now be calculated.

A.5 Green's function method

In order to solve the Helmholtz Eq. (A.20) in two dimensions numerically, we discretize the scattering region on a Cartesian grid with a grid spacing $\Delta_x = \Delta_y$ that is about a factor 20 smaller than the considered wavelength λ_0. This discretization allows us to reformulate the scattering problem as a standard matrix equation involving very large matrices. The central quantity in our approach is the so-called Green's function, that contains the information on how any incoming wave produces a certain wave pattern inside the entire scattering system. We calculated this Green's function through an efficient "modular" approach [126, 127] that involves the inversion of large matrices on a computer cluster using efficient linear algebra packages. The computer code using this Green's function method was written by Florian Libisch [127].

A.6 Correlated disorder

A correlated disorder, as used in Section 3.2, can be generated as follows: (i) for each grid point $\vec{r}$ of the scattering region a random number for the quantity

$n^2(\vec{r}) - 1 =: x(\vec{r})$ is drawn uniformly between 0 and 1. (ii) These random numbers are smoothed with a Gaussian correlation function

$$C(|\vec{r} - \vec{r}\,'|) = \langle [x(\vec{r}) - \langle x(\vec{r}) \rangle] \cdot [x(\vec{r}') - \langle x(\vec{r}') \rangle] \rangle \qquad \text{(A.44)}$$
$$\propto \exp\left(\frac{-|\vec{r} - \vec{r}\,'|}{2\xi}\right),$$

with a certain correlation length ξ. (iii) The mean value is subtracted from all $x(\vec{r})$. (iv) We rescale all values by

$$\tilde{x}(\vec{r}) = x(\vec{r}) \cdot \left(\frac{a}{\sqrt{12\langle x^2(\vec{r}) \rangle}}\right) + b, \qquad \text{(A.45)}$$

such that $\langle \tilde{x}(\vec{r}) \rangle = b$ and $\langle \tilde{x}^2(\vec{r}) \rangle = a^2/12 + b^2$. For the calculation used in Section 3.2 we choose $a = 0.21$ and $b = 0.105$. (v) In a last step we subtract the minimum value, i.e., $\tilde{x}'(\vec{r}) = \tilde{x}(\vec{r}) - \min[\tilde{x}(\vec{r})]$, to assure $\tilde{x}'(\vec{r}) > 0$ [since $n^2(\vec{r})$ has to be larger than 1] and, finally, obtain the refractive index by $n(\vec{r}) = \sqrt{1 + \tilde{x}'(\vec{r})}$. We end up with a correlated refractive index $n(\vec{r})$ characterized by a correlation length $\xi = 6 = 3\lambda_0$, minimum/maximum values: $\min[n(\vec{r})] = 1$ and $\max[n(\vec{r})] \approx 1.19$, a mean value $\mathrm{mean}[n(\vec{r})] \approx 1.1$ and a standard deviation $\mathrm{std}[n(\vec{r})] \approx 0.03$.

Bibliography

[1] A. Guo, G. J. Salamo, D. Duchesne, R. Morandotti, M. Volatier-Ravat, V. Aimez, G. A. Siviloglou, and D. N. Christodoulides, "Observation of PT-Symmetry Breaking in Complex Optical Potentials," *Physical Review Letters*, vol. 103, no. 9, p. 093902, 2009.

[2] K. G. Makris, R. El-Ganainy, D. N. Christodoulides, and Z. H. Musslimani, "Beam Dynamics in PT Symmetric Optical Lattices," *Physical Review Letters*, vol. 100, no. 10, p. 103904, 2008.

[3] Y. D. Chong, L. Ge, H. Cao, and A. D. Stone, "Coherent Perfect Absorbers: Time-Reversed Lasers," *Physical Review Letters*, vol. 105, no. 5, p. 053901, 2010.

[4] W. Wan, Y. Chong, L. Ge, H. Noh, A. D. Stone, and H. Cao, "Time-Reversed Lasing and Interferometric Control of Absorption," *Science*, vol. 331, no. 6019, p. 889, 2011.

[5] Y. D. Chong and A. D. Stone, "Hidden Black: Coherent Enhancement of Absorption in Strongly Scattering Media," *Physical Review Letters*, vol. 107, no. 16, p. 163901, 2011.

[6] C. W. Hsu, A. Goetschy, Y. Bromberg, A. D. Stone, and H. Cao, "Broadband Coherent Enhancement of Transmission and Absorption in Disordered Media," *Physical Review Letters*, vol. 115, no. 22, p. 223901, 2015.

[7] K. Pichler, M. Kühmayer, J. Böhm, A. Brandstötter, P. Ambichl, U. Kuhl, and S. Rotter, "Random anti-lasing through coherent perfect absorption in a disordered medium," *Nature*, vol. 567, no. 7748, p. 351, 2019.

[8] M. Brandstetter, M. Liertzer, C. Deutsch, P. Klang, J. Schöberl, H. E. Türeci, G. Strasser, K. Unterrainer, and S. Rotter, "Reversing the pump dependence of a laser at an exceptional point," *Nature Communications*, vol. 5, p. 4034, 2014.

[9] M. Liertzer, L. Ge, A. Cerjan, A. D. Stone, H. E. Türeci, and S. Rotter, "Pump-Induced Exceptional Points in Lasers," *Physical Review Letters*, vol. 108, no. 17, p. 173901, 2012.

[10] B. Peng, . K. Ozdemir, S. Rotter, H. Yilmaz, M. Liertzer, F. Monifi, C. M. Bender, F. Nori, and L. Yang, "Loss-induced suppression and revival of lasing," *Science*, vol. 346, no. 6207, p. 328, 2014.

[11] K. G. Makris, L. Ge, and H. E. Türeci, "Anomalous Transient Amplification of Waves in Non-normal Photonic Media," *Physical Review X*, vol. 4, no. 4, p. 041044, 2014.

[12] J. Raftery, D. Sadri, S. Schmidt, H. E. Türeci, and A. A. Houck, "Observation of a Dissipation-Induced Classical to Quantum Transition," *Physical Review X*, vol. 4, no. 3, p. 031043, 2014.

[13] C. E. Rüter, K. G. Makris, R. El-Ganainy, D. N. Christodoulides, M. Segev, and D. Kip, "Observation of parity–time symmetry in optics," *Nature Physics*, vol. 6, no. 3, p. 192, 2010.

[14] T. Kottos, "Optical physics: Broken symmetry makes light work," *Nature Physics*, vol. 6, no. 3, p. 166, 2010.

[15] C. M. Bender and S. Boettcher, "Real Spectra in Non-Hermitian Hamiltonians Having PT Symmetry," *Physical Review Letters*, vol. 80, no. 24, p. 5243, 1998.

[16] J. Cham, "Top 10 physics discoveries of the last 10 years," *Nature Physics*, vol. 11, no. 10, p. 799, 2015.

[17] R. El-Ganainy, K. G. Makris, M. Khajavikhan, Z. H. Musslimani, S. Rotter, and D. N. Christodoulides, "Non-Hermitian physics and PT symmetry," *Nature Physics*, vol. 14, no. 1, p. 11, 2018.

[18] Ş. K. Özdemir, S. Rotter, F. Nori, and L. Yang, "Parity–time symmetry and exceptional points in photonics," *Nature Materials*, vol. 18, no. 8, p. 783, 2019.

[19] S. Klaiman, U. Günther, and N. Moiseyev, "Visualization of Branch Points in PT-Symmetric Waveguides," *Physical Review Letters*, vol. 101, no. 8, p. 080402, 2008.

[20] F. Nazari, N. Bender, H. Ramezani, M. Moravvej-Farshi, D. N. Christodoulides, and T. Kottos, "Optical isolation via PT-symmetric nonlinear Fano resonances," *Optics Express*, vol. 22, no. 8, p. 9574, 2014.

[21] B. Peng, Ş. K. Özdemir, F. Lei, F. Monifi, M. Gianfreda, G. L. Long, S. Fan, F. Nori, C. M. Bender, and L. Yang, "Parity-time-symmetric whispering-gallery microcavities," *Nature Physics*, vol. 10, no. 5, p. 394, 2014.

[22] L. Chang, X. Jiang, S. Hua, C. Yang, J. Wen, L. Jiang, G. Li, G. Wang, and M. Xiao, "Parity-time symmetry and variable optical isolation in active-passive-coupled microresonators," *Nature Photonics*, vol. 8, no. 7, p. 524, 2014.

[23] A. Regensburger, C. Bersch, M.-A. Miri, G. Onishchukov, D. N. Christodoulides, and U. Peschel, "Parity-time synthetic photonic lattices," *Nature*, vol. 488, no. 7410, p. 167, 2012.

[24] Z. Lin, H. Ramezani, T. Eichelkraut, T. Kottos, H. Cao, and D. N. Christodoulides, "Unidirectional Invisibility Induced by PT-Symmetric Periodic Structures," *Physical Review Letters*, vol. 106, no. 21, p. 213901, 2011.

[25] L. Feng, Y.-L. Xu, W. S. Fegadolli, M.-H. Lu, J. E. B. Oliveira, V. R. Almeida, Y.-F. Chen, and A. Scherer, "Experimental demonstration of a unidirectional reflectionless parity-time metamaterial at optical frequencies," *Nature Materials*, vol. 12, no. 2, p. 108, 2013.

[26] L. Feng, X. Zhu, S. Yang, H. Zhu, P. Zhang, X. Yin, Y. Wang, and X. Zhang, "Demonstration of a large-scale optical exceptional point structure," *Optics Express*, vol. 22, no. 2, p. 1760, 2014.

[27] K. G. Makris, Z. H. Musslimani, D. N. Christodoulides, and S. Rotter, "Constant-intensity waves and their modulation instability in non-Hermitian potentials," *Nature Communications*, vol. 6, p. 8257, 2015.

[28] K. G. Makris, A. Brandstötter, P. Ambichl, Z. H. Musslimani, and S. Rotter, "Wave propagation through disordered media without backscattering and intensity variations," *Light: Science & Applications*, no. 6, p. e17030, 2017.

[29] K. G. Makris, A. Brandstötter, and S. Rotter, "Constant-Intensity Waves in Non-Hermitian Media," in *Parity-Time Symmetry and Its Applications* (D. Christodoulides and J. Yang, eds.), vol. 280, p. 535, Springer Singapore, 2018.

[30] A. Brandstötter, K. G. Makris, and S. Rotter, "Scattering-free pulse propagation through invisible non-Hermitian media," *Physical Review B*, vol. 99, no. 11, p. 115402, 2019.

[31] A. Lagendijk and B. A. van Tiggelen, "Resonant multiple scattering of light," *Physics Reports*, vol. 270, no. 3, p. 143, 1996.

[32] P. Sebbah, *Waves and Imaging through Complex Media*. Springer Netherlands, 2001.

[33] A. P. Mosk, A. Lagendijk, G. Lerosey, and M. Fink, "Controlling waves in space and time for imaging and focusing in complex media," *Nature Photonics*, vol. 6, no. 5, p. 283, 2012.

[34] D. S. Wiersma, "Disordered photonics," *Nature Photonics*, vol. 7, no. 3, p. 188, 2013.

[35] S. Rotter and S. Gigan, "Light fields in complex media: Mesoscopic scattering meets wave control," *Reviews of Modern Physics*, vol. 89, no. 1, p. 015005, 2017.

[36] G. Lerosey, J. de Rosny, A. Tourin, and M. Fink, "Focusing Beyond the Diffraction Limit with Far-Field Time Reversal," *Science*, vol. 315, no. 5815, p. 1120, 2007.

[37] L. Levi, M. Rechtsman, B. Freedman, T. Schwartz, O. Manela, and M. Segev, "Disorder-Enhanced Transport in Photonic Quasicrystals," *Science*, vol. 332, no. 6037, p. 1541, 2011.

[38] S. Karbasi, R. J. Frazier, K. W. Koch, T. Hawkins, J. Ballato, and A. Mafi, "Image transport through a disordered optical fibre mediated by transverse Anderson localization," *Nature Communications*, vol. 5, p. 3362, 2014.

[39] B. Redding, S. F. Liew, R. Sarma, and H. Cao, "Compact spectrometer based on a disordered photonic chip," *Nature Photonics*, vol. 7, no. 9, p. 746, 2013.

[40] D. S. Wiersma, "The physics and applications of random lasers," *Nature Physics*, vol. 4, no. 5, p. 359, 2008.

[41] M. Leonetti, C. Conti, and C. Lopez, "Switching and amplification in disordered lasing resonators," *Nature Communications*, vol. 4, no. 1, p. 1740, 2013.

[42] T. Hisch, M. Liertzer, D. Pogany, F. Mintert, and S. Rotter, "Pump-Controlled Directional Light Emission from Random Lasers," *Physical Review Letters*, vol. 111, no. 2, p. 023902, 2013.

[43] N. Bachelard, S. Gigan, X. Noblin, and P. Sebbah, "Adaptive pumping for spectral control of random lasers," *Nature Physics*, vol. 10, no. 6, p. 426, 2014.

[44] B. Redding, M. A. Choma, and H. Cao, "Speckle-free laser imaging using random laser illumination," *Nature Photonics*, vol. 6, no. 6, p. 355, 2012.

[45] S. M. Popoff, G. Lerosey, R. Carminati, M. Fink, A. C. Boccara, and S. Gigan, "Measuring the Transmission Matrix in Optics: An Approach to the Study and Control of Light Propagation in Disordered Media," *Physical Review Letters*, vol. 104, no. 10, p. 100601, 2010.

[46] H. Yu, T. R. Hillman, W. Choi, J. O. Lee, M. S. Feld, R. R. Dasari, and Y. Park, "Measuring Large Optical Transmission Matrices of Disordered Media," *Physical Review Letters*, vol. 111, no. 15, p. 153902, 2013.

[47] I. M. Vellekoop and A. P. Mosk, "Focusing coherent light through opaque strongly scattering media," *Optics Letters*, vol. 32, no. 16, p. 2309, 2007.

[48] I. M. Vellekoop, A. Lagendijk, and A. P. Mosk, "Exploiting disorder for perfect focusing," *Nature Photonics*, vol. 4, no. 5, p. 320, 2010.

[49] D. J. McCabe, A. Tajalli, D. R. Austin, P. Bondareff, I. A. Walmsley, S. Gigan, and B. Chatel, "Spatio-temporal focusing of an ultrafast pulse through a multiply scattering medium," *Nature Communications*, vol. 2, p. 447, 2011.

[50] O. Katz, E. Small, Y. Bromberg, and Y. Silberberg, "Focusing and compression of ultrashort pulses through scattering media," *Nature Photonics*, vol. 5, no. 6, p. 372, 2011.

[51] E. van Putten and A. Mosk, "The information age in optics: Measuring the transmission matrix," *Physics*, vol. 3, 2010.

[52] I. Freund, "Looking through walls and around corners," *Physica A: Statistical Mechanics and its Applications*, vol. 168, no. 1, p. 49, 1990.

[53] J. Bertolotti, E. G. van Putten, C. Blum, A. Lagendijk, W. L. Vos, and A. P. Mosk, "Non-invasive imaging through opaque scattering layers," *Nature*, vol. 491, no. 7423, p. 232, 2012.

[54] O. Katz, E. Small, and Y. Silberberg, "Looking around corners and through thin turbid layers in real time with scattered incoherent light," *Nature Photonics*, vol. 6, no. 8, p. 549, 2012.

[55] O. Katz, P. Heidmann, M. Fink, and S. Gigan, "Non-invasive single-shot imaging through scattering layers and around corners via speckle correlations," *Nature Photonics*, vol. 8, no. 10, p. 784, 2014.

[56] D. J. Richardson, J. M. Fini, and L. E. Nelson, "Space-division multiplexing in optical fibres," *Nature Photonics*, vol. 7, no. 5, p. 354, 2013.

[57] J. Carpenter, B. J. Eggleton, and J. Schröder, "Observation of Eisenbud–Wigner–Smith states as principal modes in multimode fibre," *Nature Photonics*, vol. 9, no. 11, p. 751, 2015.

[58] W. Xiong, P. Ambichl, Y. Bromberg, B. Redding, S. Rotter, and H. Cao, "Spatiotemporal Control of Light Transmission through a Multimode Fiber with Strong Mode Coupling," *Physical Review Letters*, vol. 117, no. 5, p. 053901, 2016.

[59] Z. Merali, "Optics: Super vision," *Nature News*, vol. 518, no. 7538, p. 158, 2015.

[60] H. Yu, J. Park, K. Lee, J. Yoon, K. Kim, S. Lee, and Y. Park, "Recent advances in wavefront shaping techniques for biomedical applications," *Current Applied Physics*, vol. 15, no. 5, p. 632, 2015.

[61] E. Rivet, A. Brandstötter, K. G. Makris, H. Lissek, S. Rotter, and R. Fleury, "Constant-pressure sound waves in non-Hermitian disordered media," *Nature Physics*, vol. 14, no. 9, p. 942, 2018.

[62] N. de Zordo, *Wave Engineering in Non-Hermitian Scattering Systems*. Bachelor Thesis, TU Wien, 2018.

[63] L. Leczek, *Efficient Sound Absorption through Predetermined-Pressure Waves*. Bachelor Thesis (in preparation), TU Wien, 2020.

[64] K. G. Makris, I. Krešić, A. Brandstötter, and S. Rotter, "Scattering-free channels of invisibility across non-Hermitian media," *Optica*, vol. 7, no. 6, p. 619, 2020.

[65] S. Rotter, P. Ambichl, and F. Libisch, "Generating Particlelike Scattering States in Wave Transport," *Physical Review Letters*, vol. 106, no. 12, p. 120602, 2011.

[66] B. Gérardin, J. Laurent, P. Ambichl, C. Prada, S. Rotter, and A. Aubry, "Particlelike wave packets in complex scattering systems," *Physical Review B*, vol. 94, no. 1, p. 014209, 2016.

[67] J. Böhm, A. Brandstötter, P. Ambichl, S. Rotter, and U. Kuhl, "*In Situ* realization of particlelike scattering states in a microwave cavity," *Physical Review A*, vol. 97, no. 2, p. 021801(R), 2018.

[68] A. Brandstötter, A. Girschik, P. Ambichl, and S. Rotter, "Shaping the branched flow of light through disordered media," *Proceedings of the National Academy of Sciences*, vol. 116, no. 27, p. 13260, 2019.

[69] P. Ambichl, A. Brandstötter, J. Böhm, M. Kühmayer, U. Kuhl, and S. Rotter, "Focusing inside Disordered Media with the Generalized Wigner-Smith Operator," *Physical Review Letters*, vol. 119, no. 3, p. 033903, 2017.

[70] M. Horodynski, M. Kühmayer, A. Brandstötter, K. Pichler, Y. V. Fyodorov, U. Kuhl, and S. Rotter, "Optimal wave fields for micromanipulation in complex scattering environments," *Nature Photonics*, vol. 14, no. 3, p. 149, 2020.

[71] H. Cao, "Lasing in random media," *Waves in Random Media*, vol. 13, no. 3, p. R1, 2003.

[72] P. Yeh, *Optical Waves in Layered Media*. Wiley-Interscience, 2005.

[73] E. H. Hauge, J. P. Falck, and T. A. Fjeldly, "Transmission and reflection times for scattering of wave packets off tunneling barriers," *Physical Review B*, vol. 36, no. 8, p. 4203, 1987.

[74] F. Wagner, *Constant-Intensity Refractive Indices Created with Deep Learning*. Project Thesis, TU Wien, 2020.

[75] S. Longhi, "A unidirectionally invisible PT-symmetric complex crystal with arbitrary thickness," *Journal of Physics A: Mathematical and Theoretical*, vol. 47, no. 48, p. 485302, 2014.

[76] S. Longhi, "Invisibility in PT-symmetric complex crystals," *Journal of Physics A: Mathematical and Theoretical*, vol. 44, no. 48, p. 485302, 2011.

[77] A. Mostafazadeh, "Invisibility and PT symmetry," *Physical Review A*, vol. 87, no. 1, p. 012103, 2013.

[78] S. Longhi, "Half-spectral unidirectional invisibility in non-Hermitian periodic optical structures," *Optics Letters*, vol. 40, no. 23, p. 5694, 2015.

[79] S. A. R. Horsley, M. Artoni, and G. C. La Rocca, "Spatial Kramers–Kronig relations and the reflection of waves," *Nature Photonics*, vol. 9, no. 7, p. 436, 2015.

[80] S. Longhi, "Wave reflection in dielectric media obeying spatial Kramers-Kronig relations," *Europhysics Letters*, vol. 112, no. 6, p. 64001, 2015.

[81] S. A. R. Horsley, C. G. King, and T. G. Philbin, "Wave propagation in complex coordinates," *Journal of Optics*, vol. 18, no. 4, p. 044016, 2016.

[82] R. Fleury, D. Sounas, and A. Alù, "An invisible acoustic sensor based on parity-time symmetry," *Nature Communications*, vol. 6, no. 1, p. 5905, 2015.

[83] C. Shi, M. Dubois, Y. Chen, L. Cheng, H. Ramezani, Y. Wang, and X. Zhang, "Accessing the exceptional points of parity-time symmetric acoustics," *Nature Communications*, vol. 7, no. 1, p. 11110, 2016.

[84] P. Berini and I. De Leon, "Surface plasmon–polariton amplifiers and lasers," *Nature Photonics*, vol. 6, no. 1, p. 16, 2012.

[85] Y. Aurégan and V. Pagneux, "PT -Symmetric Scattering in Flow Duct Acoustics," *Physical Review Letters*, vol. 118, no. 17, p. 174301, 2017.

[86] R. Fleury and A. Alù, "Extraordinary Sound Transmission through Density-Near-Zero Ultranarrow Channels," *Physical Review Letters*, vol. 111, no. 5, p. 055501, 2013.

[87] D.-Y. Maa, "Potential of microperforated panel absorber," *The Journal of the Acoustical Society of America*, vol. 104, no. 5, p. 2861, 1998.

[88] S. Yu, X. Piao, and N. Park, "Bohmian Photonics for Independent Control of the Phase and Amplitude of Waves," *Physical Review Letters*, vol. 120, no. 19, p. 193902, 2018.

[89] L. Eisenbud, *The Formal Properties of Nuclear Collisions*. PhD thesis, Princeton University, 1948.

[90] E. P. Wigner, "Lower Limit for the Energy Derivative of the Scattering Phase Shift," *Physical Review*, vol. 98, no. 1, p. 145, 1955.

[91] F. T. Smith, "Lifetime Matrix in Collision Theory," *Physical Review*, vol. 118, no. 1, p. 349, 1960.

[92] R. Pierrat, P. Ambichl, S. Gigan, A. Haber, R. Carminati, and S. Rotter, "Invariance property of wave scattering through disordered media," *Proceedings of the National Academy of Sciences*, vol. 111, no. 50, p. 17765, 2014.

[93] M. Davy, Z. Shi, J. Wang, X. Cheng, and A. Z. Genack, "Transmission Eigenchannels and the Densities of States of Random Media," *Physical Review Letters*, vol. 114, no. 3, p. 033901, 2015.

[94] M. Davy, Z. Shi, J. Park, C. Tian, and A. Z. Genack, "Universal structure of transmission eigenchannels inside opaque media," *Nature Communications*, vol. 6, no. 1, p. 6893, 2015.

[95] R. Savo, R. Pierrat, U. Najar, R. Carminati, S. Rotter, and S. Gigan, "Observation of mean path length invariance in light-scattering media," *Science*, vol. 358, no. 6364, p. 765, 2017.

[96] P. del Hougne, R. Sobry, O. Legrand, F. Mortessagne, U. Kuhl, and M. Davy, "Experimental realization of optimal energy storage in resonators embedded in scattering media," *arXiv:2001.04658 [cond-mat, physics:physics]*, 2020.

[97] S. Fan and J. M. Kahn, "Principal modes in multimode waveguides," *Optics Letters*, vol. 30, no. 2, p. 135, 2005.

[98] M. A. Topinka, B. J. LeRoy, R. M. Westervelt, S. E. J. Shaw, R. Fleischmann, E. J. Heller, K. D. Maranowski, and A. C. Gossard, "Coherent branched flow in a two-dimensional electron gas," *Nature*, vol. 410, no. 6825, p. 183, 2001.

[99] E. J. Heller, R. Fleischmann, and T. Kramer, "Branched Flow," *arXiv:1910.07086*, 2019.

[100] M. P. Jura, M. A. Topinka, L. Urban, A. Yazdani, H. Shtrikman, L. N. Pfeiffer, K. W. West, and D. Goldhaber-Gordon, "Unexpected features of branched flow through high-mobility two-dimensional electron gases," *Nature Physics*, vol. 3, no. 12, p. 841, 2007.

[101] L. Kaplan, "Statistics of Branched Flow in a Weak Correlated Random Potential," *Physical Review Letters*, vol. 89, no. 18, p. 184103, 2002.

[102] E. J. Heller, K. E. Aidala, B. J. LeRoy, A. C. Bleszynski, A. Kalben, R. M. Westervelt, K. D. Maranowski, and A. C. Gossard, "Thermal Averages in a Quantum Point Contact with a Single Coherent Wave Packet," *Nano Letters*, vol. 5, no. 7, p. 1285, 2005.

[103] K. E. Aidala, R. E. Parrott, T. Kramer, E. J. Heller, R. M. Westervelt, M. P. Hanson, and A. C. Gossard, "Imaging magnetic focusing of coherent electron waves," *Nature Physics*, vol. 3, no. 7, p. 464, 2007.

[104] D. Maryenko, F. Ospald, K. v. Klitzing, J. H. Smet, J. J. Metzger, R. Fleischmann, T. Geisel, and V. Umansky, "How branching can change the conductance of ballistic semiconductor devices," *Physical Review B*, vol. 85, no. 19, p. 195329, 2012.

[105] E. J. Heller, L. Kaplan, and A. Dahlen, "Refraction of a Gaussian seaway," *Journal of Geophysical Research: Oceans*, vol. 113, no. C9, p. C09023, 2008.

[106] R. Höhmann, U. Kuhl, H.-J. Stöckmann, L. Kaplan, and E. J. Heller, "Freak Waves in the Linear Regime: A Microwave Study," *Physical Review Letters*, vol. 104, no. 9, p. 093901, 2010.

[107] L. H. Ying, Z. Zhuang, E. J. Heller, and L. Kaplan, "Linear and nonlinear rogue wave statistics in the presence of random currents," *Nonlinearity*, vol. 24, no. 11, p. R67, 2011.

[108] J. J. Metzger, R. Fleischmann, and T. Geisel, "Statistics of Extreme Waves in Random Media," *Physical Review Letters*, vol. 112, no. 20, p. 203903, 2014.

[109] M. Mattheakis and G. P. Tsironis, "Extreme Waves and Branching Flows in Optical Media," in *Quodons in Mica* (J. F. R. Archilla, N. Jiménez, V. J. Sánchez-Morcillo, and L. M. García-Raffi, eds.), vol. 221, p. 425, Springer International Publishing, 2015.

[110] H. Degueldre, J. J. Metzger, T. Geisel, and R. Fleischmann, "Random focusing of tsunami waves," *Nature Physics*, vol. 12, no. 3, p. 259, 2016.

[111] M. Mattheakis, I. Pitsios, G. Tsironis, and S. Tzortzakis, "Extreme events in complex linear and nonlinear photonic media," *Chaos, Solitons & Fractals*, vol. 84, p. 73, 2016.

[112] J. J. Metzger, R. Fleischmann, and T. Geisel, "Universal Statistics of Branched Flows," *Physical Review Letters*, vol. 105, no. 2, p. 020601, 2010.

[113] G. Green and R. Fleischmann, "Branched flow and caustics in nonlinear waves," *New Journal of Physics*, vol. 21, no. 8, p. 083020, 2019.

[114] X. Ni, W.-X. Wang, and Y.-C. Lai, "Origin of branched wave structures in optical media and long-tail algebraic intensity distribution," *Europhysics Letters*, vol. 96, no. 4, p. 44002, 2011.

[115] X. Ni, Y.-C. Lai, and W.-X. Wang, "Emergence of scaling associated with complex branched wave structures in optical medium," *Chaos: An Interdisciplinary Journal of Nonlinear Science*, vol. 22, no. 4, p. 043116, 2012.

[116] B. Liu and E. J. Heller, "Stability of Branched Flow from a Quantum Point Contact," *Physical Review Letters*, vol. 111, no. 23, p. 236804, 2013.

[117] B. Liu, "Classical and Quantum Stability of Branched Flow," *Journal of Physics: Conference Series*, vol. 626, no. 1, p. 012037, 2015.

[118] A. Patsyk, U. Sivan, M. Segev, and M. A. Bandres, "Observation of branched flow of light," *Nature*, vol. 583, no. 7814, p. 60, 2020.

[119] N. Blaunstein and C. Christodoulou, *Radio Propagation and Adaptive Antennas for Wireless Communication Links*. Wiley Series in Microwave and Optical Engineering, John Wiley & Sons, Inc., 2006.

[120] J. W. Hardy, *Adaptive Optics for Astronomical Telescopes*. No. 16 in Oxford Series in Optical and Imaging Sciences, Oxford University Press, 1998.

[121] R. P. Hodges, *Underwater Acoustics: Analysis, Design and Performance of Sonar*. John Wiley & Sons, Ltd, 2010.

[122] R. Horstmeyer, H. Ruan, and C. Yang, "Guidestar-assisted wavefront-shaping methods for focusing light into biological tissue," *Nature Photonics*, vol. 9, no. 9, p. 563, 2015.

[123] J. Kubby, S. Gigan, and M. Cui, eds., *Wavefront Shaping for Biomedical Imaging*. Advances in Microscopy and Microanalysis, Cambridge University Press, 2019.

[124] S. Popoff, G. Lerosey, M. Fink, A. C. Boccara, and S. Gigan, "Image transmission through an opaque material," *Nature Communications*, vol. 1, no. 6, p. 1, 2010.

[125] H. Yılmaz, C. W. Hsu, A. Yamilov, and H. Cao, "Transverse localization of transmission eigenchannels," *Nature Photonics*, vol. 13, no. 5, p. 352, 2019.

[126] S. Rotter, J.-Z. Tang, L. Wirtz, J. Trost, and J. Burgdörfer, "Modular recursive Green's function method for ballistic quantum transport," *Physical Review B*, vol. 62, no. 3, p. 1950, 2000.

[127] F. Libisch, S. Rotter, and J. Burgdörfer, "Coherent transport through graphene nanoribbons in the presence of edge disorder," *New Journal of Physics*, vol. 14, no. 12, p. 123006, 2012.

[128] G. Thalhammer, R. Steiger, S. Bernet, and M. Ritsch-Marte, "Optical macrotweezers: Trapping of highly motile micro-organisms," *Journal of Optics*, vol. 13, no. 4, p. 044024, 2011.

[129] R. Bowman, A. Jesacher, G. Thalhammer, G. Gibson, M. Ritsch-Marte, and M. Padgett, "Position clamping in a holographic counterpropagating optical trap," *Optics Express*, vol. 19, no. 10, p. 9908, 2011.

[130] A. Jannasch, M. Mahamdeh, and E. Schäffer, "Inertial Effects of a Small Brownian Particle Cause a Colored Power Spectral Density of Thermal Noise," *Physical Review Letters*, vol. 107, no. 22, p. 228301, 2011.

[131] D. Palima and J. Glückstad, "Gearing up for optical microrobotics: Micromanipulation and actuation of synthetic microstructures by optical forces: Gearing up for optical microrobotics," *Laser & Photonics Reviews*, vol. 7, no. 4, p. 478, 2013.

[132] T. Li, *Fundamental Tests of Physics with Optically Trapped Microspheres*. Springer Theses, Springer, 2013.

[133] S. Kheifets, A. Simha, K. Melin, T. Li, and M. G. Raizen, "Observation of Brownian Motion in Liquids at Short Times: Instantaneous Velocity and Memory Loss," *Science*, vol. 343, no. 6178, p. 1493, 2014.

[134] S. Longhi, "PT -symmetric laser absorber," *Physical Review A*, vol. 82, no. 3, p. 031801, 2010.

[135] D. G. Baranov, A. Krasnok, T. Shegai, A. Alù, and Y. Chong, "Coherent perfect absorbers: Linear control of light with light," *Nature Reviews Materials*, vol. 2, no. 12, p. 17064, 2017.

[136] M. Pu, Q. Feng, M. Wang, C. Hu, C. Huang, X. Ma, Z. Zhao, C. Wang, and X. Luo, "Ultrathin broadband nearly perfect absorber with symmetrical coherent illumination," *Optics Express*, vol. 20, no. 3, p. 2246, 2012.

[137] R. Bruck and O. L. Muskens, "Plasmonic nanoantennas as integrated coherent perfect absorbers on SOI waveguides for modulators and all-optical switches," *Optics Express*, vol. 21, no. 23, p. 27652, 2013.

[138] Y. Sun, W. Tan, H.-q. Li, J. Li, and H. Chen, "Experimental Demonstration of a Coherent Perfect Absorber with PT Phase Transition," *Physical Review Letters*, vol. 112, no. 14, p. 143903, 2014.

[139] T. Roger, S. Vezzoli, E. Bolduc, J. Valente, J. J. F. Heitz, J. Jeffers, C. Soci, J. Leach, C. Couteau, N. I. Zheludev, and D. Faccio, "Coherent perfect absorption in deeply subwavelength films in the single-photon regime," *Nature Communications*, vol. 6, no. 1, p. 7031, 2015.

[140] Z. J. Wong, Y.-L. Xu, J. Kim, K. O'Brien, Y. Wang, L. Feng, and X. Zhang, "Lasing and anti-lasing in a single cavity," *Nature Photonics*, vol. 10, no. 12, p. 796, 2016.

[141] C. Meng, X. Zhang, S. T. Tang, M. Yang, and Z. Yang, "Acoustic Coherent Perfect Absorbers as Sensitive Null Detectors," *Scientific Reports*, vol. 7, no. 1, p. 43574, 2017.

[142] O. Richoux, V. Achilleos, G. Theocharis, and I. Brouzos, "Subwavelength Interferometric Control of Absorption in Three-port Acoustic Network," *Scientific Reports*, vol. 8, no. 1, p. 12328, 2018.

[143] N. Kaina, M. Dupré, G. Lerosey, and M. Fink, "Shaping complex microwave fields in reverberating media with binary tunable metasurfaces," *Scientific Reports*, vol. 4, no. 1, p. 6693, 2015.

[144] G. Ma, X. Fan, P. Sheng, and M. Fink, "Shaping reverberating sound fields with an actively tunable metasurface," *Proceedings of the National Academy of Sciences*, vol. 115, no. 26, p. 6638, 2018.

[145] D. Gerlach and A. Paulraj, "Base station transmitting antenna arrays for multipath environments," *Signal Processing*, vol. 54, no. 1, p. 59, 1996.

[146] P. Yeh, A. Yariv, and C.-S. Hong, "Electromagnetic propagation in periodic stratified media I General theory*," *Journal of the Optical Society of America*, vol. 67, no. 4, p. 423, 1977.

Acknowledgments

Finally I would like to thank the following people who helped, inspired and encouraged me during the exciting and very rewarding time I was working on my PhD:

- My supervisor Stefan Rotter who gave me the possibility to conduct my PhD in a very professional and well functioning scientific group. He was always open for my questions and took time for discussions even in stressful times. He also put a lot of trust in me by sending me to conferences to present my results thus giving me the opportunity to gain experience. Beside his immense professional skills, I appreciate Stefan's human side of being a warm, understanding and respectful person.

- My long-time office colleague Matthias Kühmayer who always had an open ear to listen to my problems, ideas and random thoughts. Matthias was always willing to help and patiently explained things to me. I especially appreciate Matthias' numerical and programming skills that helped me a lot when I was in despair. I am also grateful for the warm and amusing, yet productive atmosphere in our office.

- My other office colleague Michael Horodynski who became an essential member of our group in a very short time. I am grateful for many interesting and fruitful discussions.

- My former colleagues Philipp Ambichl and Adrian Girschik who took a lot of time introducing me to most of the physical concepts which I used in this thesis. They were always willing to help and deepen my understanding of physics.

- The colleagues in my working group for interesting conversations and their contribution to a pleasant and constructive working atmosphere.

- Further, I am grateful for the contributions and support of all external collaboration partners who co-authored our mutual publications. Especially I thank (in alphabetical order) Julian Böhm, Romain Fleury, Sebastian Floss, Manfred Kaltenbacher, Ulrich Kuhl, Konstantinos Makris and Etienne Rivet from Nice, Lausanne, Crete and Vienna, respectively.

- My project-, bachelor- and diploma-students, Michael Horodynski, Nikolaus del Zordo, Lukas Leczek and Felix Wagner for the great job they did in their works which parts of this thesis are built on.

- Florian Libisch who granted me full access to his computer code and his PhD-student Thomas Fabian who helped me every time I had problems with it.

- Heike Höller, Sylvia Riedler and Ingrid Unger for assisting me with all the administrative workload.

- The Austrian Academy of Sciences (ÖAW) who funded parts of my PhD through the DOC Fellowship.

Last but not least I want to thank my family and friends for their moral support and for creating a healthy balance between my work and my private life.

List of publications

1. K. G. Makris, I. Krešić, A. Brandstötter, and S. Rotter, "Scattering-free channels of invisibility across non-Hermitian media," *Optica*, vol. 7, no. 6, p. 619, 2020

2. M. Horodynski, M. Kühmayer, A. Brandstötter, K. Pichler, Y. V. Fyodorov, U. Kuhl, and S. Rotter, "Optimal wave fields for micromanipulation in complex scattering environments," *Nature Photonics*, vol. 14, no. 3, p. 149, 2020

3. A. Brandstötter, A. Girschik, P. Ambichl, and S. Rotter, "Shaping the branched flow of light through disordered media," *Proceedings of the National Academy of Sciences*, vol. 116, no. 27, p. 13260, 2019

4. A. Brandstötter, K. G. Makris, and S. Rotter, "Scattering-free pulse propagation through invisible non-Hermitian media," *Physical Review B*, vol. 99, no. 11, p. 115402, 2019

5. K. Pichler, M. Kühmayer, J. Böhm, A. Brandstötter, P. Ambichl, U. Kuhl, and S. Rotter, "Random anti-lasing through coherent perfect absorption in a disordered medium," *Nature*, vol. 567, no. 7748, p. 351, 2019

6. K. G. Makris, A. Brandstötter, and S. Rotter, "Constant-Intensity Waves in Non-Hermitian Media," in *Parity-Time Symmetry and Its Applications* (D. Christodoulides and J. Yang, eds.), vol. 280, p. 535, Springer Singapore, 2018

7. E. Rivet, A. Brandstötter, K. G. Makris, H. Lissek, S. Rotter, and R. Fleury, "Constant-pressure sound waves in non-Hermitian disordered media," *Nature Physics*, vol. 14, no. 9, p. 942, 2018

8. J. Böhm, A. Brandstötter, P. Ambichl, S. Rotter, and U. Kuhl, "*In Situ* realization of particlelike scattering states in a microwave cavity," *Physical Review A*, vol. 97, no. 2, p. 021801(R), 2018

9. P. Ambichl, A. Brandstötter, J. Böhm, M. Kühmayer, U. Kuhl, and S. Rotter, "Focusing inside Disordered Media with the Generalized Wigner-Smith Operator," *Physical Review Letters*, vol. 119, no. 3, p. 033903, 2017

10. K. G. Makris, A. Brandstötter, P. Ambichl, Z. H. Musslimani, and S. Rotter, "Wave propagation through disordered media without backscattering and intensity variations," *Light: Science & Applications*, no. 6, p. e17030, 2017

Curriculum Vitae

PERSONAL DATA

Name:	**Dipl.-Ing. Andre BRANDSTÖTTER, BSc**
Address:	
Date of birth:	**6. May 1991**
Place of birth:	**Vienna**
Nationality:	**Austrian**
Mobile number:	
E-mail-address:	**abrandstotter@hotmail.com**

EDUCATION

since July 2016

Vienna University of Technology (TU Wien), Inst. for Theoretical Physics
Doctoral program in Engineering Sciences: Technical Physics

Advisor:	Stefan Rotter (Vienna University of Technology)
PhD thesis:	Photonics with Loss and Disorder

Oct. 2013 – June 2016

Vienna University of Technology (TU Wien)
Master of Science (Dipl.-Ing.) in Technical Physics
Graduated with highest distinction (8.6.2016)

Diploma thesis:	Wave Control in Complex Media: from System Design to Wave Front Shaping
Advisor:	Stefan Rotter (Vienna University of Technology)

Oct. 2010 – Oct. 2013

Vienna University of Technology (TU Wien)
Bachelor of Science in Technical Physics

Bachelor thesis:	Implementation and Characterization of a Coincidence-Counting Module for Bell Experiments
Advisor:	Anton Zeilinger (IQOQI Vienna)

Sept. 2001 – June 2009

High school GRg Draschestraße 90-92:
Graduated with highest distinction (23.6.2009)
Focus on science

WORK EXPERIENCE

since July 2016 **Project assistant at TU Wien** (see above)

Apr. 2015 – Jan. 2016,
Oct. 2013 – Dec. 2014,
Oct. 2012 – July 2013

Freelancer at the Austrian Institute of Technology (AIT)

Department:	Transportation Infrastructure Technology
Advisor:	Roland Spielhofer

July 2013,
July 2012 – Sept. 2012

Summer job at the Austrian Institute of Technology (AIT)

Department:	Transportation Infrastructure Technology
Advisor:	Roland Spielhofer

July 2010 – July 2012 **Part time salesman at Brotauto (mobile bakery)**

Nov. 2009 – July 2010 **Community service in a geriatric center**

Aug. 2006, Aug. 2007, Aug. 2008 **Summer job in the Austrian Chamber of Commerce**

AWARDS

Participating in the high-potential-program for students of the Vienna University of Technology (Nov. 2018 and Mar. 2019)

DOC Fellowship of the Austrian Academy of Sciences (ÖAW) since Sept. 2018

Award of excellence of the Faculty of Physics of the Vienna University of Technology ("Leistungsstipendium") in the year 2014

SCIENTIFIC CONTRIBUTION

Participation in 9 national/international conferences (2x USA, 2x France, 2x Great Britain, Mexico, Germany, Austria) with 6 oral talks and 3 poster presentations (see "conferences and summer schools")

Participation in 2 summer schools in Austria and Greece (see "conferences and summer schools")

Scientific stays at the Université Côte d'Azur in Nice, France (2 weeks) and at the College of Optics and Photonics (CREOL) in Florida, USA (3 weeks)

9 scientific publications in peer-reviewed journals (including 2 as first author) in Nature, Nature Physics, Nature Photonics, Physical Review Letters, Proceedings of the National Academy of Sciences, Light: Science & Applications, Optica, Physical Review B, Physical Review A

1 co-author of a book chapter

CONFERENCES AND SUMMER SCHOOLS

Sept. 22 – 27, 2019	**Summer school** on "Imaging in Wave Physics: Multi Wave and Large Sensor Networks", Cargése, Corsica, France **Poster presentation** on "Optimal Wave Fields for Micro-manipulation in Complex Scattering Environments"
Aug. 26 - 30, 2019	**Conference** on "Mathematical and Numerical Aspects of Wave Propagation", Vienna, Austria **30-min talk** on "Constant-intensity waves in non-Hermitian media"
Sept. 3 - 7, 2018	**Conference** on "Billiards (Dynamics Days Europe)", Loughborough, UK **30-min talk** on "Coherent wave scattering in billiards: time-delay and beyond"
Jan. 27 – Feb. 1, 2018	**Conference** on "Adaptive Optics and Wavefront Control for Biological Systems (Photonics West)", San Francisco, USA **30-min talk** on "Perfect Transmission and Focusing in Disordered Media"
July 25 – 28, 2017	**Conference** on "Complex Nanophotonics (Science Camp)", Windsor, UK **20-min talk** on "Focusing Inside Disordered Media with the Generalized Wigner-Smith Operator"

June 25 – 29, 2017	**Conference** on "Lasers and Electro-Optics (CLEO Europe)", Munich, Germany **Poster presentation** on "Non-Hermitian Focusing Deep Inside Strongly Disordered Scattering Media"
Sept. 12 – 16, 2016	**Summer School** on "Complex Quantum Systems (CoQuS)", Vienna, Austria
Jan. 3 – 8, 2016	**Conference** on the "Physics of Quantum Electronics (PQE)", Snowbird, Utah, USA **20-min talk** on "Controlling Branched Flow"
Aug. 22 – Sept. 12, 2015	**Conference** and **scientific gathering** on "Quantum Chaos, Billards, RMT and more", Cuernavaca, Mexico **45-min talk** on "New Insights on Scattering through Disordered and Non-Hermitian Media"
May 25 – 29, 2015	**Summer school** on "Imaging, Focusing and Sensing in Wave Physics", Cargése, Corsica, France **Poster presentation** on "Controlling the Branched Flow of Light through Disordered Media"
Aug. 15 – 30, 2013	**Summer school** on "Charged Particle Optics: Theory & Simulation (CPOTS)", Heraklion, Crete, Greece

LANGUAGES

German	native speaker
English	fluent
Spanish	basic

PROGRAMMING SKILLS

MATLAB	advanced
Python	advanced
Fortran	basic knowledge
C/C++	basic knowledge
Machine learning/ Deep learning	basic knowledge

INTERESTS AND ABILITIES

ECDL Certificate
Driving license (B)
Course in first aid
Sports: running, strength training, cycling
Diving: licensed Advanced Open Water Diver
Aquaristics: freshwater fish, shrimp, aquatic plants
Reading: classics, popular science
Traveling